

1 SEARCH FOR PRODUCTION OF A HIGGS BOSON AND A SINGLE TOP  
2 QUARK IN MULTILEPTON FINAL STATES IN  $pp$  COLLISIONS AT  $\sqrt{s} = 13$   
3 TeV.

4 by

5 Jose Andres Monroy MontaÑez

6 A DISSERTATION

7 Presented to the Faculty of

8 The Graduate College at the University of Nebraska

In Partial Fulfilment of Requirements

10 For the Degree of Doctor of Philosophy

11 Major: Physics and Astronomy

12 Under the Supervision of Kenneth Bloom and Aaron Dominguez

13 Lincoln, Nebraska

14 July, 2018

15 SEARCH FOR PRODUCTION OF A HIGGS BOSON AND A SINGLE TOP  
16 QUARK IN MULTILEPTON FINAL STATES IN pp COLLISIONS AT  $\sqrt{s} = 13$   
17 TeV.

18 Jose Andres Monroy Montañez, Ph.D.

19 University of Nebraska, 2018

20 Adviser: Kenneth Bloom and Aaron Dominguez

# **<sup>21</sup> Table of Contents**

<b><sup>22</sup> Table of Contents</b>	<b>iii</b>
<b><sup>23</sup> List of Figures</b>	<b>vii</b>
<b><sup>24</sup> List of Tables</b>	<b>x</b>
<b><sup>25</sup> 1 INTRODUCTION</b>	<b>1</b>
<b><sup>26</sup> 2 Theoretical approach</b>	<b>2</b>
27     2.1 Introduction . . . . .	2
28     2.2 Standard model of particle physics . . . . .	3
29     2.2.1 Fermions . . . . .	5
30     2.2.1.1 Leptons . . . . .	6
31     2.2.1.2 Quarks . . . . .	8
32     2.2.2 Fundamental interactions . . . . .	13
33     2.2.3 Gauge bosons . . . . .	18
34     2.3 Electroweak unification and the Higgs mechanism . . . . .	20
35     2.3.1 Spontaneous symmetry breaking (SSB) . . . . .	28
36     2.3.2 Higgs mechanism . . . . .	32
37     2.3.3 Masses of the gauge bosons . . . . .	35

38	2.3.4	Masses of the fermions . . . . .	36
39	2.3.5	The Higgs field . . . . .	37
40	2.3.6	Production of Higgs bosons at LHC . . . . .	38
41	2.3.7	Higgs boson decay channels . . . . .	42
42	2.4	Associated production of a Higgs boson and a single Top quark. . . . .	43
43	2.5	The CP-mixing in tH processes . . . . .	47
44	2.6	Experimantal status of the anomalous Higg-fermion coupling. . . . .	52
45	<b>3</b>	<b>The CMS experiment at the LHC</b>	<b>54</b>
46	3.1	Introduction . . . . .	54
47	3.2	The LHC . . . . .	55
48	3.3	The CMS experiment . . . . .	65
49	3.3.1	Coordinate system . . . . .	67
50	3.3.2	Pixels detector . . . . .	68
51	3.3.3	Silicon strip tracker . . . . .	70
52	3.3.4	Electromagnetic calorimeter . . . . .	72
53	3.3.5	Hadronic calorimeter . . . . .	73
54	3.3.6	Superconducting solenoid magnet . . . . .	75
55	3.3.7	Muon system . . . . .	76
56	3.3.8	CMS trigger system . . . . .	77
57	3.3.9	CMS computing . . . . .	79
58	<b>4</b>	<b>Event generation, simulation and reconstruction</b>	<b>83</b>
59	4.1	Event generation . . . . .	84
60	4.2	Monte Carlo Event Generators. . . . .	88
61	4.3	CMS detector simulation. . . . .	89
62	4.4	Event reconstruction. . . . .	91

63	4.4.1	Particle-Flow Algorithm.	92
64	4.4.2	Event reconstruction examples	104
65	<b>5</b>	<b>Statistical methods</b>	<b>107</b>
66	5.1	Multivariate analysis	107
67	5.2	MVA methods, NN, BDT, boosting, overtraining, variable ranking	109
68	5.3	statistical inference, likelihood parametrization	109
69	5.4	nuisance parameters	109
70	5.5	exclusion limits	109
71	5.6	asymptotic limits	109
72	<b>6</b>	<b>Search for production of a Higgs boson and a single top quark in multilepton final states in pp collisions at <math>\sqrt{s} = 13</math> TeV</b>	<b>110</b>
74	6.1	Introduction	110
75	6.2	Data and MC Samples	112
76	6.2.1	Full 2016 dataset and MC samples	112
77	6.2.2	Triggers	115
78	6.2.2.1	Trigger efficiency scale factors	115
79	6.3	Object Identification and event selection	116
80	6.3.1	Jets and $b$ tagging	116
81	6.3.2	Lepton selection	117
82	6.3.3	Lepton selection efficiency	118
83	6.4	Background predictions	119
84	6.5	Signal discrimination	120
85	6.5.1	Classifiers response	124
86	6.6	Additional discriminating variables	127

87 Bibliography 128

88 References 130

## <sup>89</sup> List of Figures

90	2.1	Standard model of particle physics.	4
91	2.2	Transformations between quarks	12
92	2.3	Fundamental interactions in nature.	13
93	2.4	SM interactions diagrams	14
94	2.5	Neutral current processes	21
95	2.6	Spontaneous symmetry breaking mechanism	29
96	2.7	SSB Potential form	30
97	2.8	Potential for complex scalar field	31
98	2.9	SSB mechanism for complex scalar field	32
99	2.10	Proton-Proton collision	39
100	2.11	Higgs boson production mechanism Feynman diagrams	40
101	2.12	Higgs boson production cross section and decay branching ratios	41
102	2.13	Associated Higgs boson production mechanism Feynman diagrams	43
103	2.14	Cross section for tHq process as a function of $\kappa_t$	46
104	2.15	Cross section for $tHW$ process as a function of $\kappa_{Htt}$	47
105	2.16	NLO cross section for $tX_0$ and $t\bar{t}X_0$ .	50
106	2.17	NLO cross section for $tWX_0$ , $t\bar{t}X_0$ .	51

107	2.18 Two dimentional $\kappa_t$ - $\kappa_V$ plot of the coupling modifiers. ATLAS and CMS 108 combination. . . . .	52
109	3.1 CERN accelerator complex . . . . .	55
110	3.2 LHC protons source. First acceleration stage. . . . .	56
111	3.3 The LINAC2 accelerating system at CERN. . . . .	57
112	3.4 LHC layout and RF cavities module. . . . .	58
113	3.5 LHC dipole magnet. . . . .	60
114	3.6 Integrated luminosity delivered by LHC and recorded by CMS during 2016	62
115	3.7 LHC interaction points . . . . .	63
116	3.8 Multiple $pp$ collision bunch crossing at CMS. . . . .	65
117	3.9 Layout of the CMS detector . . . . .	66
118	3.10 CMS detector coordinate system . . . . .	67
119	3.11 CMS pixel detector schematic view. . . . .	70
120	3.12 SST Schematic view. . . . .	71
121	3.13 CMS ECAL schematic view . . . . .	72
122	3.14 CMS HCAL schematic view . . . . .	74
123	3.15 CMS solenoid magnet . . . . .	75
124	3.16 CMS Muon system schematic view . . . . .	76
125	3.17 CMS Level-1 trigger architecture . . . . .	78
126	3.18 WLCG structure . . . . .	80
127	3.19 Data flow from CMS detector through hardware Tiers . . . . .	82
128	4.1 Event generation process. . . . .	84
129	4.2 Particle flow algorithm. . . . .	92
130	4.3 Jet reconstruction. . . . .	100
131	4.4 Jet energy corrections. . . . .	101

132	4.5	Secondary vertex in a b-hadron decay.	103
133	4.6	HIG-13-004 Event 1 reconstruction.	104
134	4.7	$e\mu$ event reconstruction.	105
135	4.8	Recorded event reconstruction.	106
136	5.1	Scatter plots-MVA event classification.	109
137	6.1	The two leading-order diagrams of $tHq$ production.	111
138	6.2	Input variables to the BDT for signal discrimination normalized.	121
139	6.3	Input variables to the BDT for signal discrimination not normalized.	123
140	6.4	BDT inputs as seen by TMVA against $t\bar{t}$ .	124
141	6.5	BDT inputs as seen by TMVA against $t\bar{t}V$ .	125
142	6.6	Correlation matrices for the input variables in the TMVA.	126
143	6.7	MVA classifiers performance.	126
144	6.8	Additional discriminating variables distributions.	128

# <sup>145</sup> List of Tables

146	2.1	Fermions of the SM. . . . .	5
147	2.2	Fermion masses. . . . .	6
148	2.3	Leptons properties. . . . .	9
149	2.4	Quarks properties. . . . .	9
150	2.5	Fermion weak isospin and weak hypercharge multiplets. . . . .	11
151	2.6	Fundamental interactions features. . . . .	15
152	2.7	SM gauge bosons. . . . .	20
153	2.8	Higgs boson properties. . . . .	38
154	2.9	Predicted branching ratios for a SM Higgs boson with $m_H = 125 \text{ GeV}/c^2$ . . . . .	42
155	2.10	Predicted SM cross sections for $tH$ production at $\sqrt{s} = 13 \text{ TeV}$ . . . . .	44
156	2.11	Predicted enhancement of the $tHq$ and $tHW$ cross sections at LHC . . . . .	48
157	6.1	Signal samples and their cross section and branching fraction. . . . .	112
158	6.2	$\kappa_V$ and $\kappa_t$ combinations. . . . .	113
159	6.3	List of background samples used in this analysis (CMSSW 80X). . . . .	114
160	6.4	Leading-order $t\bar{t}W$ and $t\bar{t}Z$ samples used in the signal BDT training. . . . .	114
161	6.5	Table of high-level triggers that we consider in the analysis. . . . .	115
162	6.6	Trigger efficiency scale factors and associated uncertainties. . . . .	116
163	6.7	Requirements on each of the three muon selections. . . . .	117

164	6.8 Criteria for each of the three electron selections. . . . .	118
165	6.9 MVA input discriminating variables . . . . .	122
166	6.10 TMVA input variables ranking for BDTA_GRAD method . . . . .	127
167	6.11 TMVA configuration used in the BDT training. . . . .	127
168	6.12 ROC-integral for all the testing cases. . . . .	129

<sup>169</sup> Chapter 1

<sup>170</sup> INTRODUCTION

# <sup>171</sup> Chapter 2

## <sup>172</sup> Theoretical approach

### <sup>173</sup> 2.1 Introduction

<sup>174</sup> The physical description of the universe is a challenge that physicists have faced by  
<sup>175</sup> making theories that refine existing principles and proposing new ones in an attempt  
<sup>176</sup> to embrace emerging facts and phenomena.

<sup>177</sup>

<sup>178</sup> At the end of 1940s Julian Schwinger [1] and Richard P. Feynman [2], based in the  
<sup>179</sup> work of Sin-Itiro Tomonaga [3], developed an electromagnetic theory consistent with  
<sup>180</sup> special relativity and quantum mechanics that describes how matter and light inter-  
<sup>181</sup> act; the so-called “quantum eletrodynamics” (QED) had born.

<sup>182</sup>

<sup>183</sup> QED has become the guide in the development of theories that describe the universe.  
<sup>184</sup> It was the first example of a quantum field theory (QFT), which is the theoretical  
<sup>185</sup> framework for building quantum mechanical models that describes particles and their  
<sup>186</sup> interactions. QFT is composed of a set of mathematical tools that combines classical  
<sup>187</sup> fields, special relativity and quantum mechanics, while keeping the quantum point

188 particles and locality ideas.

189 This chapter gives an overview of the standard model of particle physics, starting  
 190 with a description of the particles and interactions that compose it, followed by a  
 191 description of the electroweak interaction, the Higgs boson and the associated pro-  
 192 duction of Higgs boson and a single top quark ( $tH$ ). The description contained in  
 193 this chapter is based on references [4–6].

## 194 2.2 Standard model of particle physics

195 Particle physics at the fundamental level is modeled in terms of a collection of in-  
 196 teracting particles and fields in a theory known as the “standard model of particle  
 197 physics (SM)”<sup>1</sup>.

198

199 The full picture of the SM is composed of three fields<sup>2</sup>, whose excitations are inter-  
 200 preted as particles called mediators or force-carriers; a set of fields, whose excitations  
 201 are interpreted as elementary particles, interacting through the exchange of those  
 202 mediators and a field that gives the mass to elementary particles. Figure 2.1 shows  
 203 an scheme of the SM particles organization. In addition to the particles in the scheme  
 204 (but not listed in it), their corresponding anti-particles, with opposite quantum num-  
 205 bers, are also part of the picture; some particles are their own anti-particles, like  
 206 photon or Higgs, or anti-particle is already listed like in the  $W^+$  and  $W^-$  case.

207

208 The mathematical formulation of the SM is based on group theory and the use of  
 209 Noether’s theorem [8] which states that for a physical system modeled by a Lagrangian

---

<sup>1</sup> The formal and complete treatment of the SM is out of the scope of this document, however a plenty of textbooks describing it at several levels are available in the literature. The treatment in references [?] is quite comprehensive and detailed.

<sup>2</sup> Note that gravitational field is not included in the standard model formulation

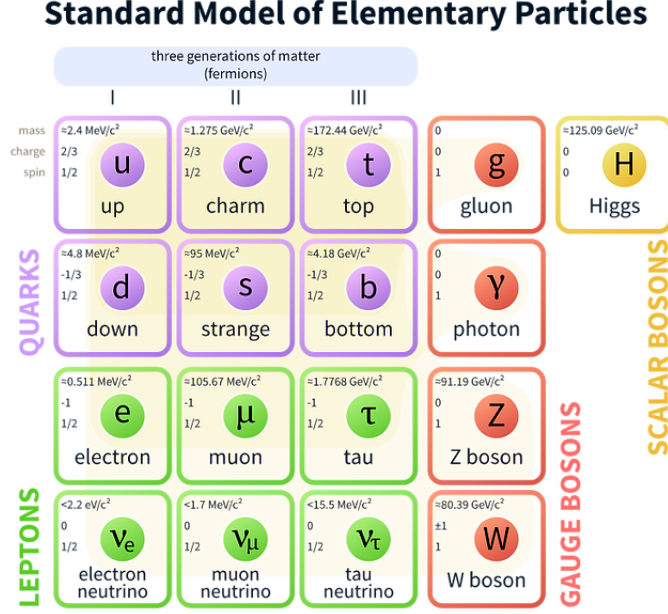


**Figure 2.1:** Schematic representation of the Standard model of particle physics. SM is a theoretical model intended to describe three of the four fundamental forces of the universe in terms of a set of particles and their interactions. [7].

that is invariant under a group of transformations a conservation law is expected. For instance, a system described by a time-independent Lagrangian is invariant (symmetric) under time changes (transformations) with the total energy conservation law as the expected conservation law. In QED, the charge operator ( $Q$ ) is the generator of the  $U(1)$  symmetry which according to the Noether's theorem means that there is a conserved quantity; this conserved quantity is the electric charge and thus the law of conservation of electric charge is established.

217

In the SM, the symmetry group  $SU(3)_C \otimes SU(2)_L \otimes U(1)_Y$  describes three of the four fundamental interactions in nature(see section 2.2.2): strong interaction(SI), weak interaction(WI) and electromagnetic interactions (EI) in terms of symmetries associated to physical quantities:

- 222     • Strong:  $SU(3)_C$  associated to color charge
- 223     • Weak:  $SU(2)_L$  associated to weak isospin and chirality
- 224     • Electromagnetic:  $U(1)_Y$  associated to weak hypercharge and electric charge
- 225   It will be shown that the electromagnetic and weak interactions are combined in  
 226   the so-called electroweak interaction where chirality, hypercharge, weak isospin and  
 227   electric charge are the central concepts.

228 **2.2.1 Fermions**

229 The basic constituents of the ordinary matter at the lowest level, which form the set  
 230 of elementary particles in the SM formulation, are quarks and leptons. All of them  
 231 have spin 1/2, therefore they are classified as fermions since they obey Fermi-Dirac  
 232 statistics. There are six “flavors” of quarks and three of leptons organized in three  
 233 generations, or families, as shown in table 2.1.

234

		Generation		
		1st	2nd	3rd
Leptons	Charged	Electron (e)	Moun( $\mu$ )	Tau ( $\tau$ )
	Neutral	Electron neutrino ( $\nu_e$ )	Muon neutrino ( $\nu_\mu$ )	Tau neutrino ( $\nu_\tau$ )
Quarks	Up-type	Up (u)	Charm (c)	Top (t)
	Down-type	Down (d)	Strange (s)	Bottom (b)

**Table 2.1:** Fermions of the SM. There are six flavors of quarks and three of leptons, organized in three generations, or families, composed of two pairs of closely related particles. The close relationship is motivated by the fact that WI between leptons is limited to the members of the same generation; WI between quarks is not limited but greatly favoured, to same generation members.

235

236 There is a mass hierarchy between generations (see table 2.2), where the higher gener-  
 237 ation particles decays to the lower one, which can explain why the ordinary matter is

made of particles in the first generation. In the SM, neutrinos are modeled as massless particles so they are not subject to this mass hierarchy; however, today it is known that neutrinos are massive so the hierarchy could be restated. The reason behind this mass hierarchy is one of the most important open questions in particle physics, and it becomes more puzzling when noticing that the mass difference between first and second generation fermions is small compared to the mass difference with respect to the third generation.

Lepton	Mass (MeV/c <sup>2</sup> )	Quark	Mass (MeV/c <sup>2</sup> )
e	0.51	u	2.2
$\mu$	105.65	c	$1.28 \times 10^3$
$\tau$	1776.86	t	$173.1 \times 10^3$
$\nu_e$	Unknown	d	4.7
$\nu_\mu$	Unknown	s	96
$\tau_\mu$	Unknown	b	$4.18 \times 10^3$

**Table 2.2:** Fermion masses [9]. Generations differ by mass in a way that have been interpreted as a masss hierarchy. Approximate values with no uncertainties are used, for comparison purpose.

Usually, the second and third generation fermions are produced in high energy processes, like the ones recreated in particle accelerators.

### 2.2.1.1 Leptons

A lepton is an elementary particle that is not subject to the SI. As seen in table 2.1, there are two types of leptons, the charged ones (electron, muon and tau) and the neutral ones (the three neutrinos). The electric charge (Q) is the property that gives leptons the ability to participate in the EI. From the classical point of view, Q plays a central role determining, among others, the strength of the electric field through which the electromagnetic force is exerted. It is clear that neutrinos are not affected

255 by EI because they don't carry electric charge.

256

257 Another feature of the leptons that is fundamental in the mathematical description  
258 of the SM is the chirality, which is closely related to spin and helicity. Helicity defines  
259 the handedness of a particle by relating its spin and momentum such that if they  
260 are parallel then the particle is right-handed; if spin and momentum are antiparallel  
261 the particle is said to be left-handed. The study of parity conservation (or viola-  
262 tion) in  $\beta$ -decay has shown that only left-handed electrons/neutrinos or right-handed  
263 positrons/anti-neutrinos are created [10]; the inclusion of that feature in the theory  
264 was achieved by using projection operators for helicity, however, helicity is frame de-  
265 pendent for massive particles which makes it not Lorentz invariant and then another  
266 related attribute has to be used: *chirality*.

267

268 Chirality is a purely quantum attribute which makes it not so easy to describe in  
269 graphical terms but it defines how the wave function of a particle transforms under  
270 certain rotations. As with helicity, there are two chiral states, left-handed chiral (L)  
271 and right-handed chiral (R). In the highly relativistic limit where  $E \approx p \gg m$  helicity  
272 and chirality converge, becoming exactly the same for massless particles.

273

274 In the following, when referring to left-handed (right-handed) it will mean left-handed  
275 chiral (right-handed chiral). The fundamental fact about chirality is that while EI  
276 and SI are not sensitive to chirality, in WI left-handed and right-handed fermions are  
277 treated asymmetrically, such that only left handed fermions and right-handed anti-  
278 fermions are allowed to couple to WI mediators, which is a violation of parity. The  
279 way to translate this statement in a formal mathematical formulation is based on the  
280 isospin symmetry group  $SU(2)_L$ .

281

282 Each generation of leptons is seen as a weak isospin doublet.<sup>3</sup> The left-handed charged  
 283 lepton and its associated left-handed neutrino are arranged in doublets of weak isospin  
 284 T=1/2 while their right-handed partners are singlets:

$$\begin{pmatrix} \nu_l \\ l \end{pmatrix}_L, l_R := \begin{pmatrix} \nu_e \\ e \end{pmatrix}_L, \begin{pmatrix} \nu_\mu \\ \mu \end{pmatrix}_L, \begin{pmatrix} \nu_\tau \\ \tau \end{pmatrix}_L, e_R, \mu_R, \tau_R, \nu_{eR}, \nu_{\mu R}, \nu_{\tau R} \quad (2.1)$$

285 The isospin third component refers to the eigenvalues of the weak isospin operator  
 286 which for doublets is  $T_3 = \pm 1/2$ , while for singlets it is  $T_3 = 0$ . The physical meaning  
 287 of this doublet-singlet arrangement falls in that the WI couples the two particles in  
 288 the doublet by exchanging the interaction mediator while the singlet member is not  
 289 involved in WI. The main properties of the leptons are summarized in table 2.3.

290

291 Altough all three flavor neutrinos have been observed, their masses remain unknown  
 292 and only some estimations have been made [11]. The main reason is that the fla-  
 293 vor eigenstates are not the same as the mass eigenstates which implies that when  
 294 a neutrino is created its mass state is a linear combination of the three mass eigen-  
 295 states and experiments can only probe the squared difference of the masses. The  
 296 Pontecorvo-Maki-Nakagawa-Sakata (PMNS) mixing matrix encode the relationship  
 297 between flavor and mass eigenstates.

298

### 299 2.2.1.2 Quarks

300 Quarks are the basic constituents of protons and neutrons. The way quarks join to  
 301 form bound states, called “hadrons”, is through the SI. Quarks are affected by all the

---

<sup>3</sup> The weak isospin is an analogy of the isospin symmetry in strong interaction where neutron and proton are affected equally by strong force but differ in their charge.

Lepton	Q(e)	$T_3$	$L_e$	$L_\mu$	$L_\tau$	Lifetime (s)
Electron (e)	-1	-1/2	1	0	0	Stable
Electron neutrino( $\nu_e$ )	0	1/2	1	0	0	Unknown
Muon ( $\mu$ )	-1	-1/2	0	1	0	$2.19 \times 10^{-6}$
Muon neutrino ( $\nu_\mu$ )	0	1/2	0	1	0	Unknown
Tau ( $\tau$ )	-1	-1/2	0	0	1	$290.3 \times 10^{-15}$
Tau neutrino ( $\tau_\mu$ )	0	1/2	0	0	1	Unknown

**Table 2.3:** Leptons properties [9]. Q: electric charge,  $T_3$ : weak isospin. Only left-handed leptons and right-handed anti-leptons participate in the WI. Anti-particles with inverted  $T_3$ , Q and lepton number complete the leptons set but are not listed. Right-handed leptons and left-handed anti-leptons, neither listed, form weak isospin singlets with  $T_3 = 0$  and do not take part in the weak interaction.

302 fundamental interactions which means that they carry all the four types of charges:  
 303 color, electric charge, weak isospin and mass.

Flavor	Q(e)	$I_3$	$T_3$	B	C	S	T	$B'$	Y	Color
Up (u)	2/3	1/2	1/2	1/3	0	0	0	0	1/3	r,b,g
Charm (c)	2/3	0	1/2	1/3	1	0	0	0	4/3	r,b,g
Top(t)	2/3	0	1/2	1/3	0	0	1	0	4/3	r,b,g
Down(d)	-1/3	-1/2	-1/2	1/3	0	0	0	0	1/3	r,b,g
Strange(s)	-1/3	0	-1/2	1/3	0	-1	0	0	-2/3	r,b,g
Bottom(b)	-1/3	0	-1/2	1/3	0	0	0	-1	-2/3	r,b,g

**Table 2.4:** Quarks properties [9]. Q: electric charge,  $I_3$ : isospin,  $T_3$ : weak isospin, B: baryon number, C: charmness, S: strangeness, T: topness,  $B'$ : bottomness, Y: hypercharge. Anti-quarks posses the same mass and spin as quarks but all charges (color, flavor numbers) have opposite sign.

304  
 305 Table 2.4 summarizes the features of quarks, among which the most particular is  
 306 their fractional electric charge. Note that fractional charge is not a problem, given  
 307 that quarks are not found isolated, but serves to explain how composed particles are  
 308 formed out of two or more valence quarks<sup>4</sup>.

309

---

<sup>4</sup> Hadrons can contain an indefinite number of virtual quarks and gluons, known as the quark and gluon sea, but only the valence quarks determine hadrons' quantum numbers.

310 Color charge is the responsible for the SI between quarks and is the symmetry  
 311 ( $SU(3)_C$ ) that defines the formalism to describe SI. There are three colors: red (r),  
 312 blue(b) and green(g) and their corresponding three anti-colors; thus each quark carries  
 313 one color unit while anti-quarks carries one anti-color unit. As said above, quarks are  
 314 not allowed to be isolated due to the color confinement effect, therefore their features  
 315 have been studied indirectly by observing their bound states created when:

- 316     • one quark with a color charge is attracted by an anti-quark with the correspond-  
 317         ing anti-color charge forming a colorless particle called a “meson.”
- 318     • three quarks (anti-quarks) with different color (anti-color) charges are attracted  
 319         among them forming a colorless particle called a “baryon(anti-baryon).”

320 In practice, when a quark is left alone isolated a process called “hadronization” occurs  
 321 where the quark emits gluons (see section 2.2.3) which eventually will generate new  
 322 quark-antiquark pairs and so on; those quarks will recombine to form hadrons that  
 323 will decay into leptons. This proliferation of particles looks like a “jet” coming from  
 324 the isolated quark. More details about the hadronization process and jet structure  
 325 will be given in chapter4.

326 In the first version of the quark model (1964), M. Gell-Mann [12] and G. Zweig  
 327 [13, 14] developed a consistent way to classify hadrons according to their properties.  
 328 Only three quarks (u, d, s) were involved in a scheme in which all baryons have  
 329 baryon number  $B=1$  and therefore quarks have  $B=1/3$ ; non-baryons have  $B=0$ . The  
 330 scheme organizes baryons in a two-dimensional space ( $I_3 - Y$ );  $Y$  (hypercharge) and  $I_3$   
 331 (isospin) are quantum numbers related by the Gell-Mann-Nishijima formula [15, 16]:

$$Q = I_3 + \frac{Y}{2} \quad (2.2)$$

332 where  $Y = B + S + C + T + B'$  are the quantum numbers listed in table 2.4. Baryon  
 333 number is conserved in SI and EI which means that single quarks cannot be created  
 334 but in pairs  $q - \bar{q}$ .

335

336 There are six quark flavors organized in three generations (see table 2.1) following a  
 337 mass hierarchy which, again, implies that higher generations decay to first generation  
 338 quarks.

	Quarks			$T_3$	$Y_W$	Leptons			$T_3$	$Y_W$
Doublets	$(\begin{smallmatrix} u \\ d' \end{smallmatrix})_L$	$(\begin{smallmatrix} c \\ s' \end{smallmatrix})_L$	$(\begin{smallmatrix} t \\ b' \end{smallmatrix})_L$	$(\begin{smallmatrix} 1/2 \\ -1/2 \end{smallmatrix})$	1/3	$(\begin{smallmatrix} \nu_e \\ e \end{smallmatrix})_L$	$(\begin{smallmatrix} \nu_\mu \\ \mu \end{smallmatrix})_L$	$(\begin{smallmatrix} \nu_\tau \\ \tau \end{smallmatrix})_L$	$(\begin{smallmatrix} 1/2 \\ -1/2 \end{smallmatrix})$	-1
Singlets	$u_R$	$c_R$	$t_R$	0	4/3	$\nu_{eR}$	$\nu_{\mu R}$	$\nu_{\tau R}$	0	-2
	$d'_R$	$s'_R$	$b'_R$	0	-2/3	$e_R$	$\mu_R$	$\tau_R$		

**Table 2.5:** Fermion weak isospin and weak hypercharge multiplets. Weak hypercharge is calculated through the Gell-Mann-Nishijima formula 2.2 but using the weak isospin and charge for quarks.

339

340 Isospin doublets of quarks are also defined (see table 2.5) and as for neutrinos, the  
 341 mass eigenstates are not the same as the WI eigenstates which means that members of  
 342 different quark generations are connected by the WI mediator; thus, up-type quarks  
 343 are coupled not to down-type quarks directly but to a superposition of down-type  
 344 quarks ( $q'_d$ ) via WI according to:

$$q'_d = V_{CKM} q_d$$

345

$$\begin{pmatrix} d' \\ s' \\ b' \end{pmatrix} = \begin{pmatrix} V_{ud} & V_{us} & V_{ub} \\ V_{cd} & V_{cs} & V_{cb} \\ V_{td} & V_{ts} & V_{tb} \end{pmatrix} \begin{pmatrix} d \\ s \\ b \end{pmatrix} \quad (2.3)$$

346 where  $V_{CKM}$  is known as Cabibbo-Kobayashi-Maskawa (CKM) mixing matrix [17,18].

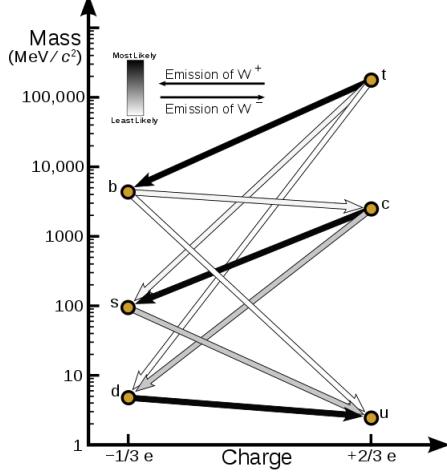


**Figure 2.2:** Transformations between quarks through the exchange of a WI. Higher generations quarks decay to first generation quarks by emitting a W boson. The arrow color indicates the likelihood of the transition according to the grey scale in the top left side which represent the CKM matrix parameters [19].

347 The weak decays of quarks are represented in the diagram of figure 2.2; again the  
 348 CKM matrix plays a central role since it contains the probabilities for the different  
 349 quark decay channels, in particular, note that quark decays are greatly favored be-  
 350 tween generation members.

351

352 CKM matrix is a  $3 \times 3$  unitary matrix parametrized by three mixing angles and  
 353 the *CP-mixing phase*; the latter is the parameter responsible for the Charge-Parity  
 354 symmetry violation (CP-violation) in the SM. The fact that the b quark decays almost  
 355 all the times to a top quark is exploited in this thesis when making the selection of  
 356 the signal events by requiring the presence of a jet tagged as a jet coming from a  
 357 b quark in the final state. The effect of the *CP-mixing phase* on the cross section of  
 358 associated production of Higgs boson and a single top process is also explored in this  
 359 thesis.

360 2.2.2 Fundamental interactions

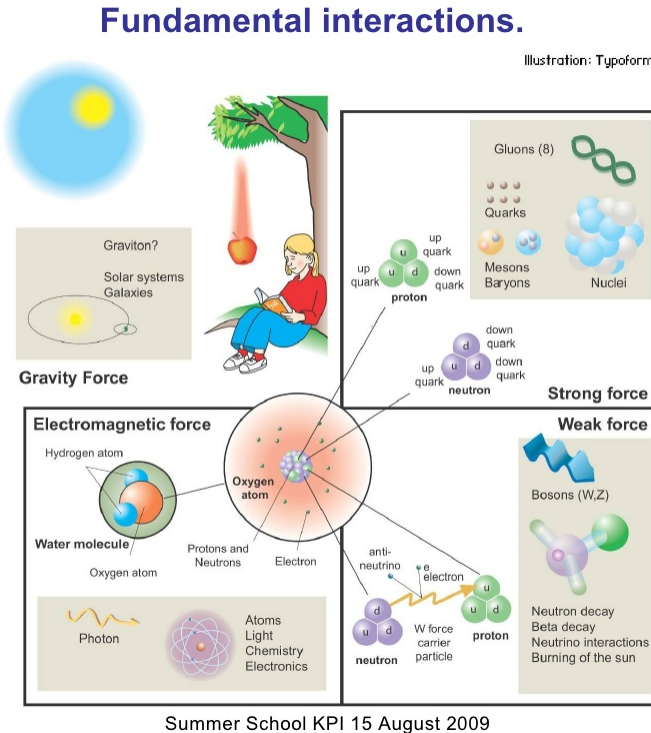


**Figure 2.3:** Fundamental interactions in nature. Despite the many manifestations of forces in nature, we can track all of them back to one of the fundamental interactions. The most common forces are gravity and electromagnetic given that all of us are subject and experience them in everyday life.

361 Even though there are many manifestations of force in nature, like the ones repre-

362 sented in figure 2.3, we can classify all of them into one of four fundamental interac-

363 tions:

- 364 • *Electromagnetic interaction (EI)* affects particles that are “electrically charged,”
- 365 like electrons and protons. It is described by QED combining quantum mechan-
- 366 ics, special relativity and electromagnetism in order to explain how particles
- 367 with electric charge interact through the exchange of photons, therefore, one
- 368 says that “Electromagnetic Force” is mediated by “photons”. Figure 2.4a. shows

369 a graphical representation, known as “feynman diagram”, of electron-electron  
 370 scattering.

- 371 • *Strong interaction (SI)* described by Quantum Chromodynamics (QCD). Hadrons  
 372 like proton and neutron have internal structure given that they are composed  
 373 of two or more valence quarks<sup>5</sup>. Quarks have fractional electric charge which  
 374 means that they are subject to electromagnetic interaction and in the case of the  
 375 proton they should break apart due to electrostatic repulsion; however, quarks  
 376 are held together inside the hadrons against their electrostatic repulsion by the  
 377 “Strong Force” through the exchange of “gluons.” The analog to the electric  
 378 charge is the “color charge”. Electrons and photons are elementary particles  
 379 as quarks but they don’t carry color charge, therefore they are not subject to  
 380 SI. The feynman diagram for gluon exchange between quarks is shown in figure  
 381 2.4b.

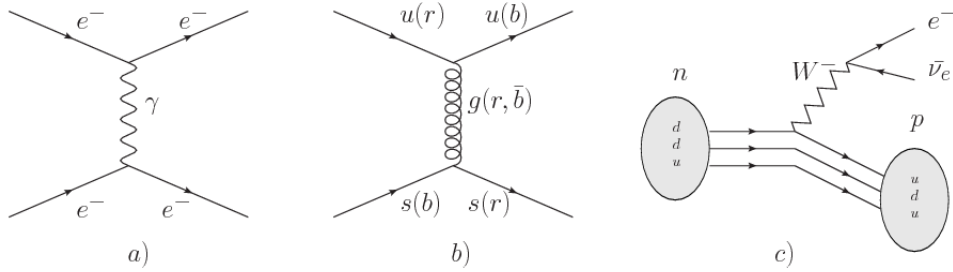


**Figure 2.4:** Feynman diagrams representing the interactions in SM; a) EI: e-e scattering; b) SI: gluon exchange between quarks ; c) WI:  $\beta$ -decay

- 382 • *Weak interaction (WI)* described by the weak theory (WT), is responsible, for  
 383 instance, for the radioactive decay in atoms and proton-proton (pp) fusion  
 384 within the sun. Quarks and leptons are the particles affected by the weak  
 385 interaction; they possess a property called “flavor charge” (see 2.2.1) which can  
 386 be changed by emitting or absorbing one weak force mediator. There are three

<sup>5</sup> particles made of four and five quarks are exotic states not so common.

387 mediators of the “weak force” known as “Z” boson in the case of electrically  
 388 neutral changes and “ $W^\pm$ ” bosons in the case of electrically charged changes.  
 389 The “weak isospin” is the WI analog to electric charge in EI, and color charge  
 390 in SI, and defines how quarks and leptons are affected by the weak force. Figure  
 391 2.4c. shows the feynman diagram of  $\beta$ -decay where a newtron (n) is transformed  
 392 in a proton (p) by emmiting a  $W^-$  particle. Since this thesis is in the frame  
 393 of the electroweak interaction, a more detailed description of it will be given in  
 394 section 2.3

395 • *Gravitational interaction (GI)* described by General Theory of Relativity (GR).  
 396 It is responsible for the structure of galaxies and black holes as well as the  
 397 expansion of the universe. As a classical theory, in the sense that it can be for-  
 398 mulated without even appeal to the concept of quantization, it implies that the  
 399 spacetime is a continuum and predictions can be made without limitation to the  
 400 precision of the measurement tools. The latter represent a direct contradiction  
 401 of the quantum mechanics principles. Gravity is deterministic while quantum  
 402 mechanics is probabilistic; despite that, efforts to develop a quantum theory of  
 403 gravity have predicted the “graviton” as mediator of the Gravitational force<sup>6</sup>.

Interaction	Acts on	Relative strength	Range (m)	Mediators
Electromagnetic (QED)	Electrically charged particles	$10^{-2}$	Infinite	Photon
Strong (QCD)	Quarks and gluons	1	$10^{-15}$	Gluon
Weak (WI)	Leptons and quarks	$10^{-6}$	$10^{-18}$	$W^\pm$ , Z
Gravitational (GI)	Massive particles	$10^{-39}$	Infinite	Graviton

**Table 2.6:** Fundamental interactions features [20].

404

---

<sup>6</sup> Actually a wide variety of theories have been developed in an attempt to describe gravity; some famous examples are string theory and supergravity.

405 Table 2.6 summarizes the main features of the fundamental interactions. The rela-  
 406 tive strength of the fundamental forces reveals the meaning of strong and weak; in  
 407 a context where the relative strength of the SI is 1, the EI is about hundred times  
 408 weaker and WI is about million times weaker than the SI. A good description on  
 409 how the relative strength and range of the fundamental interactions are calculated  
 410 can be found in references [20,21]. In the everyday life, only EI and GI are explicitly  
 411 experienced due to the range of these interactions; i.e., at the human scale distances  
 412 only EI and GI have appreciable effects, in contrast to SI which at distances greater  
 413 than  $10^{-15}$ m become negligible.

414

415 QED was built successfully on the basis of the classical electrodynamics theory (CED)  
 416 of Maxwell and Lorentz, following theoretical and experimental requirements imposed  
 417 by

- 418     • lorentz invariance: independence on the reference frame.
- 419     • locality: interacting fields are evaluated at the same space-time point to avoid  
     420       action at a distance.
- 421     • renormalizability: physical predictions are finite and well defined
- 422     • particle spectrum, symmetries and conservation laws already known must emerge  
     423       from the theory.
- 424     • gauge invariance.

425 The gauge invariance requirement reflects the fact that the fundamental fields cannot  
 426 be directly measured but associated fields which are the observables. Electric (“E”)  
 427 and magnetic (“B”) fields in CED are associated with the electric scalar potential

428 “V” and the vector potential “A”. In particular,  $\mathbf{E}$  can be obtained by measuring  
 429 the change in the space of the scalar potential ( $\Delta V$ ); however, two scalar potentials  
 430 differing by a constant “f” correspond to the same electric field. The same happens in  
 431 the case of the vector potential “A”; thus, different configurations of the associated  
 432 fields result in the same set of values of the observables. The freedom in choosing  
 433 one particular configuration is known as “gauge freedom”; the transformation law con-  
 434 necting two configurations is known as “gauge transformation” and the fact that the  
 435 observables are not affected by a gauge transformation is called “gauge invariance”.

436

437 When the gauge transformation:

$$\begin{aligned} \mathbf{A} &\rightarrow \mathbf{A} - \Delta f \\ V &\rightarrow V - \frac{\partial f}{\partial t} \end{aligned} \tag{2.4}$$

488 is applied to Maxwell equations, they are still satisfied and the fields remain invariant.  
 489 Thus, CED is invariant under gauge transformations and is called a “gauge theory”.  
 490 The set of all gauge transformations form the “symmetry group” of the theory, which  
 491 according to the group theory, has a set of “group generators”. The number of group  
 492 generators determine the number of “gauge fields” of the theory.

493

494 As mentioned in the first lines of section 2.2, QED has one symmetry group ( $U(1)$ )  
 495 with one group generator (the  $Q$  operator) and one gauge field (the electromagnetic  
 496 field  $A^\mu$ ). In CED there is not a clear definition, beyond the historical convention, of  
 497 which fields are the fundamental and which are the associated, but in QED it is clear  
 498 that the fundamental field is  $A^\mu$ . When a gauge theory is quantized, the gauge field

449 is quantized and its quanta is called “gauge boson”. The word boson characterizes  
 450 particles with integer spin which obvey Bose-einstein statistics.

451

452 As will be detailed in section 2.3, interactions between partcles in a system can be  
 453 obtained by considering first the Lagrangian density of free particles in the system,  
 454 which of course is incomplete because the interaction terms have been left out, and  
 455 demanding global phase transformation invariance. Global phase transformation in-  
 456 variance means that a gauge transformation is performed identically to every point  
 457 in the space<sup>7</sup> and the Lagrangian remains invariant. Then, the global transformation  
 458 is promoted to a local phase transformation (this time the gauge transformation de-  
 459 pends on the position in space) and again invariance is required.

460

461 Due to the space dependence of the local tranformation, the Lagrangian density is  
 462 not invariant anymore. In order to restate the gauge invariance, the gauge covariant  
 463 derivative is introduced in the Lagrangian and with it the gauge field responsible for  
 464 the interaction between particles in the system. The new Lagrangian density is gauge  
 465 invariant, includes the interaction terms needed to account for the interactions and  
 466 provides a way to explain the interaction between particles through the exchange of  
 467 the gauge boson.

468 This recipe was used to build QED and the theories that aim to explain the funda-  
 469 mental interactions.

### 470 **2.2.3 Gauge bosons**

471 The importance of the gauge bosons comes from the fact that they are the force  
 472 mediators or force carriers. The features of the gauge bosons reflect those of the

---

<sup>7</sup> Here space corresponds to the 4-dimensional space i.e. space-time.

473 fields they represent and they are extracted from the Lagrangian density used to  
 474 describe the interactions. In section 2.3, it will be shown how the gauge bosons of the  
 475 EI and WI emerge from the electroweak Lagrangian. The SI gauge bosons features  
 476 are also extracted from the SI Lagrangian but it is not detailed in this document. The  
 477 main features of the SM gauge bosons will be briefly presented below and summarized  
 478 in table 2.7.

- 479     • **Photon.** EI occurs when the photon couples to (is exchanged between) particles  
 480       carrying electric charge; however, the photon itself does not carry electric charge,  
 481       therefore, there is no coupling between photons. Given that the photon is  
 482       massless the EI is of infinite range, i.e., electrically charged particles interact  
 483       even if they are located far away one from each other; this also implies that  
 484       photons always move with the speed of light.
- 485     • **Gluon.** SI is mediated by gluons which, same as photons, are massless. They  
 486       carry one unit of color charge and one unit of anticolor charge which means that  
 487       gluons couple to other gluons. As a result, the range of the SI is not infinite  
 488       but very short due to the attraction between gluons, giving rise to the “color  
 489       confinement” which explains why color charged particles cannot be isolated but  
 490       live within composited particles, like quarks inside protons.
- 491     • **W, Z.** The WI mediators,  $W^\pm$  and Z, are massive which explains their short-  
 492       range. Given that the WI is the only interaction that can change the flavor  
 493       of the interacting particles, the W boson is the responsible for the nuclear  
 494       transmutation where a neutron is converted in a proton or vice versa with the  
 495       involvement of an electron and a neutrino (see figure 2.4c). The Z boson is the  
 496       responsible of the neutral weak processes like neutrino elastic scattering where

497 no electric charge but momentum transference is involved. WI gauge bosons  
 498 carry isospin charge which makes possible the interaction between them.

Interaction	Mediator	Electric charge (e)	Color charge	Weak Isospin	mass (GeV/c <sup>2</sup> )
Electromagnetic	Photon ( $\gamma$ )	0	No	0	0
Strong	Gluon (g)	0	Yes -octet	No	0
Weak	$W^\pm$ Z	$\pm 1$ 0	No No	$\pm 1$ 0	$80.385 \pm 0.015$ $91.188 \pm 0.002$

**Table 2.7:** SM gauge bosons main features [9].

499

500 **2.3 Electroweak unification and the Higgs  
 501 mechanism**

502 Physicists dream of building a theory that contains all the interactions in one single  
 503 interaction, i.e., showing that at some scale in energy all the four fundamental in-  
 504 teractions are unified and only one interaction emerges in a “Theory of everything”.  
 505 The first sign of the feasibility of such unification comes from success in the con-  
 506 struction of the CED. Einstein spent years trying to reach that dream, which by  
 507 1920 only involved electromagnetism and gravity, with no success; however, a new  
 508 partial unification was achieved in the 1960’s, when S.Glashow [22], A.Salam [23] and  
 509 S.Weinberg [24] independently proposed that electromagnetic and weak interactions  
 510 are two manifestations of a more general interaction called “electroweak interaction  
 511 (EWT)”. Both, QCD and EWT, were developed in parallel and following the useful  
 512 prescription provided by QED and the gauge invariance principles.

513

514 The theory of weak interactions was capable of explaining the  $\beta$ -decay and in general  
 515 the processes mediated by  $W^\pm$  bosons. However, there were some processes like the

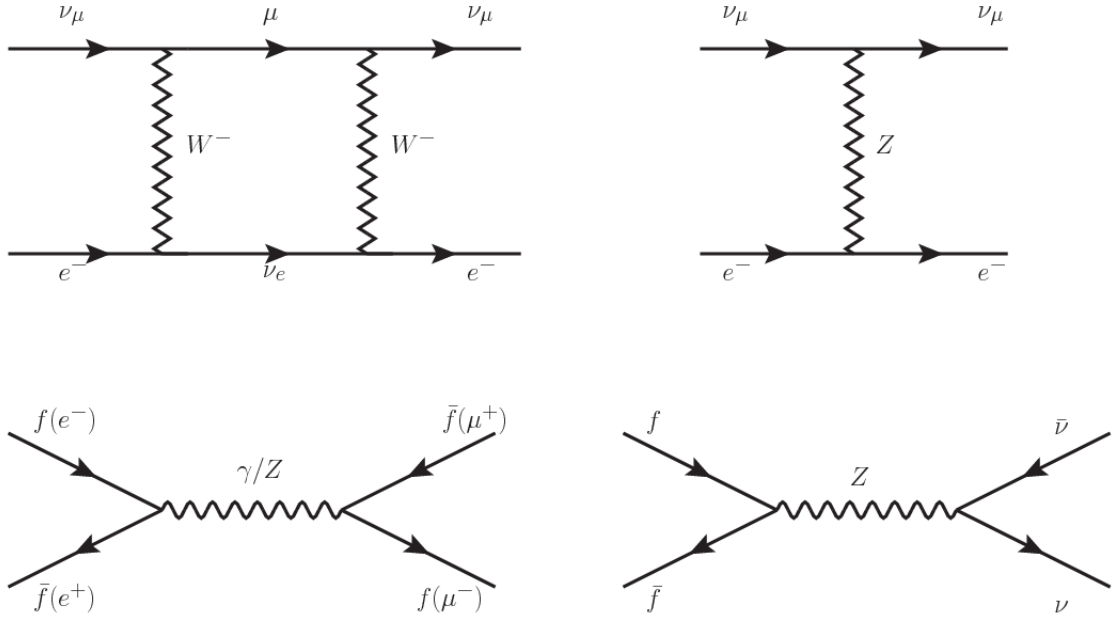


**Figure 2.5:** Top:  $\nu_\mu - e^-$  scattering going through charged currents (left) and neutral currents (right). Bottom: neutral current processes for charged fermions (left) and involving neutrinos (right). While neutral current processes involving only charged fermions can proceed through EI or WI, those involving neutrinos can only proceed via WI.

516 “ $\nu_\mu - e$  scattering” which would require the exchange of two  $W$  bosons (see figure 2.5  
517 top diagrams) giving rise to divergent loop integrals and then non finite predictions.  
518 By including neutral currents involving fermions via the exchange of neutral bosons  
519  $Z$ , those divergences are compensated and the predictions become realistic.

520

521 Neutral weak interaction vertices conserve flavor in the same way as the electromag-  
522 netic vertices do, but additionally, the  $Z$  boson can couple to neutrinos which implies  
523 that processes involving charged fermions can proceed through EI or WI but processes  
524 involving neutrinos can proceed only through WI.

525

526 The prescription to build a gauge theory of the WI consists of proposing a free field  
527 Lagrangian density that includes the particles involved; next, by requesting invari-

528 ance under global phase transformations first and generalizing to local phase trans-  
 529 formations invariance later, the conserved currents are identified and interactions are  
 530 generated by introducing gauge fields. Given that the goal is to include the EI and  
 531 WI in a single theory, the group symmetry considered should be a combination of  
 532  $SU(2)_L$  and  $U(1)_{em}$ , however the latter cannot be used directly because the EI treats  
 533 left and right-handed particles indistinctly in contrast to the former. Fortunately, the  
 534 weak hypercharge, which is a combination of the weak isospin and the electric charge  
 535 (eqn 2.2) is suitable to be used since it is conserved by the EI and WI. Thus, the  
 536 symmetry group to be considered is

$$G \equiv SU(2)_L \otimes U(1)_Y \quad (2.5)$$

537 The following treatment applies to any of the fermion generations, but for simplicity  
 538 the first generation of leptons will be considered [5, 6, 25, 26].

539

540 Given the first generation of leptons

$$\psi_1 = \begin{pmatrix} \nu_e \\ e^- \end{pmatrix}_L, \quad \psi_2 = \nu_{eR}, \quad \psi_3 = e_R^- \quad (2.6)$$

541 the charged fermionic currents are given by

$$J_\mu \equiv J_\mu^+ = \bar{\nu}_{eL} \gamma_\mu e_L, \quad J_\mu^\dagger \equiv J_\mu^- = \bar{e}_L \gamma_\mu \nu_{eL} \quad (2.7)$$

542 and the free Lagrangian is given by

$$\mathcal{L}_0 = \sum_{j=1}^3 i\bar{\psi}_j(x) \gamma^\mu \partial_\mu \psi_j(x). \quad (2.8)$$

543 Mass terms are included directly in the QED and QCD free Lagrangians since they

544 preserve the invariance under the symmetry transformations involved which treat  
 545 left-handed and right-handed similarly, however mass terms of the form

$$m_W^2 W_\mu^\dagger(x) W^\mu(x) + \frac{1}{2} m_Z^2 Z_\mu(x) Z^\mu(x) - m_e \bar{\psi}_e(x) \psi_e(x) \quad (2.9)$$

546 which represent the mass of  $W^\pm$ , Z and electrons, are not invariant under G trans-  
 547 formations, therefore the gauge fields described by the EWI are in principle massless.

548

549 Experiments have shown that the gauge fields are not massless; however, they have  
 550 to acquire mass through a mechanism compatible with the gauge invariance; that  
 551 mechanism is known as the “Higgs mechanism” and will be considered later in this  
 552 section. The global transformations in the combined symmetry group G can be  
 553 written as

$$\begin{aligned} \psi_1(x) &\xrightarrow{G} \psi'_1(x) \equiv U_Y U_L \psi_1(x), \\ \psi_2(x) &\xrightarrow{G} \psi'_2(x) \equiv U_Y \psi_2(x), \\ \psi_3(x) &\xrightarrow{G} \psi'_3(x) \equiv U_Y \psi_3(x) \end{aligned} \quad (2.10)$$

554 where  $U_L$  represent the  $SU(2)_L$  transformation acting only on the weak isospin dou-  
 555 blet and  $U_Y$  represent the  $U(1)_Y$  transformation acting on all the weak isospin mul-  
 556 tiplets. Explicitly

$$U_L \equiv \exp\left(i \frac{\sigma_i}{2} \alpha^i\right), \quad U_Y \equiv \exp(i y_i \beta) \quad (i = 1, 2, 3) \quad (2.11)$$

557 with  $\sigma_i$  the Pauli matrices and  $y_i$  the weak hypercharges. In order to promote the  
 558 transformations from global to local while keeping the invariance, it is required that

559  $\alpha^i = \alpha^i(x)$ ,  $\beta = \beta(x)$  and the replacement of the ordinary derivatives by the covariant  
 560 derivatives

$$\begin{aligned} D_\mu \psi_1(x) &\equiv \left[ \partial_\mu + ig\sigma_i W_\mu^i(x)/2 + ig'y_1 B_\mu(x) \right] \psi_1(x) \\ D_\mu \psi_2(x) &\equiv \left[ \partial_\mu + ig'y_2 B_\mu(x) \right] \psi_2(x) \\ D_\mu \psi_3(x) &\equiv \left[ \partial_\mu + ig'y_3 B_\mu(x) \right] \psi_3(x) \end{aligned} \quad (2.12)$$

561 introducing in this way four gauge fields,  $W_\mu^i(x)$  and  $B_\mu(x)$ , in the process. The  
 562 covariant derivatives (eqn 2.12) are required to transform in the same way as fermion  
 563 fields  $\psi_i(x)$  themselves, therefore, the gauge fields transform as:

$$\begin{aligned} B_\mu(x) &\xrightarrow{G} B'_\mu(x) \equiv B_\mu(x) - \frac{1}{g'} \partial_\mu \beta(x) \\ W_\mu^i(x) &\xrightarrow{G} W_\mu^{i\prime}(x) \equiv W_\mu^i(x) - \frac{i}{g} \partial_\mu \alpha_i(x) - \varepsilon_{ijk} \alpha_i(x) W_\mu^j(x). \end{aligned} \quad (2.13)$$

564 The G invariant version of the Lagrangian density 2.8 can be written as

$$\mathcal{L}_0 = \sum_{j=1}^3 i\bar{\psi}_j(x) \gamma^\mu D_\mu \psi_j(x) \quad (2.14)$$

565 where free massless fermion and gauge fields and fermion-gauge boson interactions  
 566 are included. The EWI Lagrangian density must additionally include kinetic terms  
 567 for the gauge fields ( $\mathcal{L}_G$ ) which are built from the field strengths, according to

$$B_{\mu\nu}(x) \equiv \partial_\mu B_\nu - \partial_\nu B_\mu \quad (2.15)$$

$$W_{\mu\nu}^i(x) \equiv \partial_\mu W_\nu^i(x) - \partial_\nu W_\mu^i(x) - g\varepsilon^{ijk}W_\mu^j W_\nu^k \quad (2.16)$$

568 the last term in eqn. 2.16 is added in order to hold the gauge invariance; therefore,

$$\mathcal{L}_G = -\frac{1}{4}B_{\mu\nu}(x)B^{\mu\nu}(x) - \frac{1}{4}W_{\mu\nu}^i(x)W_i^{\mu\nu}(x) \quad (2.17)$$

569 which contains not only the free gauge fields contributions, but also the gauge fields  
570 self-interactions and interactions among them.

571

572 The three weak isospin conserved currents resulting from the  $SU(2)_L$  symmetry are  
573 given by

$$J_\mu^i(x) = \frac{1}{2}\bar{\psi}_1(x)\gamma_\mu\sigma^i\psi_1(x) \quad (2.18)$$

574 while the weak hypercharge conserved current resulting from the  $U(1)_Y$  symmetry is  
575 given by

$$J_\mu^Y = \sum_{j=1}^3 \bar{\psi}_j(x)\gamma_\mu y_j\psi_j(x) \quad (2.19)$$

576 In order to evaluate the electroweak interactions modeled by an isos triplet field  $W_\mu^i$   
577 which couples to isospin currents  $J_\mu^i$  with strength  $g$  and additionally the singlet  
578 field  $B_\mu$  which couples to the weak hypercharge current  $J_\mu^Y$  with strength  $g'/2$ . The  
579 interaction Lagrangian density to be considered is

$$\mathcal{L}_I = -g J^{i\mu}(x) W_\mu^i(x) - \frac{g'}{2} J^{Y\mu}(x) B_\mu(x) \quad (2.20)$$

580 Note that the weak isospin currents are not the same as the charged fermionic currents  
 581 that were used to describe the WI (eqn 2.7), since the weak isospin eigenstates are  
 582 not the same as the mass eigenstates, but they are closely related

$$J_\mu = \frac{1}{2}(J_\mu^1 + iJ_\mu^2), \quad J_\mu^\dagger = \frac{1}{2}(J_\mu^1 - iJ_\mu^2). \quad (2.21)$$

583 The same happens with the gauge fields  $W_\mu^i$  which are related to the mass eigenstates  
 584  $W^\pm$  by

$$W_\mu^+ = \frac{1}{\sqrt{2}}(W_\mu^1 - iW_\mu^2), \quad W_\mu^- = \frac{1}{\sqrt{2}}(W_\mu^1 + iW_\mu^2). \quad (2.22)$$

585 The fact that there are three weak isospin conserved currents is an indication that in  
 586 addition to the charged fermionic currents, which couple charged to neutral leptons,  
 587 there should be a neutral fermionic current that does not involve electric charge  
 588 exchange; therefore, it couples neutral fermions or fermions of the same electric charge.  
 589 The third weak isospin current contains a term that is similar to the electromagnetic  
 590 current ( $j_\mu^{em}$ ), indicating that there is a relation between them and resembling the  
 591 Gell-Mann-Nishijima formula 2.2 adapted to electroweak interactions

$$Q = T_3 + \frac{Y_W}{2}. \quad (2.23)$$

592 Just as  $Q$  generates the  $U(1)_{em}$  symmetry, the weak hypercharge generates the  $U(1)_Y$   
 593 symmetry as said before. It is possible to write the relationship in terms of the currents  
 594 as

$$j_\mu^{em} = J_\mu^3 + \frac{1}{2} J_\mu^Y. \quad (2.24)$$

595 The neutral gauge fields  $W_\mu^3$  and  $B_\mu$  cannot be directly identified with the  $Z$  and the  
 596 photon fields since the photon interacts similarly with left and right-handed fermions;  
 597 however, they are related through a linear combination given by

$$\begin{aligned} A_\mu &= B_\mu \cos \theta_W + W_\mu^3 \sin \theta_W \\ Z_\mu &= -B_\mu \sin \theta_W + W_\mu^3 \cos \theta_W \end{aligned} \quad (2.25)$$

598 where  $\theta_W$  is known as the “Weinberg angle.” The interaction Lagrangian is now given  
 599 by

$$\mathcal{L}_I = -\frac{g}{\sqrt{2}}(J^\mu W_\mu^+ + J^{\mu\dagger} W_\mu^-) - \left( g \sin \theta_W J_\mu^3 + g' \cos \theta_W \frac{J_\mu^Y}{2} \right) A^\mu - \left( g \cos \theta_W J_\mu^3 - g' \sin \theta_W \frac{J_\mu^Y}{2} \right) Z^\mu \quad (2.26)$$

600 the first term is the weak charged current interaction, while the second term is the  
 601 electromagnetic interaction under the condition

$$g \sin \theta_W = g' \cos \theta_W = e, \quad \frac{g'}{g} = \tan \theta_W \quad (2.27)$$

602 contained in the eqn.2.24; the third term is the neutral weak current.

603

604 Note that the neutral fields transformation given by the eqn. 2.25 can be written in  
 605 terms of the coupling constants  $g$  and  $g'$  as:

$$A_\mu = \frac{g' W_\mu^3 + g B_\mu}{\sqrt{g^2 + g'^2}}, \quad Z_\mu = \frac{g W_\mu^3 - g' B_\mu}{\sqrt{g^2 + g'^2}} \quad (2.28)$$

606 So far, the Lagrangian density describing the non-massive EWI is:

$$\mathcal{L}_{nmEWI} = \mathcal{L}_0 + \mathcal{L}_G \quad (2.29)$$

607 where fermion and gauge fields have been considered massless because their regular  
 608 mass terms are manifestly non invariant under  $G$  transformations; therefore, masses  
 609 have to be generated in a gauge invariant way. The mechanism by which this goal is  
 610 achieved is known as the “Higgs mechanism” and is closely connected to the concept  
 611 of “spontaneous symmetry breaking.”

### 612 2.3.1 Spontaneous symmetry breaking (SSB)

613 Figure 2.6 left shows a steel nail (top) which is subject to an external force; the form  
 614 of the potential energy is also shown (bottom).

615

616 Before reaching the critical force value, the system has rotational symmetry with re-  
 617 spect to the nail axis; however, after the critical force value is reached the nail buckles  
 618 (top right). The form of the potential energy (bottom right) changes, preserving its  
 619 rotational symmetry although its minima does not exhibit that rotational symmetry  
 620 any longer. Right before the nail buckles there is no indication of the direction the  
 621 nail will bend because any of the directions are equivalent, but once the nail bends,  
 622 choosing a direction, an arbitrary minimal energy state (ground state) is selected and  
 623 it does not share the system’s rotational symmetry. This mechanism for reaching an  
 624 asymmetric ground state is known as “*spontaneous symmetry breaking*”.

625 The lesson from this analysis is that the way to introduce the SSB mechanism into a  
 626 system is by adding the appropriate potential to it.

627

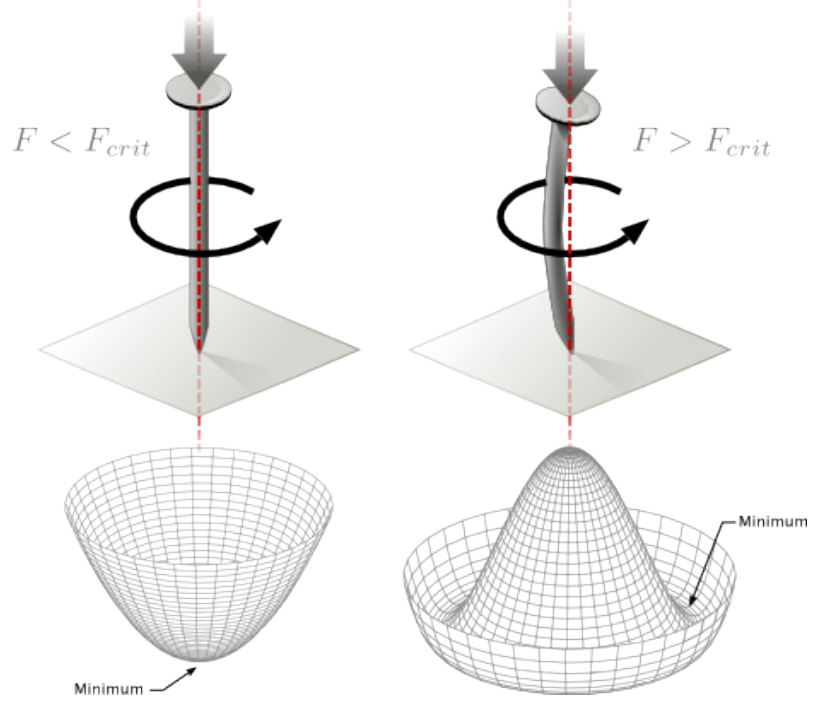


**Figure 2.6:** Spontaneous symmetry breaking mechanism. The steel nail, subject to an external force (top left), has rotational symmetry with respect to its axis. When the external force overcomes a critical value the nail buckles (top right) choosing a minimal energy state (ground state) and thus “*breaking spontaneously the rotational symmetry*”. The potential energy (bottom) changes but holds the rotational symmetry; however, an infinite number of asymmetric ground states are generated and circularly distributed in the bottom of the potential [27].

628 Figure 2.7 shows a plot of the potential  $V(\phi)$  in the case of a scalar field  $\phi$

$$V(\phi) = \mu^2 \phi^\dagger \phi + \lambda (\phi^\dagger \phi)^2 \quad (2.30)$$

629 If  $\mu^2 > 0$  the potential has only one minimum at  $\phi = 0$  and describes a scalar field  
 630 with mass  $\mu$ . If  $\mu^2 < 0$  the potential has a local maximum at  $\phi = 0$  and two minima  
 631 at  $\phi = \pm\sqrt{-\mu^2/\lambda}$  which enables the SSB mechanism to work.

632

633 In the case of a complex scalar field  $\phi(x)$

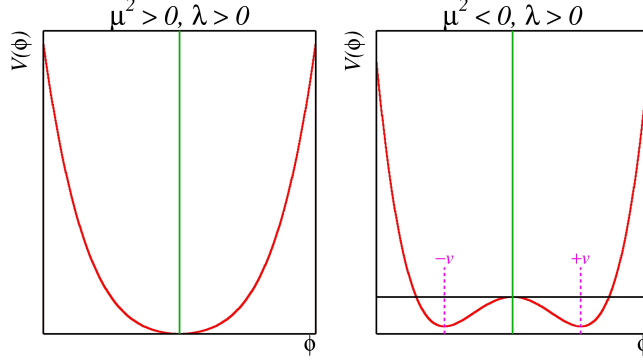


**Figure 2.7:** Shape of the potential  $V(\phi)$  for  $\lambda > 0$  and:  $\mu^2 > 0$  (left) and  $\mu^2 < 0$  (right). The case  $\mu^2 < 0$  corresponds to the potential suitable for introducing the SSB mechanism by choosing one of the two ground states which are connected via reflection symmetry. [27].

$$\phi(x) = \frac{1}{\sqrt{2}}(\phi_1 + i\phi_2) \quad (2.31)$$

634 the Lagrangian (invariant under global  $U(1)$  transformations) is given by

$$\mathcal{L} = (\partial_\mu \phi)^\dagger (\partial^\mu \phi) - V(\phi), \quad V(\phi) = \mu^2 \phi^\dagger \phi + \lambda (\phi^\dagger \phi)^2 \quad (2.32)$$

635 where an appropriate potential has been added in order to introduce the SSB.

636

637 As seen in figure 2.8, the potential has now an infinite number of minima circularly  
 638 distributed along the  $\xi$ -direction which makes possible the occurrence of the SSB by  
 639 choosing an arbitrary ground state; for instance,  $\xi = 0$ , i.e.  $\phi_1 = v, \phi_2 = 0$

$$\phi_0 = \frac{v}{\sqrt{2}} \exp(i\xi) \xrightarrow{\text{SSB}} \phi_0 = \frac{v}{\sqrt{2}} \quad (2.33)$$

640 As usual, excitations over the ground state are studied by making an expansion about

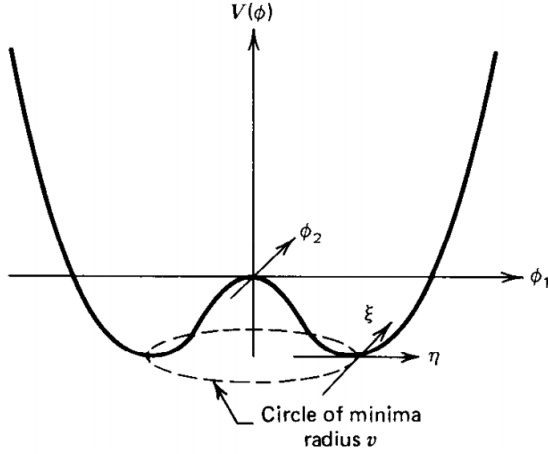


**Figure 2.8:** Potential for complex scalar field. There is a circle of minima of radius  $v$  along the  $\xi$ -direction [6].

641 it; thus, the excitation can be parametrized as:

$$\phi(x) = \frac{1}{\sqrt{2}}(v + \eta(x) + i\xi(x)) \quad (2.34)$$

642 which when substituted into eqn. 2.32 produces a Lagrangian in terms of the new  
643 fields  $\eta$  and  $\xi$

$$\mathcal{L}' = \frac{1}{2}(\partial_\mu \xi)^2 + \frac{1}{2}(\partial_\mu \eta)^2 + \mu^2 \eta^2 - V(\phi_0) - \lambda v \eta (\eta^2 + \xi^2) - \frac{\lambda}{4}(\eta^2 + \xi^2)^2 \quad (2.35)$$

644 where the last two terms represent the interactions and self-interaction between the  
645 two fields  $\eta$  and  $\xi$ . The particular feature of the SSB mechanism is revealed when  
646 looking to the first three terms of  $\mathcal{L}'$ . Before the SSB, only the massless  $\phi$  field is  
647 present in the system; after the SSB there are two fields of which the  $\eta$ -field has  
648 acquired mass  $m_\eta = \sqrt{-2\mu^2}$  while the  $\xi$ -field is still massless (see figure 2.9).

649

650 Thus, the SSB mechanism serves as a method to generate mass but as a side effect a

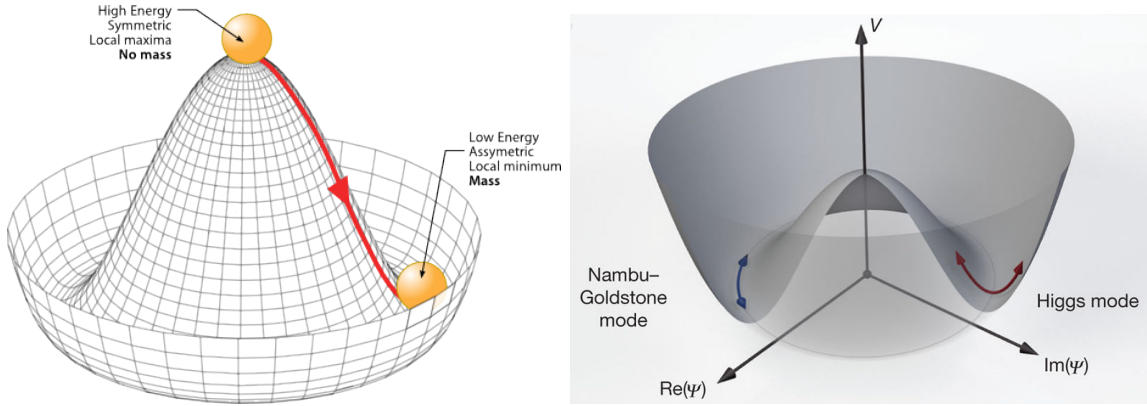


**Figure 2.9:** SSB mechanism for a complex scalar field [27, 28].

651 *massless field is introduced in the system.* This fact is known as the Goldstone theorem  
 652 and states that a massless scalar field appears in the system for each continuous  
 653 symmetry spontaneously broken. Another version of the Goldstone theorem states  
 654 that “*if a Lagrangian is invariant under a continuous symmetry group  $G$ , but the*  
 655 *vacuum is only invariant under a subgroup  $H \subset G$ , then there must exist as many*  
 656 *massless spin-0 particles (Nambu-Goldstone bosons) as broken generators.*” [26] The  
 657 Nambu-Goldstone boson can be understood considering that the potential in the  $\xi$ -  
 658 direction is flat so excitations in that direction are not energy consuming and thus  
 659 represent a massless state.

### 660 2.3.2 Higgs mechanism

661 When the SSB mechanism is introduced in the formulation of the EWI in an attempt  
 662 to generate the mass of the so far massless gauge bosons and fermions, an interesting  
 663 effect is revealed. In order to keep the  $G$  symmetry group invariance and generate  
 664 the mass of the EW gauge bosons, a  $G$  invariant Lagrangian density ( $\mathcal{L}_S$ ) has to be  
 665 added to the non massive EWI Lagrangian (eqn. 2.29)

$$\mathcal{L}_S = (D_\mu \phi)^\dagger (D^\mu \phi) - \mu^2 \phi^\dagger \phi - \lambda (\phi^\dagger \phi)^2, \quad \lambda > 0, \mu^2 < 0 \quad (2.36)$$

$$D_\mu \phi = \left( i\partial_\mu - g \frac{\sigma_i}{2} W_\mu^i - g' \frac{Y}{2} B_\mu \right) \phi \quad (2.37)$$

666  $\phi$  has to be an isospin doublet of complex scalar fields so it preserves the G invariance;  
 667 thus  $\phi$  can be defined as:

$$\phi = \begin{pmatrix} \phi^+ \\ \phi^0 \end{pmatrix} \equiv \frac{1}{\sqrt{2}} \begin{pmatrix} \phi_1 + i\phi_2 \\ \phi_3 + i\phi_4 \end{pmatrix}. \quad (2.38)$$

668 The minima of the potential are defined by

$$\phi^\dagger \phi = \frac{1}{2} (\phi_1^2 + \phi_2^2 + \phi_3^2 + \phi_4^2) = -\frac{\mu^2}{2\lambda}. \quad (2.39)$$

669 The choice of the ground state is critical. By choosing a ground state, invariant under  
 670  $U(1)_{em}$  gauge symmetry, the photon will remain massless and the  $W^\pm$  and  $Z$  bosons  
 671 masses will be generated which is exactly what is needed. In that sense, the best  
 672 choice corresponds to a weak isospin doublet with  $T_3 = -1/2$ ,  $Y_W = 1$  and  $Q = 0$   
 673 which defines a ground state with  $\phi_1 = \phi_2 = \phi_4$  and  $\phi_3 = v$ :

$$\phi_0 \equiv \frac{1}{\sqrt{2}} \begin{pmatrix} 0 \\ v \end{pmatrix}, \quad v^2 \equiv -\frac{\mu^2}{\lambda}. \quad (2.40)$$

674 where the vacuum expectation value  $v$  is fixed by the Fermi coupling  $G_F$  according  
 675 to  $v = (\sqrt{2}G_F)^{1/2} \approx 246$  GeV.

676

677 The G symmetry has been broken and three Nambu-Goldstone bosons will appear.

678 The next step is to expand  $\phi$  about the chosen ground state as:

$$\phi(x) = \frac{1}{\sqrt{2}} \exp\left(\frac{i}{v} \sigma_i \theta^i(x)\right) \begin{pmatrix} 0 \\ v + H(x) \end{pmatrix} \approx \frac{1}{\sqrt{2}} \begin{pmatrix} \theta_1(x) + i\theta_2(x) \\ v + H(x) - i\theta_3(x) \end{pmatrix} \quad (2.41)$$

679 to describe fluctuations from the ground state  $\phi_0$ . The fields  $\theta_i(x)$  represent the  
 680 Nambu-Goldstone bosons while  $H(x)$  is known as “higgs field.” The fundamental  
 681 feature of the parametrization used is that the dependence on the  $\theta_i(x)$  fields is  
 682 factored out in a global phase that can be eliminated by taking the physical “unitary  
 683 gauge”  $\theta_i(x) = 0$ . Therefore the expansion about the ground state is given by:

$$\phi(x) \frac{1}{\sqrt{2}} \begin{pmatrix} 0 \\ v + H(x) \end{pmatrix} \quad (2.42)$$

684 which when substituted into  $\mathcal{L}_S$  (eqn. 2.36) results in a Lagrangian containing the now  
 685 massive three gauge bosons  $W^\pm, Z$ , one massless gauge boson (photon) and the new  
 686 Higgs field ( $H$ ). The three degrees of freedom corresponding to the Nambu-Goldstone  
 687 bosons are now integrated into the massive gauge bosons as their longitudinal po-  
 688 larizations which were not available when they were massless particles. The effect  
 689 by which vector boson fields acquire mass after an spontaneous symmetry breaking,  
 690 but without an explicit gauge invariance breaking is known as the “*Higgs mechanism*”.

691

692 The mechanism was proposed by three independent groups: F.Englert and R.Brout  
 693 in August 1964 [29], P.Higgs in October 1964 [30] and G.Guralnik, C.Hagen and  
 694 T.Kibble in November 1964 [31]; however, its importance was not realized until  
 695 S.Glashow [22], A.Salam [23] and S.Weinberg [24], independently, proposed that elec-  
 696 tromagnetic and weak interactions are two manifestations of a more general interac-  
 697 tion called “electroweak interaction” in 1967.

### 698 2.3.3 Masses of the gauge bosons

699 The mass of the gauge bosons is extracted by evaluating the kinetic part of Lagrangian  
 700  $\mathcal{L}_S$  in the ground state (known also as the vacuum expectation value), i.e.,

$$\left| \left( \partial_\mu - ig \frac{\sigma_i}{2} W_\mu^i - i \frac{g'}{2} B_\mu \right) \phi_0 \right|^2 = \left( \frac{1}{2} v g \right)^2 W_\mu^+ W^{-\mu} + \frac{1}{8} v^2 (W_\mu^3, B_\mu) \begin{pmatrix} g^2 & -gg' \\ -gg' & g'^2 \end{pmatrix} \begin{pmatrix} W^{3\mu} \\ B^\mu \end{pmatrix} \quad (2.43)$$

701 comparing with the typical mass term for a charged boson  $M_W^2 W^+ W^-$

$$M_W = \frac{1}{2} v g. \quad (2.44)$$

The second term in the right side of the eqn.2.43 comprises the masses of the neutral bosons, but it needs to be written in terms of the gauge fields  $Z_\mu$  and  $A_\mu$  in order to be compared to the typical mass terms for neutral bosons, therefore using eqn. 2.28

$$\begin{aligned} \frac{1}{8} v^2 [g^2 (W_\mu^3)^2 - 2gg' W_\mu^3 B^\mu + g'^2 B_\mu^2] &= \frac{1}{8} v^2 [g W_\mu^3 - g' B_\mu]^2 + 0[g' W_\mu^3 + g B_\mu]^2 \quad (2.45) \\ &= \frac{1}{8} v^2 [\sqrt{g^2 + g'^2} Z_\mu]^2 + 0[\sqrt{g^2 + g'^2} A_\mu]^2 \end{aligned}$$

702 and then

$$M_Z = \frac{1}{2} v \sqrt{g^2 + g'^2}, \quad M_A = 0 \quad (2.46)$$

703 **2.3.4 Masses of the fermions**

704 The lepton mass terms can be generated by introducing a gauge invariant Lagrangian  
 705 term describing the Yukawa coupling between the lepton field and the Higgs field

$$\mathcal{L}_{Yl} = -G_l \left[ (\bar{\nu}_l, \bar{l})_L \begin{pmatrix} \phi^+ \\ \phi^0 \end{pmatrix} l_R + \bar{l}_R (\phi^-, \bar{\phi}^0) \begin{pmatrix} \nu_l \\ l \end{pmatrix}_L \right], \quad l = e, \mu, \tau. \quad (2.47)$$

706 After the SSB and replacing the usual field expansion about the ground state (eqn.2.40)  
 707 into  $\mathcal{L}_{Yl}$ , the mass term arises

$$\mathcal{L}_{Yl} = -m_l (\bar{l}_L l_R + \bar{l}_R l_L) - \frac{m_l}{v} (\bar{l}_L l_R + \bar{l}_R l_L) H = -m_l \bar{l} l \left( 1 + \frac{H}{v} \right) \quad (2.48)$$

708

$$m_l = \frac{G_l}{\sqrt{2}} v \quad (2.49)$$

709 where the additional term represents the lepton-Higgs interaction. The quark masses  
 710 are generated in a similar way as lepton masses but for the upper member of the  
 711 quark doublet a different Higgs doublet is needed:

$$\phi_c = -i\sigma_2 \phi^* = \begin{pmatrix} -\bar{\phi}^0 \\ \phi^- \end{pmatrix}. \quad (2.50)$$

712 Additionally, given that the quark isospin doublets are not constructed in terms of  
 713 the mass eigenstates but in terms of the flavor eigenstates, as shown in table2.5, the  
 714 coupling parameters will be related to the CKM matrix elements; thus the quark  
 715 Lagrangian is given by:

$$\mathcal{L}_{Yq} = -G_d^{i,j} (\bar{u}_i, \bar{d}'_i)_L \begin{pmatrix} \phi^+ \\ \phi^0 \end{pmatrix} d_{jR} - G_u^{i,j} (\bar{u}_i, \bar{d}'_i)_L \begin{pmatrix} -\bar{\phi}^0 \\ \phi^- \end{pmatrix} u_{jR} + h.c. \quad (2.51)$$

716 with  $i,j=1,2,3$ . After SSB and expansion about the ground state, the diagonal form

717 of  $\mathcal{L}_{Yq}$  is:

$$\mathcal{L}_{Yq} = -m_d^i \bar{d}_i d_i \left(1 + \frac{H}{v}\right) - m_u^i \bar{u}_i u_i \left(1 + \frac{H}{v}\right) \quad (2.52)$$

718 Fermion masses depend on arbitrary couplings  $G_l$  and  $G_{u,d}$  and are not predicted by  
719 the theory.

### 720 2.3.5 The Higgs field

721 After the characterization of the fermions and gauge bosons as well as their interac-  
722 tions, it is necessary to characterize the Higgs field itself. The Lagrangian  $\mathcal{L}_S$  in eqn.  
723 2.36 written in terms of the gauge bosons is given by

$$\mathcal{L}_S = \frac{1}{4} \lambda v^4 + \mathcal{L}_H + \mathcal{L}_{HV} \quad (2.53)$$

724

$$\mathcal{L}_H = \frac{1}{2} \partial_\mu H \partial^\mu H - \frac{1}{2} m_H^2 H^2 - \frac{1}{2v} m_H^2 H^3 - \frac{1}{8v^2} m_H^2 H^4 \quad (2.54)$$

725

$$\mathcal{L}_{HV} = m_H^2 W_\mu^+ W^{\mu-} \left(1 + \frac{2}{v} H + \frac{2}{v^2} H^2\right) + \frac{1}{2} m_Z^2 Z_\mu Z^\mu \left(1 + \frac{2}{v} H + \frac{2}{v^2} H^2\right) \quad (2.55)$$

726 The mass of the Higgs boson is deduced as usual from the mass term in the Lagrangian  
727 resulting in:

$$m_H = \sqrt{-2\mu^2} = \sqrt{2\lambda}v \quad (2.56)$$

728 however, it is not predicted by the theory either. The experimental efforts to find  
729 the Higgs boson, carried out by the “Compact Muon Solenoid (CMS)” experiment  
730 and the “A Toroidal LHC AppartuS (ATLAS)” experiments at the “Large Hadron  
731 Collider(LHC)”, gave great results by July of 2012 when the discovery of a new  
732 particle compatible with the Higgs boson predicted by the electroweak theory [32, 33]  
733 was announced. Although at the announcement time there were some reservations  
734 about calling the new particle the “Higgs boson”, today this name is widely accepted.

735 The Higgs mass measurement, reported by both experiments [34], is in table 2.8.

Property	Value
Electric charge	0
Colour charge	0
Spin	0
Weak isospin	-1/2
Weak hypercharge	1
Parity	1
Mass ( $\text{GeV}/c^2$ )	$125.09 \pm 0.21 \text{ (stat.)} \pm 0.11 \text{ (syst.)}$

**Table 2.8:** Higgs boson properties. Higgs mass is not predicted by the theory and the value here corresponds to the experimental measurement.

736

### 737 2.3.6 Production of Higgs bosons at LHC

738 At LHC, Higgs boson is produced as a result of the collision of two counter-rotating  
 739 protons beams. A detailed description of the LHC machine will be presented in  
 740 chapter 3. “The total cross section” is a parameter that quantifies the number of pp  
 741 collisions that happen when a number of protons are fired at each other. Different  
 742 results can be obtained after a pp collision and for each one the “cross section” is  
 743 defined as the number of pp collisions that conclude in that particular result with  
 744 respect to the number of protons fired at each other.

745 Protons are composed of quarks and these quarks are bound by gluons; however,  
 746 what is commonly called the quark content of the proton makes reference to the  
 747 valence quarks. A sea of quarks and gluons is also present inside the proton as repre-  
 748 sented in figure 2.10. In a proton-proton (pp) collision, the constituents (quarks and  
 749 gluons) are those who collide. The pp cross section depends on the momentum of  
 750 the colliding particles, reason for which it is needed to know how the momentum is  
 751 distributed inside the proton. Quarks and gluons are known as partons and the func-  
 752 tions that describe how the proton momentum is distributed among partons inside it

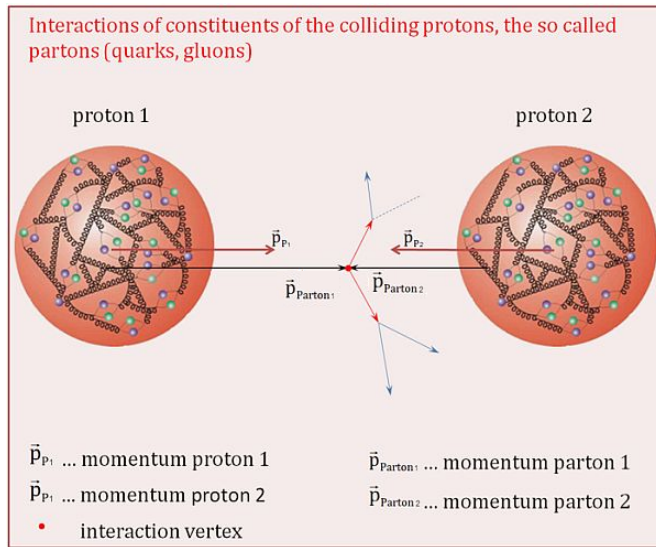


**Figure 2.10:** Proton-proton collision. Protons are composed of 3 valence quarks, a sea of quarks and gluons; therefore in a proton-proton collision, quarks and gluons are those who collide. [35].

753 are called “parton distribution functions (PDFs)”; PDFs are determined from experi-

754 mental data obtained in experiments where the internal structure of hadrons is tested.

755

In addition, in physics, a common approach to study complex systems consists in starting with a simpler version of them, for which a well known description is available, and add an additional “perturbation” which represents a small deviation from the known behavior. If the perturbation is small enough, the physical quantities associated with the perturbed system are expressed as a series of corrections to those of the simpler system; therefore, the more terms are considered in the series (the higher order in the perturbation series), the more precise is the description of the complex system.

764

765 This thesis explores the Higgs production at LHC; therefore the overview presented  
766 here will be oriented specifically to the production mechanisms after pp collisions at

767 LHC.

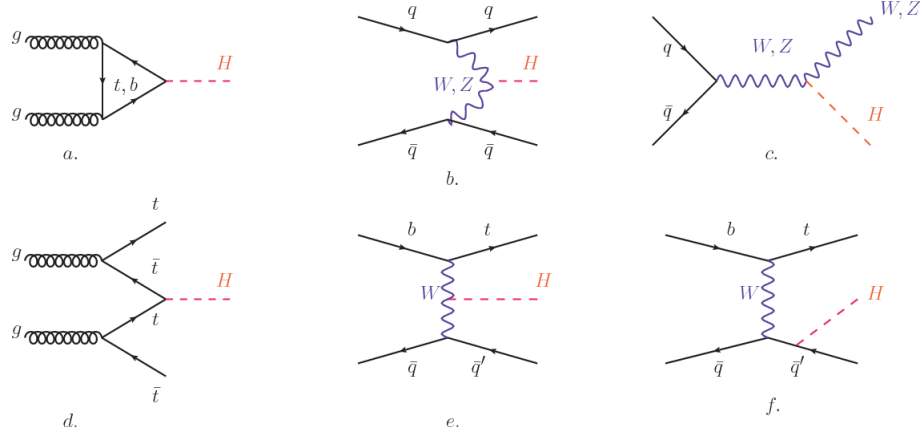


**Figure 2.11:** Main Higgs boson production mechanism Feynman diagrams. a. gluon-gluon fusion, b. vector boson fusion (VBF), c. Higgs-strahlung, d. Associated production with a top or bottom quark pair, e-f. associated production with a single top quark.

768 Figure 2.11 shows the Feynman diagrams for the leading order (first order) Higgs  
 769 production processes at LHC, while the cross section for Higgs production as a func-  
 770 tion of the center of mass-energy ( $\sqrt{s}$ ) for pp collisions is showed in figure 2.12 left.  
 771 The tags NLO (next to leading order), NNLO (next to next to leading order) and  
 772 N3LO (next to next to next to leading order) make reference to the order at which  
 773 the perturbation series have been considered.

774 As shown in eqns 2.47, 2.51 and 2.55, the strength of the Higgs-fermion interaction  
 775 is proportional to the fermion mass while the strength of the Higgs-gauge boson  
 776 interaction is proportional to the square of the gauge boson mass, which implies  
 777 that the Higgs production and decay mechanisms are dominated by couplings  $H -$   
 778  $(W, Z, t, b, \tau)$ .

779 The main production mechanism is the gluon fusion (figure 2.11a and  $pp \rightarrow H$  in figure  
 780 2.12) given that gluons carry the highest fraction of momentum of the protons in pp  
 781 colliders. Since the Higgs boson does not couple to gluons, the mechanism proceeds  
 782 through the exchange of a virtual top-quark loop given that for it the coupling is

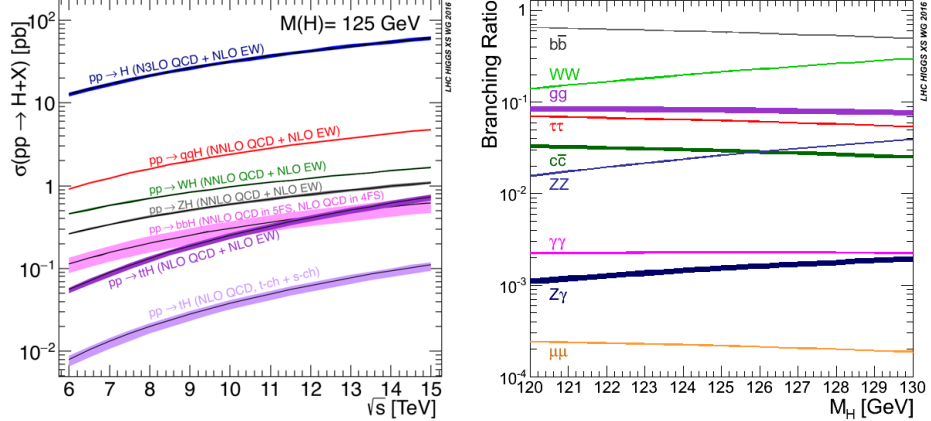


**Figure 2.12:** Higgs boson production cross sections (left) and decay branching ratios (right) for the main mechanisms. The VBF is indicated as  $qqH$  [36].

the biggest. Note that in this process, the Higgs boson is produced alone, which makes this mechanism experimentally clean when combined with the two-photon or the four-lepton decay channels (see section 2.3.7).

Vector boson fusion (figure 2.11b and  $pp \rightarrow qqH$  in figure 2.12) has the second largest production cross section. The scattering of two fermions is mediated by a weak gauge boson which later emits a Higgs boson. In the final state, the two fermions tend to be located in a particular region of the detector which is used as a signature when analyzing the datasets provided by the experiments. More details about how to identify events of interest in an analysis will be given in chapter 6.

The next production mechanism is Higgs-strahlung (figure 2.11c and  $pp \rightarrow WH, pp \rightarrow ZH$  in figure 2.12) where two fermions annihilate to form a weak gauge boson. If the initial fermions have enough energy, the emergent boson eventually will emit a Higgs boson.

The associated production with a top or bottom quark pair and the associated production with a single top quark (figure 2.11d-f and  $pp \rightarrow bbH, pp \rightarrow t\bar{t}H, pp \rightarrow tH$  in figure 2.12) have a smaller cross section than the main three mechanisms above,

799 but they provide a good opportunity to test the Higgs-top coupling. The analysis  
 800 reported in this thesis is developed using these production mechanisms. A detailed  
 801 description of the  $tH$  mechanism will be given in section 2.4.

### 802 2.3.7 Higgs boson decay channels

803 When a particle can decay through several modes, also known as channels, the  
 804 probability of decaying through a given channel is quantified by the “branching ratio  
 805 (BR)” of the decay channel; thus, the BR is defined as the ratio of number of decays  
 806 going through that given channel to the total number of decays. In regard to the  
 807 Higgs boson decay, the BR can be predicted with accuracy once the Higgs mass is  
 808 known [37, 38]. In figure 2.12 right, a plot of the BR as a function of the Higgs mass  
 809 is presented. The largest predicted BR corresponds to the  $b\bar{b}$  pair decay channel (see  
 810 table 2.9).

Decay channel	Branching ratio	Rel. uncertainty
$H \rightarrow b\bar{b}$	$5.84 \times 10^{-1}$	$+3.2\% - 3.3\%$
$H \rightarrow W^+W^-$	$2.14 \times 10^{-1}$	$+4.3\% - 4.2\%$
$H \rightarrow \tau^+\tau^-$	$6.27 \times 10^{-2}$	$+5.7\% - 5.7\%$
$H \rightarrow ZZ$	$2.62 \times 10^{-2}$	$+4.3\% - 4.1\%$
$H \rightarrow \gamma\gamma$	$2.27 \times 10^{-3}$	$+5.0\% - 4.9\%$
$H \rightarrow Z\gamma$	$1.53 \times 10^{-3}$	$+9.0\% - 8.9\%$
$H \rightarrow \mu^+\mu^-$	$2.18 \times 10^{-4}$	$+6.0\% - 5.9\%$

**Table 2.9:** Predicted branching ratios and the relative uncertainty for a SM Higgs boson with  $m_H = 125 GeV/c^2$ . [9]

812 **2.4 Associated production of a Higgs boson and a  
813 single Top quark.**

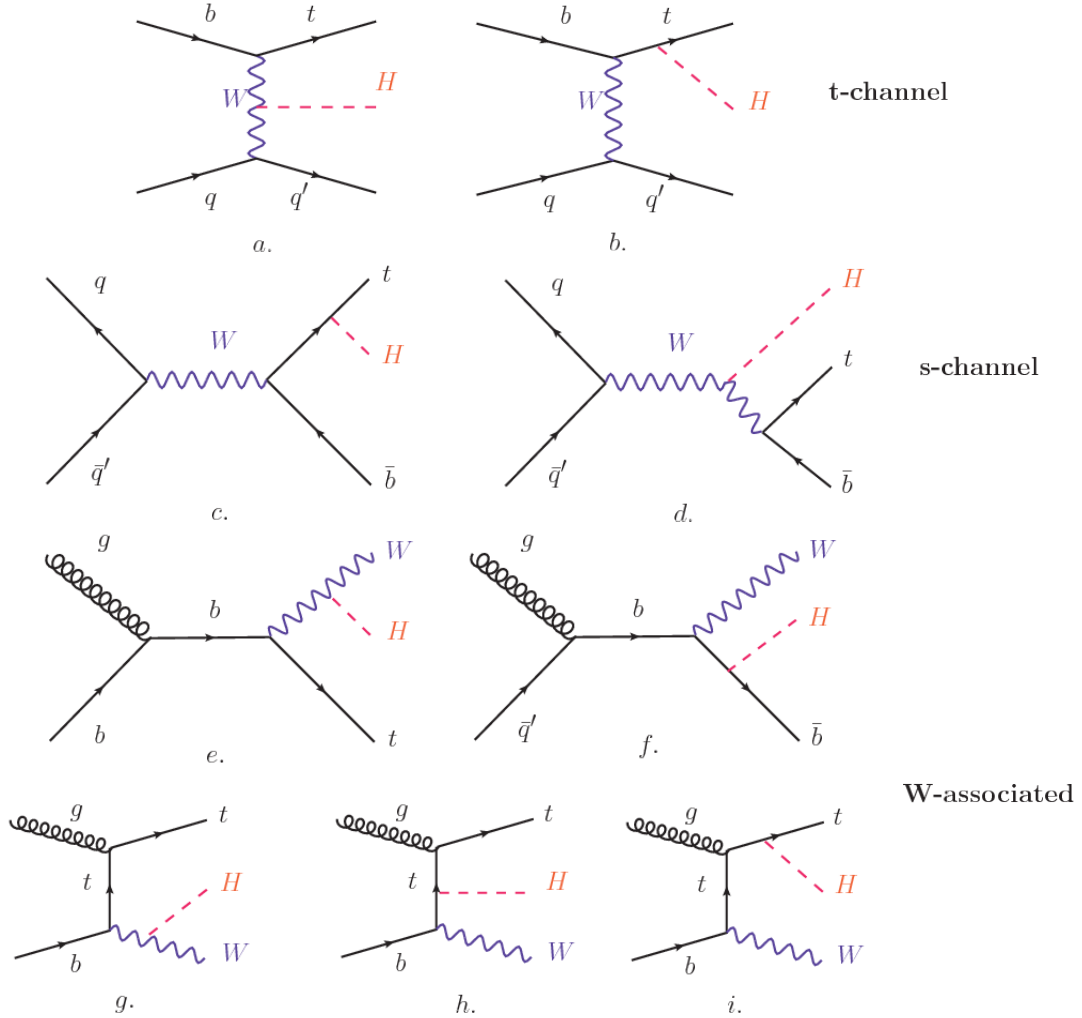


**Figure 2.13:** Associated Higgs boson production mechanism Feynman diagrams. a.,b. t-channel (tHq), c.,d. s-channel (tHb), e-i. W-associated.

814 Associated production of Higgs boson has been extensively studied [39–43]. While  
815 measurements of the main Higgs production mechanisms rates are sensitive to the  
816 strength of the Higgs coupling to W boson or top quark, they are not sensitive to the  
817 relative sign between the two couplings. In this thesis, the Higgs boson production

818 mechanism explored is the associated production with a single top quark (*th*) which  
 819 offers sensitiveness to the relative sign of the Higgs couplings to W boson and to top  
 820 quark. The description given here is based on the reference [41]

821

822 A process where two incoming particles interact and produce a final state with two  
 823 particles can proceed in three ways also called channels (see, for instance, figure 2.13  
 824 ommiting the red line). The t-channel represents processes where an intermediate  
 825 particle is emitted by one of the incoming particles and absorbed by the other. The  
 826 s-channel represents processes where the two incoming particles merge into an inter-  
 827 mediate particle which eventually will split into the particles in the final state. The  
 828 third channel, u-channel, is similar to the t-channel but the two outgoing particles  
 829 interchange their roles.

830

831 The *th* production, where Higgs boson can be radiated either from the top quark or  
 832 from the W boson, is represented by the leading order Feynman diagrams in figure  
 833 2.13. The cross section for the *th* process is calculated, as usual, summing over  
 834 the contributions from the different feynman diagrams; therefore it depends on the  
 835 interference between the contributions. In the SM, the interference for t-channel (tHq  
 836 process) and W-associated (tHW process) production is destructive [39] resulting in  
 837 the small cross sections presented in table 2.10.

tH production channel	Cross section (fb)
t-channel ( $pp \rightarrow tHq$ )	$70.79^{+2.99}_{-4.80}$
W-associated ( $pp \rightarrow tHW$ )	$15.61^{+0.83}_{-1.04}$
s-channel( $pp \rightarrow tHb$ )	$2.87^{+0.09}_{-0.08}$

**Table 2.10:** Predicted SM cross sections for *tH* production at  $\sqrt{s} = 13$  TeV [44, 45].

838

839 While the s-channel contribution can be neglected, it will be shown that a deviation  
 840 from the SM destructive interference would result in an enhancement of the  $th$  cross  
 841 section compared to that in SM, which could be used to get information about the  
 842 sign of the Higgs-top coupling [41, 42]. In order to describe  $th$  production processes,  
 843 Feynman diagram 2.13b will be considered; there, the W boson is radiated by a  
 844 quark in the proton and eventually it will interact with the b quark. In the high  
 845 energy regime, the effective W approximation [46] allows to describe the process as  
 846 the emmision of an approximately on-shell W and its hard scattering with the b  
 847 quark; i.e.  $Wb \rightarrow th$ . The scattering amplitude for the process is given by

$$\mathcal{A} = \frac{g}{\sqrt{2}} \left[ (\kappa_t - \kappa_V) \frac{m_t \sqrt{s}}{m_W v} A \left( \frac{t}{s}, \varphi; \xi_t, \xi_b \right) + \left( \kappa_V \frac{2m_W s}{v} \frac{1}{t} + (2\kappa_t - \kappa_V) \frac{m_t^2}{m_W v} \right) B \left( \frac{t}{s}, \varphi; \xi_t, \xi_b \right) \right], \quad (2.57)$$

848 where  $\kappa_V \equiv g_{HVV}/g_{HVV}^{SM}$  and  $\kappa_t \equiv g_{Ht}/g_{Ht}^{SM} = y_t/y_t^{SM}$  are scaling factors that quan-  
 849 tify possible deviations of the couplings, Higgs-Vector boson (H-W) and Higgs-top  
 850 (H-t) respectively, from the SM couplings;  $s = (p_W + p_b)^2$ ,  $t = (p_W - p_H)^2$ ,  $\varphi$  is the  
 851 Higgs azimuthal angle around the  $z$  axis taken parallel to the direction of motion of  
 852 the incoming W; A and B are funtions describing the weak interaction in terms of  
 853 the chiral states of the quarks  $b$  and  $t$ . Terms that vanish in the high energy limit  
 854 have been neglected as well as the Higgs and  $b$  quark masses<sup>8</sup>.

855

856 The scattering amplitude grows with energy like  $\sqrt{s}$  for  $\kappa_V \neq \kappa_t$ , in contrast to  
 857 the SM ( $\kappa_t = \kappa_V = 1$ ), where the first term in 2.57 cancels out and the amplitude  
 858 is constant for large  $s$ ; therefore, a deviation from the SM predictions represents an  
 859 enhancement in the  $tHq$  cross section. In particular, for a SM H-W coupling and a H-t

---

<sup>8</sup> A detailed explanation of the structure and approximations used to derive  $\mathcal{A}$  can be found in reference [41]

860 coupling of inverted sign with respect to the SM ( $\kappa_V = -\kappa_t = 1$ ) the  $tHq$  cross section  
 861 is enhanced by a factor greater 10 as seen in the figure 2.14 taken from reference [41];  
 862 reference [47] has reported similar enhancement results.

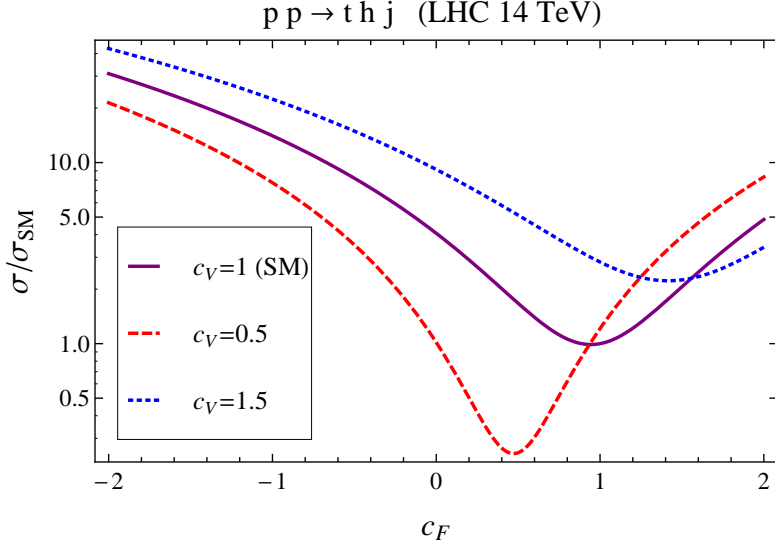


**Figure 2.14:** Cross section for  $tHq$  process as a function of  $\kappa_t$ , normalized to the SM, for three values of  $\kappa_V$ . In the plot  $c_f$  refers to the Higgs-fermion coupling which is dominated by the H-t coupling and represented here by  $\kappa_t$ . Solid, dashed and dotted lines correspond to  $c_V \rightarrow \kappa_V = 1, 0.5, 1.5$  respectively. Note that for the SM ( $\kappa_V = \kappa_t = 1$ ), the destructive effect of the interference is maximal.

863 A similar analysis is valid for the W-associated channel but, in that case, the inter-  
 864 ference is more complicated since there are more than two contributions and an ad-  
 865 ditional interference with the production of Higgs boson and a top pair process( $t\bar{t}H$ ).  
 866 The calculations are made using the so-called Diagram Removal (DR) technique where  
 867 interfering diagrams are removed (or added) from the calculations in order to evaluate  
 868 the impact of the removed contributions. DR1 was defined to neglect  $t\bar{t}H$  interference  
 869 while DR2 was defined to take  $t\bar{t}H$  interference into account [48]. As shown in figure  
 870 2.15, the  $tHW$  cross section is enhanced from about 15 fb (SM:  $\kappa_{Htt} = 1$ ) to about  
 871 150 fb ( $\kappa_{Htt} = -1$ ). Differences between curves for DR1 and DR2 help to gauge the  
 872 impact of the interference with  $t\bar{t}H$ .

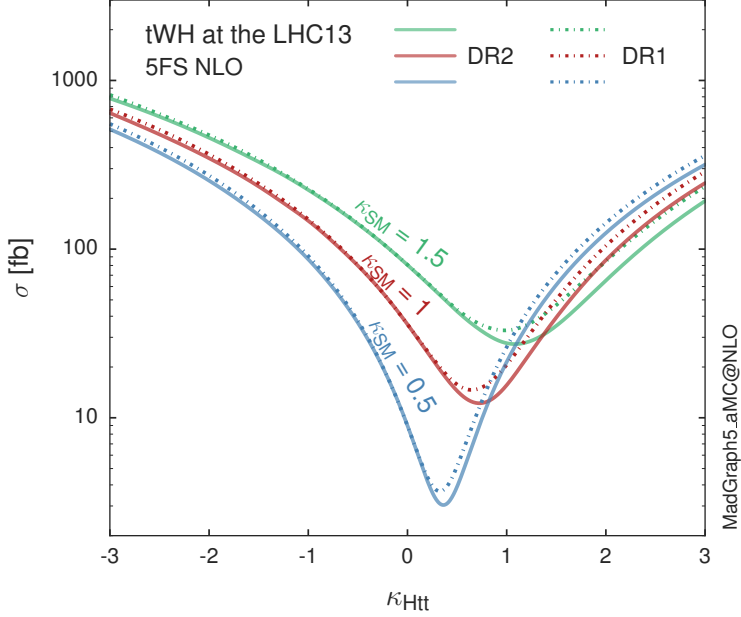


**Figure 2.15:** Cross section for  $tHW$  process as a function of  $\kappa_{Htt}$ , for three values of  $\kappa_{SM}$  at  $\sqrt{s} = 13$  TeV.  $\kappa_{Htt}^2 = \sigma_{Htt}/\sigma_{Htt}^{SM}$  is a simple rescaling of the SM Higgs interactions.

873 Results of the calculations of the  $tHq$  and  $tHW$  cross sections at  $\sqrt{s} = 13$  TeV can be  
 874 found in reference [49] and a summary of the results is presented in table 2.11.

875

## 876 2.5 The CP-mixing in tH processes

877 In addition to the sensitivity to sign of the H-t coupling,  $tHq$  and  $tHW$  processes have  
 878 been proposed as a tool to investigate the possibility of a H-t coupling that does not  
 879 conserve CP [43, 48, 50]. Current experimental results are consistent with SM H-V  
 880 and H-t couplings; however, negative H-t coupling is not excluded completely [53].

881

882 In this thesis, the sensitivity of  $th$  processes to CP-mixing is also studied in the  
 883 effective field theory framework and based in references [43, 48]; a generic particle

	$\sqrt{s}$ TeV	$\kappa_t = 1$	$\kappa_t = -1$
$\sigma^{LO}(tHq)(\text{fb})$ [41]	8	$\approx 17.4$	$\approx 252.7$
	14	$\approx 80.4$	$\approx 1042$
$\sigma^{NLO}(tHq)(\text{fb})$ [41]	8	$18.28^{+0.42}_{-0.38}$	$233.8^{+4.6}_{-0.0}$
	14	$88.2^{+1.7}_{-0.0}$	$982.8^{+28}_{-0.0}$
$\sigma^{LO}(tHq)(\text{fb})$ [47]	14	$\approx 71.8$	$\approx 893$
$\sigma^{LO}(tHW)(\text{fb})$ [47]	14	$\approx 16.0$	$\approx 139$
$\sigma^{NLO}(tHq)(\text{fb})$ [49]	8	$18.69^{+8.62\%}_{-17.13\%}$	-
	13	$74.25^{+7.48\%}_{-15.35\%}$	$848^{+7.37\%}_{-13.70\%}$
	14	$90.10^{+7.34\%}_{-15.13\%}$	$1011^{+7.24\%}_{-13.39\%}$
$\sigma^{LO}(tHW)(\text{fb})$ [48]	13	$15.77^{+15.91\%}_{-15.76\%}$	-
$\sigma^{NLO} DR1(tHW)(\text{fb})$ [48]	13	$21.72^{+6.52\%}_{-5.24\%}$	$\approx 150$
$\sigma^{NLO} DR2(tHW)(\text{fb})$ [48]	13	$16.28^{+7.34\%}_{-15.13\%}$	$\approx 150$

**Table 2.11:** Predicted enhancement of the  $tHq$  and  $tHW$  cross sections at LHC for  $\kappa_V = 1$  and  $\kappa_t = \pm 1$  at LO and NLO; the cross section enhancement of more than a factor of 10 is due to the flippling in the sign of the H-t coupling with respect to the SM one.

884 ( $X_0$ ) of spin-0 and a general CP violating interaction with the top quark, can couple  
 885 to scalar and pseudoscalar fermionic densities. The H-W interaction is assumed to  
 886 be SM-like. The Lagrangian modeling the H-t interaction is given by

$$\mathcal{L}_0^t = -\bar{\psi}_t (c_\alpha \kappa_{Htt} g_{Htt} + i s_\alpha \kappa_{Att} g_{Att} \gamma_5) \psi_t X_0, \quad (2.58)$$

887 where  $\alpha$  is the CP-mixing phase,  $c_\alpha \equiv \cos \alpha$  and  $s_\alpha \equiv \sin \alpha$ ,  $\kappa_{Htt}$  and  $\kappa_{Att}$  are real  
 888 dimensionless rescaling parameters<sup>9</sup>,  $g_{Htt} = g_{Att} = m_t/v = y_t/\sqrt{2}$  and  $v \sim 246$  GeV is  
 889 the Higgs vacuum expectation value. In this parametrization, it is easy to recover  
 890 three special cases

891 • CP-even coupling  $\rightarrow \alpha = 0^\circ$

892 • CP-odd coupling  $\rightarrow \alpha = 90^\circ$

893 • SM coupling  $\rightarrow \alpha = 0^\circ$  and  $\kappa_{Htt} = 1$

---

<sup>9</sup> analog to  $\kappa_t$  and  $\kappa_V$

894 The loop induced  $X_0$  coupling to gluons can also be described in terms of the  
 895 parametrization above, according to

$$\mathcal{L}_0^g = -\frac{1}{4} \left( c_\alpha \kappa_{Hgg} g_{Hgg} G_{\mu\nu}^a G^{a,\mu\nu} + s_\alpha \kappa_{Agg} g_{Agg} G_{\mu\nu}^a \tilde{G}^{a,\mu\nu} \right) X_0. \quad (2.59)$$

896 where  $g_{Hgg} = -\alpha_s/3\pi v$  and  $g_{Agg} = \alpha_s/2\pi v$ . Under the assumption that the top quark  
 897 dominates the gluon-fusion process at LHC energies,  $\kappa_{Hgg} \rightarrow \kappa_{Htt}$  and  $\kappa_{Agg} \rightarrow \kappa_{Att}$ ,  
 898 so that the ratio between the gluon-gluon fusion cross section for  $X_0$  and for the SM  
 899 Higgs prediction can be written as

$$\frac{\sigma_{NLO}^{gg \rightarrow X_0}}{\sigma_{NLO,SM}^{gg \rightarrow H}} = c_\alpha^2 \kappa_{Htt}^2 + s_\alpha^2 \left( \kappa_{Att} \frac{g_{Agg}}{g_{Hgg}} \right)^2. \quad (2.60)$$

900 If the rescaling parameters are set to

$$\kappa_{Htt} = 1, \quad \kappa_{Att} = \left| \frac{g_{Hgg}}{g_{Agg}} \right| = \frac{2}{3}. \quad (2.61)$$

901 the gluon-fusion SM cross section is reproduced for every value of the CP-mixing  
 902 angle  $\alpha$ ; therefore, by imposing that condition to the Lagrangian density 2.58, the  
 903 CP-mixing angle is not constrained by current data. Figure 2.16 shows the NLO cross  
 904 sections for t-channel  $tX_0$  (blue) and  $t\bar{t}X_0$  (red) associated production processes as  
 905 a function of the CP-mixing angle  $\alpha$ .  $X_0$  is a generic spin-0 particle with top quark  
 906 CP-violating coupling. Rescaling factors  $\kappa_{Htt}$  and  $\kappa_{Att}$  have been set to reproduce  
 907 the SM gluon-fusion cross sections.

908 It is interesting to notice that the  $tX_0$  cross section is enhanced, by a factor of  
 909 about 10, when a continuous rotation in the scalar-pseudoscalar plane is applied; this  
 910 enhancement is similar to the enhancement produced when the H-t coupling is flipped  
 911 in sign with respect to the SM ( $y_t = -y_{t,SM}$  in the plot), as showed in section 2.4. In

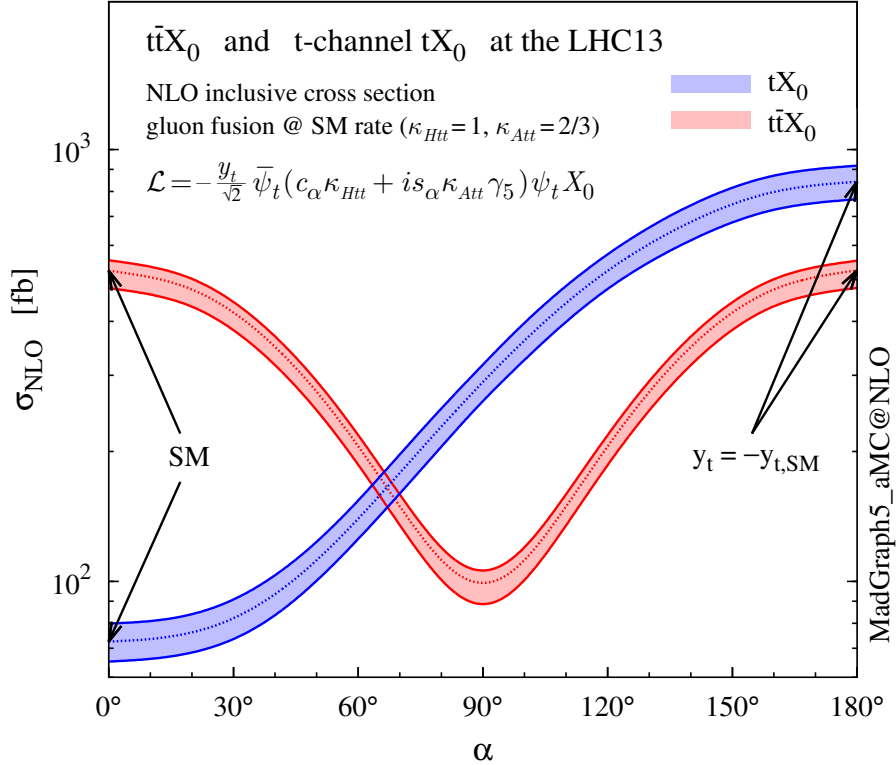


**Figure 2.16:** NLO cross sections for t-channel  $tX_0$  (blue) and  $t\bar{t}X_0$  (red) associated production processes as a function of the CP-mixing angle  $\alpha$ .  $X_0$  is a generic spin-0 particle with top quark CP-violating coupling [43].

contrast, the degeneracy in the  $t\bar{t}X_0$  cross section is still present given that it depends quadratically on the H-t coupling, but more interesting is to notice that  $t\bar{t}X_0$  cross section is exceeded by  $tX_0$  cross section after  $\alpha \sim 60^\circ$ .

A similar parametrization can be used to investigate the  $tHW$  process sensitivity to CP-violating H-t coupling. As said in 2.4, the interference in the W-associated channel is more complicated because there are more than two contributions and also there is interference with the  $t\bar{t}H$  production process.

919

920 Figure 2.17 shows the NLO cross sections for t-channel  $tX_0$  (blue),  $t\bar{t}X_0$  (red) associated production and for the combined  $tWX_0 + t\bar{t}X_0 +$  interference (orange) as a

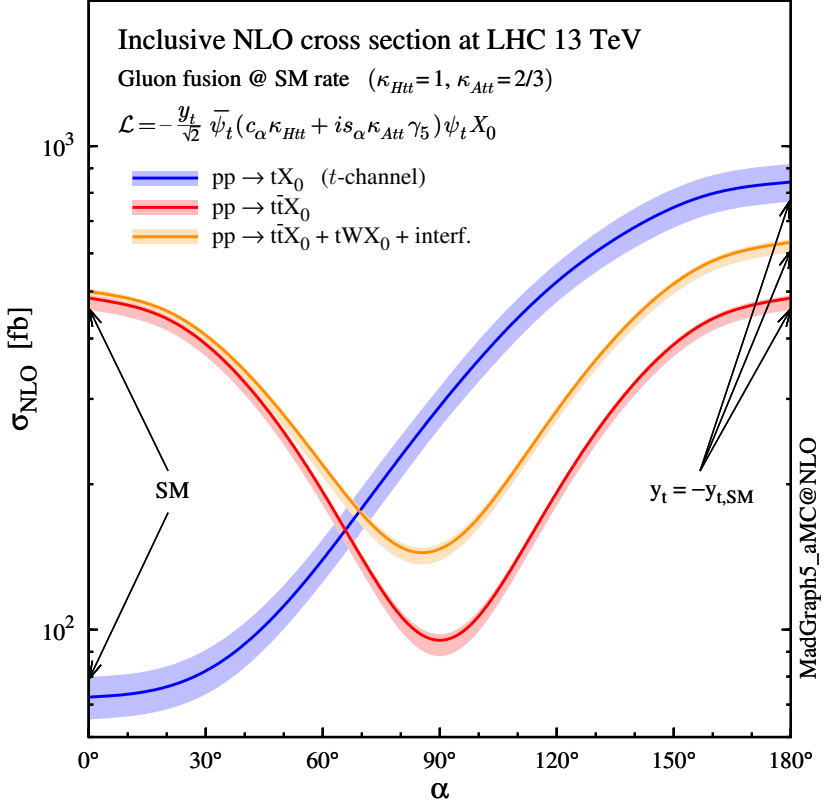


**Figure 2.17:** NLO cross sections for t-channel  $tX_0$  (blue),  $t\bar{t}X_0$  (red) associated production processes and combined  $tWX_0 + t\bar{t}X_0$  (including interference) production as a function of the CP-mixing angle  $\alpha$  [43].

function of the CP-mixing angle. It is clear that the effect of the interference in the combined case is the lifting of the degeneracy present in the  $t\bar{t}X_0$  production. The constructive interference enhances the cross section from about 500 fb at SM ( $\alpha = 0$ ) to about 600 fb ( $\alpha = 180^\circ \rightarrow y_t = -y_{t,SM}$ ).

An analysis combining  $tHq$  and  $tHW$  processes will be made in this thesis taking advantage of the sensitivity improvement.

928 **2.6 Experimantal status of the anomalous**  
 929 **Higg-fermion coupling.**

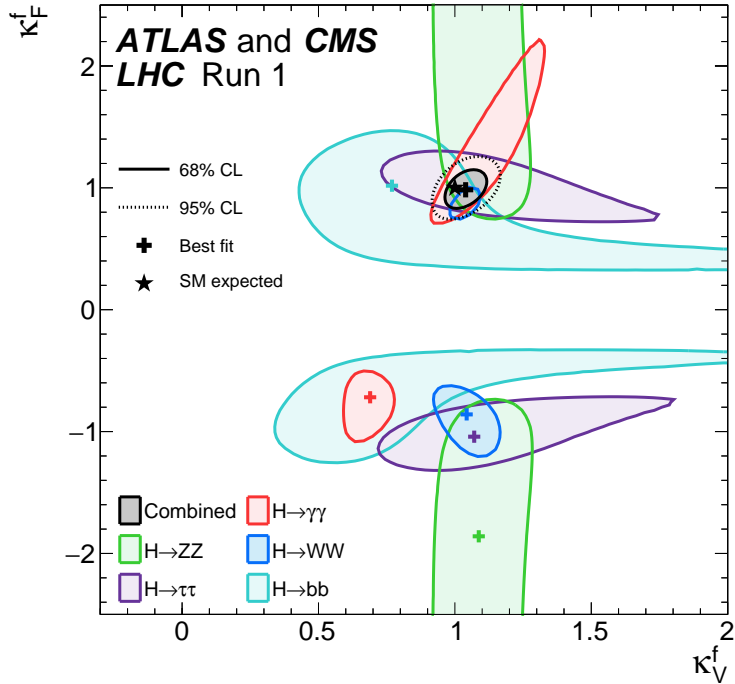


**Figure 2.18:** Combination of the ATLAS and CMS fits for coupling modifiers  $\kappa_t$ - $\kappa_V$ ; also shown the individual decay channels combination and their global combination. No assumptions have been made on the sign of the coupling modifiers [53].

930 ATLAS and CMS have performed analysis of the anomalous H-f coupling by making  
 931 likelihood scans for the two coupling modifiers,  $\kappa_t$  and  $\kappa_V$ , under the assumption that  
 932  $\kappa_Z = \kappa_W = \kappa_V$  and  $\kappa_t = \kappa_\tau = \kappa_b = \kappa_f$ . Figure 2.18 shows the result of the combination  
 933 of ATLAS and CMS fits; also the individual decay channels combination and the  
 934 global combination results are shown.

935 While all the channels are compatible for positive values of the modifiers, for negative  
 936 values of  $\kappa_t$  there is no compatibility. The best fit for individual channels is compatible  
 937 with negative values of  $\kappa_t$  except for the  $H \rightarrow bb$  channel which is expected to be the

938 most sensitive channel; therefore, the best fit for the global fit yields  $\kappa_t \geq 0$ . Thus,  
939 the anomalous H-t coupling cannot be excluded completely.

## 940 Chapter 3

# 941 The CMS experiment at the LHC

### 942 3.1 Introduction

943 Located on the Swiss-French border, the European Council for Nuclear Research  
944 (CERN) is the largest scientific organization leading the particle physics research.  
945 About 13000 people in a broad range of fields including users, students, scientists,  
946 engineers, among others, contribute to the data taking and analysis, with the goal  
947 of unveiling the secrets of nature and revealing the fundamental structure of the  
948 universe. CERN is also the home of the Large Hadron Collider (LHC), the largest  
949 circular particle accelerator around the world, where protons (or heavy ions) traveling  
950 close to the speed of light, are made to collide. These collisions open a window  
951 to investigate how particles (and their constituents if they are composite) interact  
952 with each other, providing clues about the laws of nature. This chapter presents an  
953 overview of the LHC structure and operation. A detailed description of the CMS  
954 detector is offered, given that the data used in this thesis have been taken with this  
955 detector.

## 956 3.2 The LHC

957 With 27 km of circumference, the LHC is currently the largest and most powerful  
 958 circular accelerator in the world. It is installed in the same tunnel where the Large  
 959 Electron-Positron (LEP) collider was located, taking advantage of the existing infras-  
 960 tructure. The LHC is also the larger accelerator in the CERN's accelerator complex  
 961 and is assisted by several successive accelerating stages before the particles are in-  
 962 jected into the LHC ring where they reach their maximum energy (see figure 3.1).

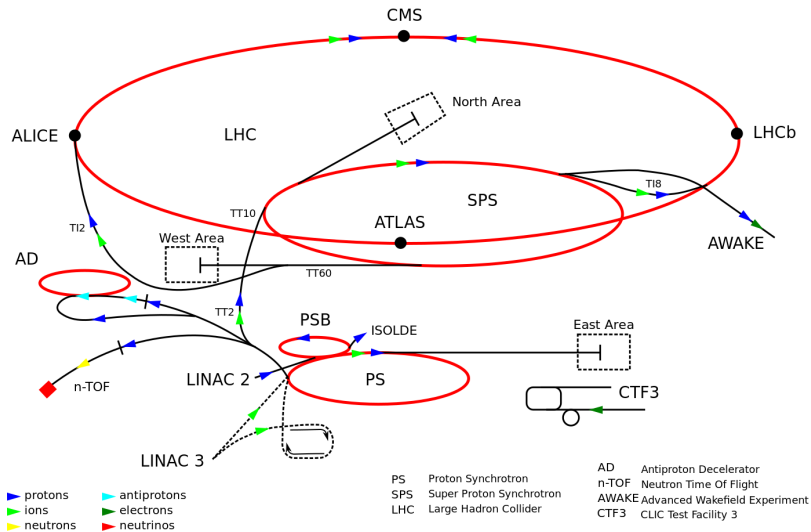


**Figure 3.1:** CERN accelerator complex. Blue arrows show the path followed by protons along the acceleration process [54].

963 LHC runs in three modes depending on the particles being accelerated

- 964     ● Proton-Proton collisions ( $pp$ ) for multiple physics experiments.
- 965     ● Lead-Lead collisions ( $Pb-Pb$ ) for heavy ion experiments.
- 966     ● Proton-Lead collisions ( $p-Pb$ ) for quark-gluon plasma experiments.

967 In this thesis only  $pp$  collisions will be considered.

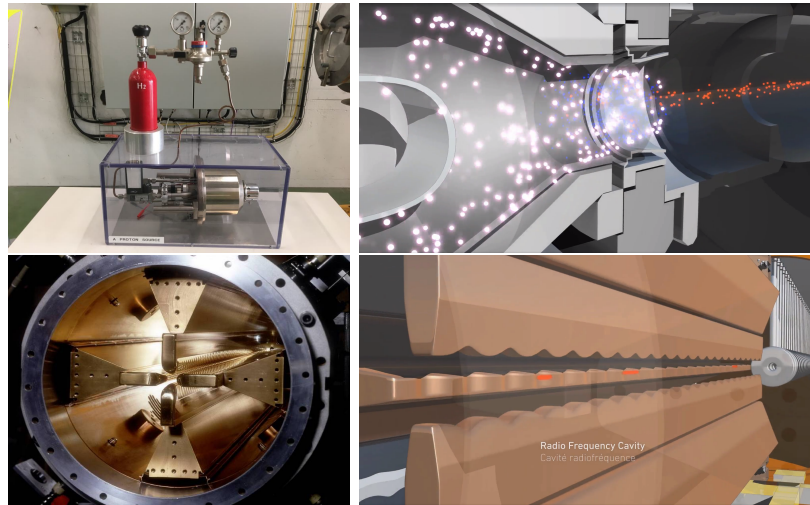


**Figure 3.2:** LHC protons source and the first acceleration stage. Top: the bottle contains hydrogen gas (white dots) which is injected into the metal cylinder to be broken down into electrons(blue dots) and protons(red dots); Bottom: the obtained protons are directed towards the radio frequency quadrupole which perform the first acceleration, focus the beam and create the bunches of protons. [58, 59]

969 Collection of protons starts with hydrogen atoms taken from a bottle, containing hy-  
 970 drogen gas, and injecting them in a metal cylinder; hydrogen atoms are broken down  
 971 into electrons and protons by an intense electric field (see figure3.2 top). The result-  
 972 ing protons leave the metal cylinder towards a radio frequency quadrupole (RFQ)  
 973 that focus the beam, accelerates the protons and creates the packets of protons called  
 974 bunches. In the RFQ, an electric field is generated by a RF wave at a frequency that  
 975 matches the resonance frequency of the cavity where the electrodes are contained.  
 976 The beam of protons traveling on the RFQ axis experiences an alternating electric  
 977 field gradient that generates the focusing forces.

978

979 In order to accelerate the protons, a longitudinal time-varying electric field component  
 980 is added to the system; it is done by giving the electrodes a sinus-like profile as shown  
 981 in figure 3.2 bottom. By matching the speed and phase of the protons with the  
 982 longitudinal electric field the bunching is performed; protons synchronized with the

983 RFQ (synchronous proton) do not feel an accelerating force, but those protons in the  
 984 beam that have more (or less) energy than the synchronous proton (asynchronous  
 985 protons) will feel a decelerating (accelerating) force; therefore, asynchronous protons  
 986 will oscillate around the synchronous ones forming bunches of protons [56]. From the  
 987 RFQ protons emerge with energy 750 keV in bunches of about  $1.15 \times 10^{11}$  protons [57].

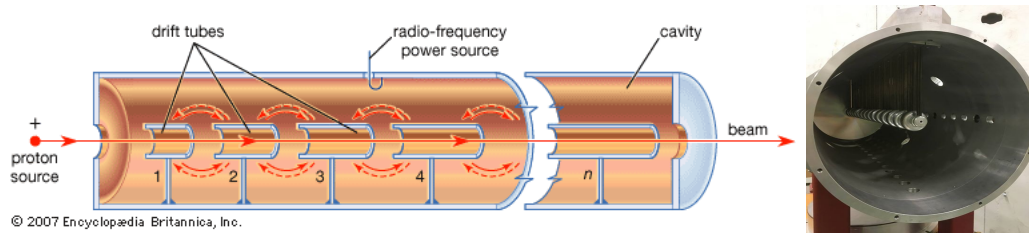


**Figure 3.3:** The LINAC2 accelerating system at CERN. Electric fields generated by radio frequency (RF) create acceleration and deceleration zones inside the cavity; deceleration zones are blocked by drift tubes where quadrupole magnets focus the proton beam. [60]

988 Proton bunches coming from the RFQ go to the linear accelerator 2 (LINAC2) where  
 989 they are accelerated to reach 50 MeV energy. In the LINAC2 stage, acceleration  
 990 is performed using electric fields generated by radio frequency which create zones  
 991 of acceleration and deceleration as shown in figure 3.3. In the deceleration zones,  
 992 the electric field is blocked using drift tubes where protons are free to drift while  
 993 quadrupole magnets focus the beam.

994

995 The beam coming from LINAC2 is injected into the proton synchrotron booster  
 996 (PSB) to reach 1.4 GeV in energy. The next acceleration is provided at the pro-  
 997 ton synchrotron (PS) up to 26 GeV, followed by the injection into the super proton  
 998 synchrotron (SPS) where protons are accelerated to 450 GeV. Finally, protons are  
 999 injected into the LHC where they are accelerated to the target energy of 6.5 TeV.  
 1000 PSB, PS, SPS and LHC accelerate protons using the same RF acceleration technique  
 1001 described before.

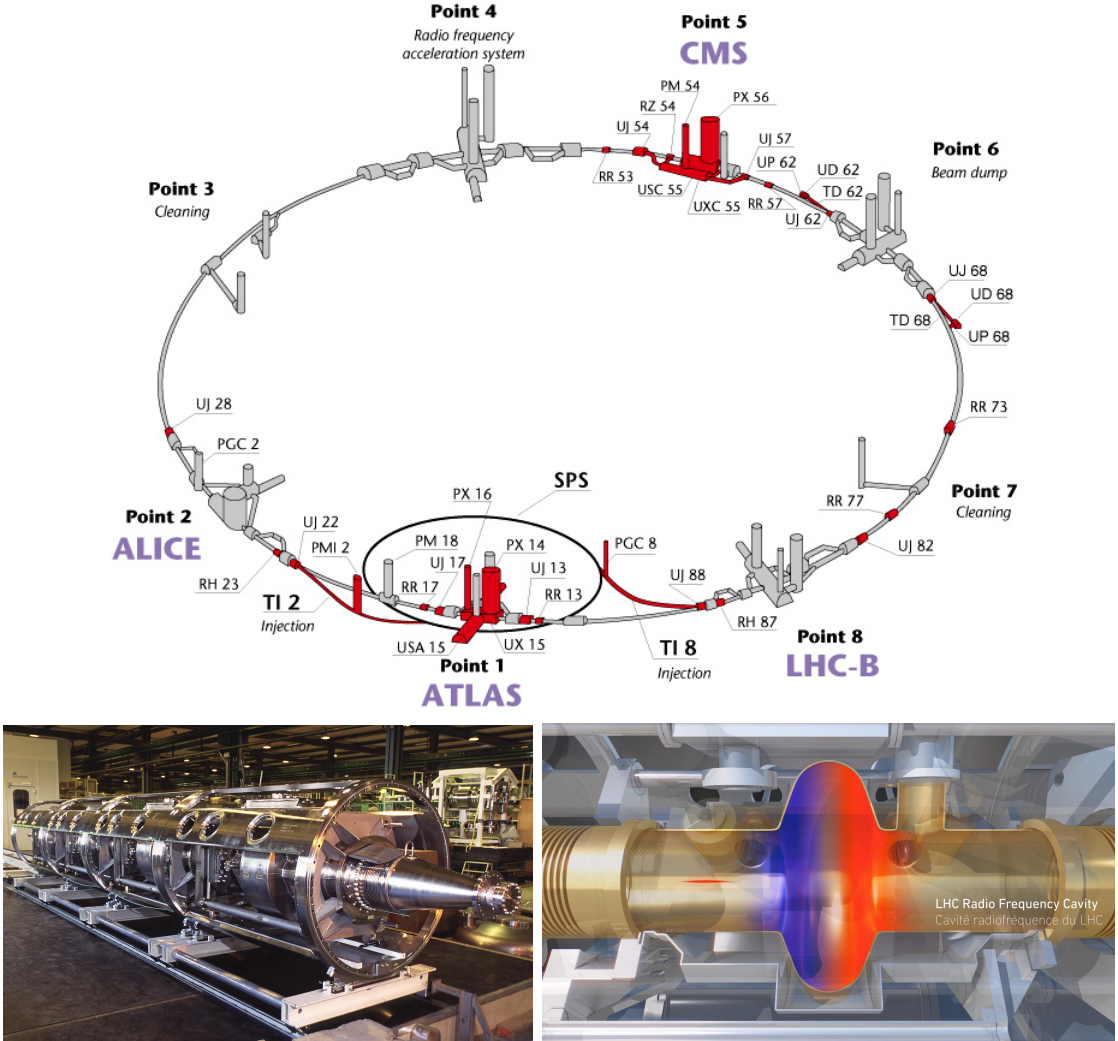


**Figure 3.4:** Top: LHC layout. The red zones indicate the infrastructure additions to the LEP installations, built to accommodate the ATLAS and CMS experiments which exceed the size of the former experiments located there [55]. Bottom: LHC RF cavities. A module accommodates 4 cavities that accelerate protons and preserve the bunch structure of the beam. [59, 61]

1002 LHC has a system of 16 RF cavities located in the so-called point 4, as shown in  
 1003 figure 3.4 top, tuned at a frequency of 400 MHz and the protons are carefully timed,  
 1004 so in addition to the acceleration effect the bunch structure of the beam is preserved.  
 1005 Bottom side of figure 3.4 shows a picture of a RF module composed of 4 RF cavities  
 1006 working in a superconducting state at 4.5 K; also is showed a representation of the

1007 accelerating electric field that accelerates the protons in the bunch.

1008

1009 While protons are accelerated in one section of the LHC ring, where the RF cavities  
 1010 are located, in the rest of their path they have to be kept in the curved trajectory  
 1011 defined by the LHC ring. Technically, LHC is not a perfect circle; RF, injection, beam  
 1012 dumping, beam cleaning and sections before and after the experimental points where  
 1013 protons collide are all straight sections. In total, there are 8 arcs 2.45 Km long each  
 1014 and 8 straight sections 545 m long each. In order to curve the proton's trajectory in  
 1015 the arc sections, superconducting dipole magnets are used.

1016

1017 Inside the LHC ring, there are two proton beams traveling in opposite directions in  
 1018 two separated beam pipes; the beam pipes are kept at ultra-high vacuum ( $\sim 10^{-9}$   
 1019 Pa) to ensure that there are no particles that interact with the proton beams. The  
 1020 superconducting dipole magnets used in LHC are made of a NbTi alloy, capable of  
 1021 transporting currents of about 12000 A when cooled at a temperature below 2K using  
 1022 liquid helium (see figure 3.5).

1023

1024 Protons in the arc sections of LHC feel a centripetal force exerted by the dipole  
 1025 magnets which is perpendicular to the beam trajectory; The magnitude of magnetic  
 1026 field needed can be found assuming that protons travel at  $v \approx c$ , using the standard  
 1027 values for proton mass and charge and the LHC radius, as

$$F_m = \frac{mv^2}{r} = qBv \quad \rightarrow B = 8.33T \quad (3.1)$$

1028 which is about 100000 times the Earth's magnetic field. A representation of the mag-  
 1029 netic field generated by the dipole magnets is shown on the bottom left side of figure

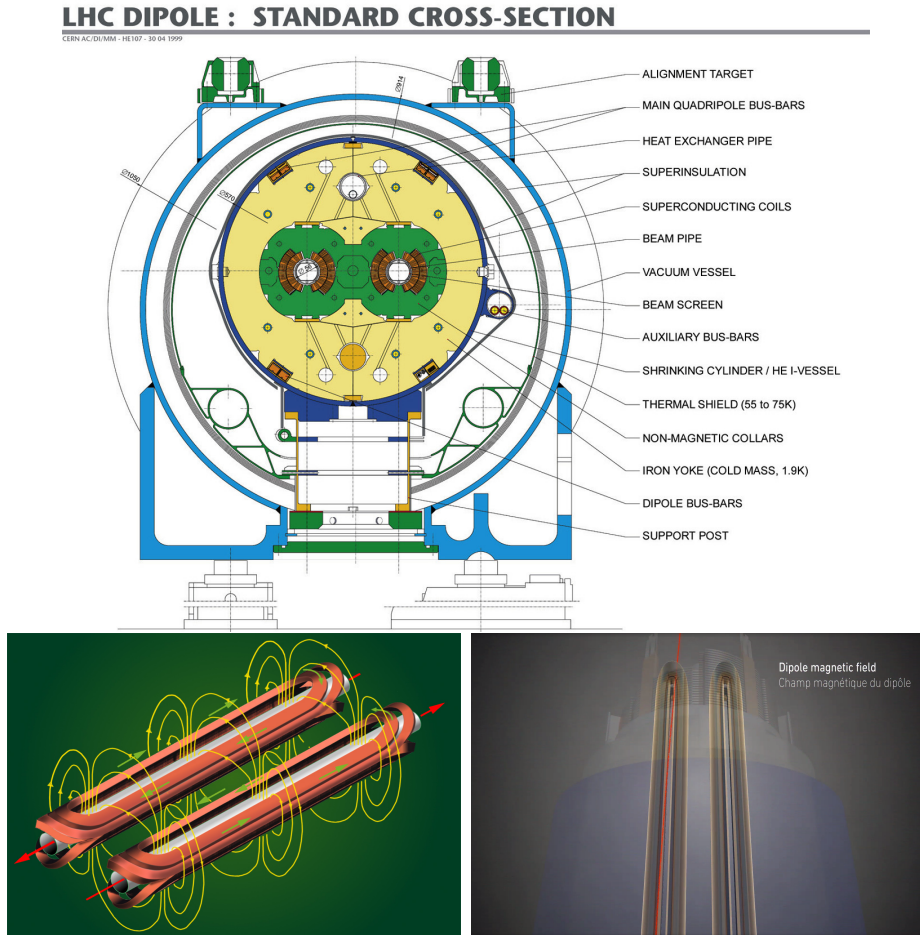


**Figure 3.5:** Top: LHC dipole magnet transverse view; cooling, shielding and mechanical support are indicated. Bottom left: Magnetic field generated by the dipole magnets; note that the direction of the field inside one beam pipe is opposite with respect to the other beam pipe which guarantee that both proton beams are curved in the same direction towards the center of the ring. The effect of the dipole magnetic field on the proton beam is represented on the bottom right side [59, 62, 63].

1030 3.5. The bending effect of the magnetic field on the proton beam is shown on the  
 1031 bottom right side of figure 3.5. Note that the dipole magnets are not curved; the arc  
 1032 section of the LHC ring is composed of straight dipole magnets of about 15 m. In  
 1033 total there are 1232 dipole magnets along the LHC ring.

1034

1035 In addition to bending the beam trajectory, the beam has to be focused so it stays

1036 inside the beam pipe. The focusing is performed by quadrupole magnets installed in  
 1037 a different straight section; in total 858 quadrupole magnets are installed along the  
 1038 LHC ring. Other effects like electromagnetic interaction among bunches, interaction  
 1039 with electron clouds from the beam pipe, the gravitational force on the protons, dif-  
 1040 ferences in energy among protons in the same bunch, among others, are corrected  
 1041 using sextupole and other magnetic multipoles.

1042

1043 The two proton beams inside the LHC ring are made of bunches with a cylindrical  
 1044 shape of about 7.5 cm long and about 1 mm in diameter; when bunches are close  
 1045 to the collision point (CP), the beam is focused up to a diameter of about 16  $\mu\text{m}$  in  
 1046 order to maximize the number of collisions per unit area and per second, known as  
 1047 luminosity ( $L$ ). Luminosity can be calculated using

$$L = fn \frac{N_1 N_2}{4\pi\sigma_x\sigma_y} \quad (3.2)$$

1048 where  $f$  is the revolution frequency,  $n$  is the number of bunches per beam,  $N_1$  and  
 1049  $N_2$  are the numbers of protons per bunch ( $1.5 \times 10^{11}$ ),  $\sigma_x$  and  $\sigma_y$  are the gaussian  
 1050 transverse sizes of the bunches. The expected luminosity is about

$$f = \frac{v}{2\pi r_{LHC}} \approx \frac{3 \times 10^8 \text{ m/s}}{27 \text{ km}} \approx 11.1 \text{ kHz},$$

$$n = 2808$$

$$N_1 = N_2 = 1.5 \times 10^{11}$$

$$\sigma_x = \sigma_y = 16 \mu\text{m}$$

1051

$$L = 1.28 \times 10^{34} \text{ cm}^{-2} \text{ s}^{-1} = 1.28 \times 10^{-5} \text{ fb}^{-1} \text{ s}^{-1} \quad (3.3)$$

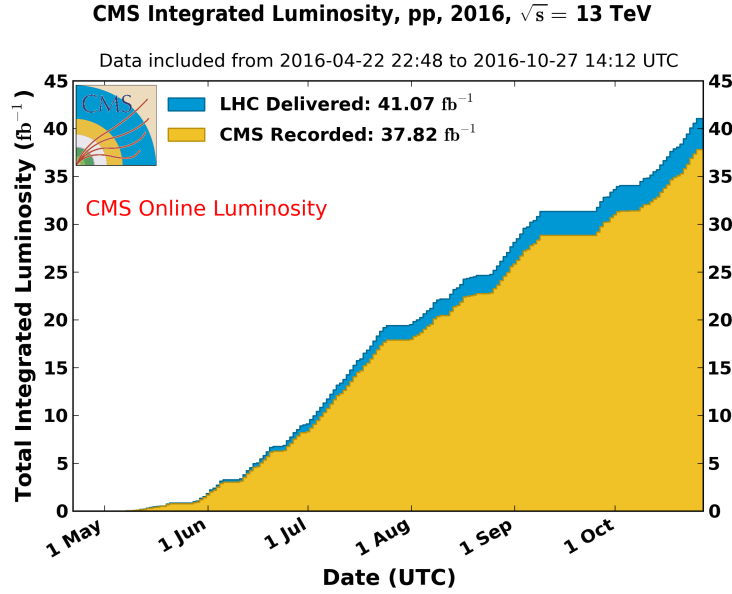


**Figure 3.6:** Integrated luminosity delivered by LHC and recorded by CMS during 2016. The difference between the delivered and the recorded luminosity is due to fails and issues occurred during the data taking in the CMS experiment [64].

1052 Luminosity is a fundamental aspect of LHC given that the bigger luminosity the  
 1053 bigger number of collisions, which means that for processes with a very small cross  
 1054 section the number of expected occurrences is increased and so the chances of being  
 1055 detected. The integrated luminosity, i.e., the total luminosity, collected by the CMS  
 1056 experiment during 2016 is shown in figure 3.6; the data analyzed in this thesis corre-  
 1057 sponds to an integrated luminosity of  $35.9 \text{ fb}^{-1}$  at a center of mass-energy  $\sqrt{s} = 13$   
 1058 TeV.

1059

1060 A way to increase  $L$  is increasing the number of bunches in the beam. Currently, the  
 1061 separation between two consecutive bunches in the beam is 7.5 m which corresponds  
 1062 to a time separation of 25 ns. In the full LHC ring the allowed number of bunches is  
 1063  $n = 27\text{km}/7.5\text{m} = 3600$ ; however, there are some gaps in the bunch pattern intended  
 1064 for preparing the dumping and injection of the beam, thus, the proton beams are

1065 composed of 2808 bunches.

1066

1067 Once the proton beams reach the desired energy, they are brought to cross each other  
 1068 producing proton-proton collisions. The bunch crossing happens in precise places  
 1069 where the four LHC experiments are located, as seen in the top of figure 3.7. In 2008,  
 1070 the first set of collisions involved protons with  $\sqrt{s} = 7$  TeV; the energy was increased  
 1071 to 8 TeV in 2012 and to 13 TeV in 2015.

1072

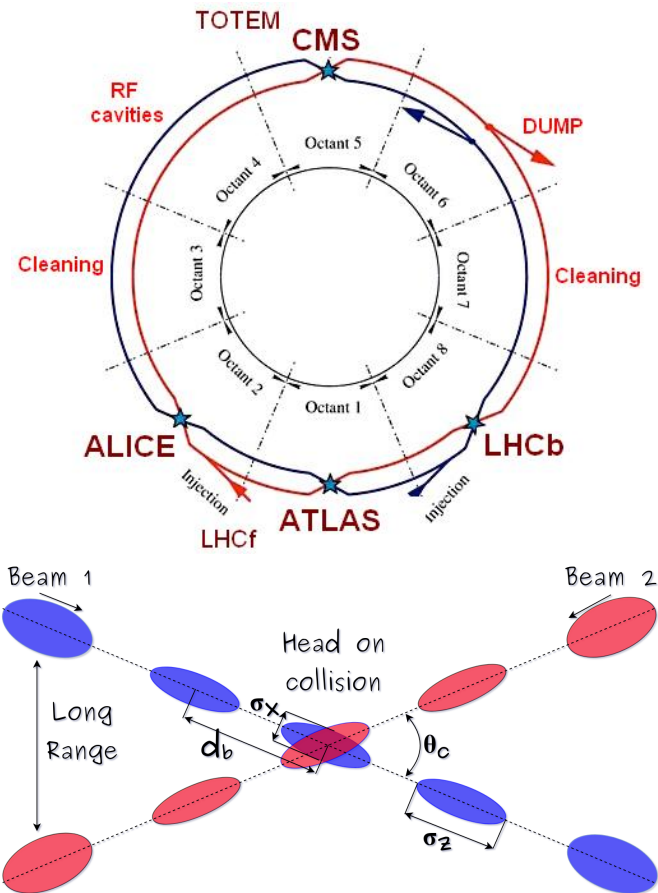


**Figure 3.7:** Top: LHC interaction points. Bunch crossing occurs where the LHC experiments are located [65]. Sections indicated as cleaning are dedicated to collimate the beam in order to protect the LHC ring from collisions with protons in very spreaded bunches. Bottom: bunch crossing scheme. Since the bunch crossing is not perfectly head-on, the luminosity is reduced in a factor of 17%; adapted from reference [77].

1073 CMS and ATLAS experiments, which are multi-purpose experiments, are enabled  
 1074 to explore physics in any of the collision modes. LHCb experiment is optimized  
 1075 to explore bottom quark physics, while ALICE is optimized for heavy ion collisions  
 1076 searches; TOTEM and LHCf are dedicated to forward physics studies; MoEDAL (not  
 1077 indicated in the figure) is intended for monopoles or massive pseudo stable particles  
 1078 searches.

1079

1080 At the CP there are two interesting details that need to be addressed. The first one  
 1081 is that the bunch crossing does not occur head-on but at a small crossing angle “ $\theta_c$ ”  
 1082 (280  $\mu$ rad in CMS and ATLAS) as shown in the bottom side of figure 3.7, affecting  
 1083 the overlapping between bunches; the consequence is a reduction of about 17% in  
 1084 the luminosity (represented by a factor not included in eqn: 3.2). The second one  
 1085 is the occurrence of multiple  $pp$  collisions in the same bunch crossing; this effect is  
 1086 called pile-up (PU). A fairly simple estimation of the PU follows from estimating the  
 1087 probability of collision between two protons, one from each of the bunches in course  
 1088 of collision; it depends roughly on the ratio of proton size and the cross section of the  
 1089 bunch in the interaction point, i.e.,

$$P(pp\text{-}collision) \sim \frac{d_{proton}^2}{\sigma_x \sigma_y} = \frac{(1\text{fm})^2}{(16\mu\text{m})^2} \sim 4 \times 10^{-21} \quad (3.4)$$

1090 however, there are  $N = 1.15 \times 10^{11}$  protons in a bunch, thus the estimated number of  
 1091 collisions in a bunch crossing is

$$PU = N^2 * P(pp\text{-}collision) \sim 50 \text{ } pp\text{-}collision \text{ per bunch crossing}, \quad (3.5)$$

1092 about 20 of those  $pp$  collisions are inelastic. Each collision generates a vertex, but  
 1093 only the most energetic is considered as a primary vertex; the rest are considered as

1094 PU vertices. A multiple  $pp$  collision event in a bunch crossing at CMS is showed in  
 1095 figure3.8. Unstable particles outgoing from the primary vertex will eventually decay;  
 1096 this decay vertex is known as a secondary vertex.

1097

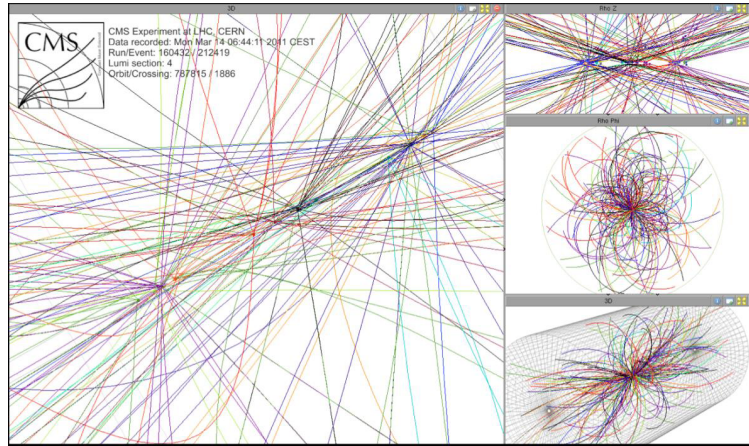


**Figure 3.8:** Multiple  $pp$  collision bunch crossing at CMS. Only the most energetic vertex is considered and the rest are catalogued as PU vertices [66].

1098 Next section presents a description of the CMS detector which it is the detector used  
 1099 to collect the data used in this thesis.

### 1100 3.3 The CMS experiment

1101 CMS is a general-purpose detector designed to conduct research in a wide range  
 1102 of physics from the standard model to new physics like extra dimensions and dark  
 1103 matter. Located at the point 5 in the LHC layout as shown in figure 3.4, CMS is  
 1104 composed of several detection systems distributed in a cylindrical structure; in total,  
 1105 CMS weights about 12500 tons in a very compact 21.6 m long and 14.6 m diameter  
 1106 cylinder. It was built in 15 separate sections at the ground level and lowered to the  
 1107 cavern individually to be assembled. A complete and detailed description of the CMS

1108 detector and its components is given in reference [67] on which this section is based on.

1109

1110 Figure 3.9 shows the layout of the CMS detector. The design is driven by the require-  
 1111 ments on the identification, momentum resolution and unambiguous charge determi-  
 1112 nation of the muons; therefore, a large bending power is provided by the solenoid  
 1113 magnet made of superconducting cable capable to generate a 3.8 T magnetic field.  
 1114 The detection system is composed of (from the innermost to the outermost)

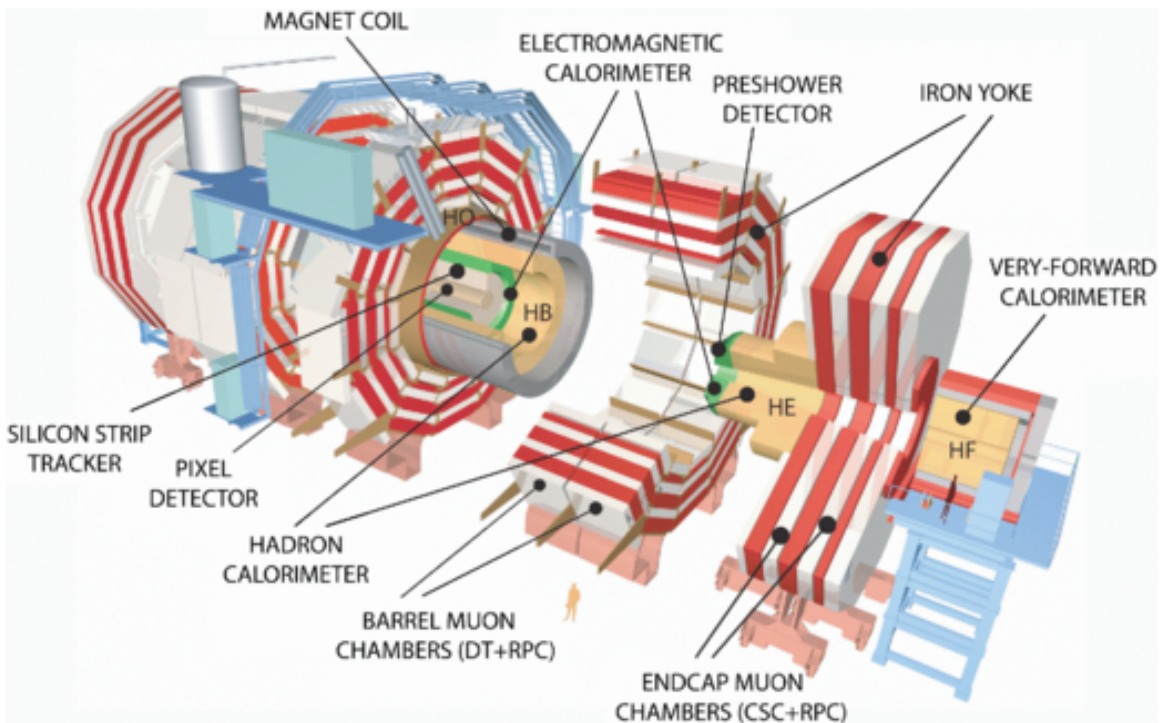


**Figure 3.9:** Layout of the CMS detector. The several subdetectors are indicated. The central region of the detector is referred as the Barrel section while the endcaps are referred as the forward sections. [68].

1115 • Pixel detector.

1116 • Silicon strip tracker.

1117 • Preshower detector.

1118 • Electromagnetic calorimeter.

1119 • Hadronic calorimeter.

1120 • Muon chambers (Barrel and endcap)

1121 The central region of the detector is commonly referred as the barrel section while the  
 1122 endcaps are referred as the forward sections of the detector; thus, each subdetector  
 1123 is composed of a barrel section and a forward section.

### 1124 3.3.1 Coordinate system

1125 The coordinate system used by CMS is centered in the geometrical center of the  
 1126 detector which is the same as the CP as shown in figure3.10. The  $z$ -axis is parallel  
 1127 to the beam direction, while the  $Y$ -axis pointing vertically upward, and the  $X$ -axis  
 1128 pointing radially inward toward the center of the LHC.

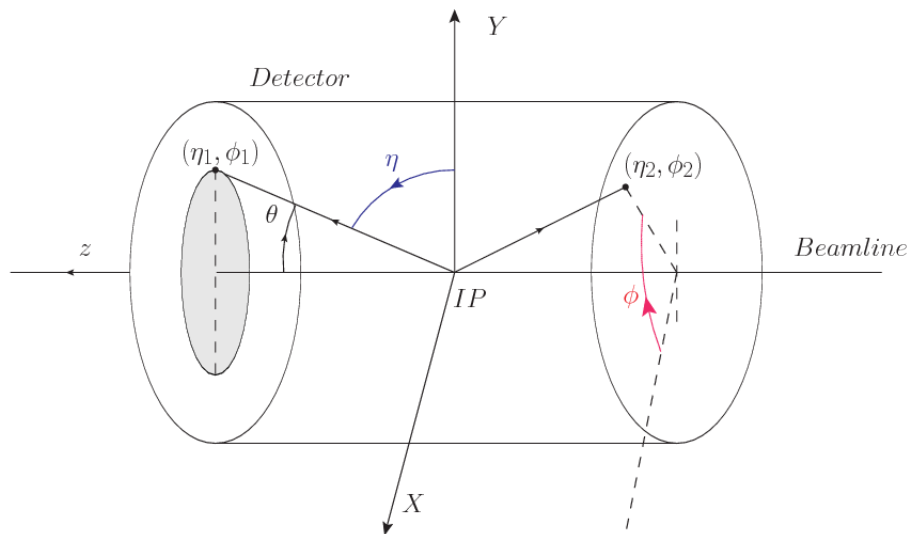


**Figure 3.10:** CMS detector coordinate system.

1129 In addition to the common cartesian and cylindrical coordinate systems, two coordi-  
 1130 nates are of particular utility in particle physics: rapidity( $y$ ) and pseudorapidity( $\eta$ ),

1131 defined in connection to the polar angle  $\theta$ , energy and longitudinal momentum com-  
 1132 ponent (momentum along the  $z$ -axis) according to

$$y = \frac{1}{2} \ln \frac{E + p_z}{E - p_z} \quad \eta = -\ln \left( \tan \frac{\theta}{2} \right) \quad (3.6)$$

1133 Rapidity is related to the angle between the  $XY$ -plane and the direction in which the  
 1134 products of a collision are emitted; it has the nice property that the difference between  
 1135 the rapidities of two particles is invariant with respect to Lorentz boosts along the  $z$ -  
 1136 axis. Thus, data analysis becomes more simple when based on rapidity; however, it is  
 1137 not simple to measure the rapidity of highly relativistic particles, as those produced  
 1138 after  $pp$  collisions. Under the highly relativistic motion approximation,  $y$  can be  
 1139 rewritten in terms of the polar angle, concluding that rapidity is approximately equal  
 1140 to the pseudorapidity defined above, i.e.,  $y \approx \eta$ . Note that  $\eta$  is easier to measure than  $y$   
 1141 given the direct relationship between the former and the polar angle. Angular distance  
 1142 between two objects in the detector ( $\Delta R$ ) is defined in terms of their coordinates  
 1143  $(\eta_1, \phi_1), (\eta_2, \phi_2)$  as

$$\Delta R = \sqrt{(\Delta\eta)^2 - (\Delta\phi)^2} \quad (3.7)$$

### 1144 3.3.2 Pixels detector

1145 The CMS tracking system is designed to provide a precise measurement of the tra-  
 1146 jectory (*track*) followed by the charged particles created after the  $pp$  collisions; also,  
 1147 the precise reconstruction of the primary and secondary origins (*vertices*) is expected  
 1148 in an environment where, each 25 ns, the bunch crossing produce about 20 inelastic  
 1149 collisions and about 1000 particles. An increment in the luminosity is ongoing which  
 1150 implies that the PU will increase accordingly.

1152 The pixel detector was replaced during the 2016-2017 extended year-end technical  
1153 stop, due to the increasingly challenging operating conditions like the higher particle  
1154 flow and more radiation harsh environment, among others. The new one is respond-  
1155 ing as expected, reinforcing its crucial role in the successful way to fulfill the new  
1156 LHC physics objectives after the discovery of the Higgs boson. The last chapter of  
1157 this thesis is dedicated to describe my contribution to the “Forward Pixel Phase 1  
1158 upgrade”.

1159

1160 The current pixel detector is composed of 1856 silicon pixel detector modules orga-  
1161 nized in four-barrel layers in the central region and three disks in the forward region;  
1162 it is designed to record efficiently and with high precision, up to  $10\mu\text{m}$  in the  $XY$ -  
1163 plane and  $20\mu\text{m}$  in the  $z$ -direction, the first four space-points (*hits*) near to the CP  
1164 region (see figure 3.11 left side) in the range  $|\eta| \leq 2.5$ . The first barrel layer is located  
1165 at a radius of 30 mm from the beamline, while the fourth layer is located at a radius  
1166 of 160 mm closer to the strip tracker inner barrel layer (see section 3.3.3) in order to  
1167 reduce the rate of fake tracks. The high granularity of the detector is represented in  
1168 its about 123 Mpixels, each of size  $100 \times 150\mu\text{m}^2$ , which is almost twice the channels  
1169 of the old detector. The transverse momentum resolution of tracks can be measured  
1170 with a resolution of 1-2% for muons of  $p_T = 100$  GeV.

1171

1172 Some of the improvements with respect to the previous pixel detector include a higher  
1173 average tracking efficiency and lower average fake rate as well as higher track impact  
1174 parameter resolution which is fundamental in order to increase the efficiency in the  
1175 identification of jets originating from b quarks (b-tagging). A significant source of  
1176 improvement comes from the overall reduction in the material budget of the detector  
1177 which results in fewer photon conversions and less multiple scattering from charged

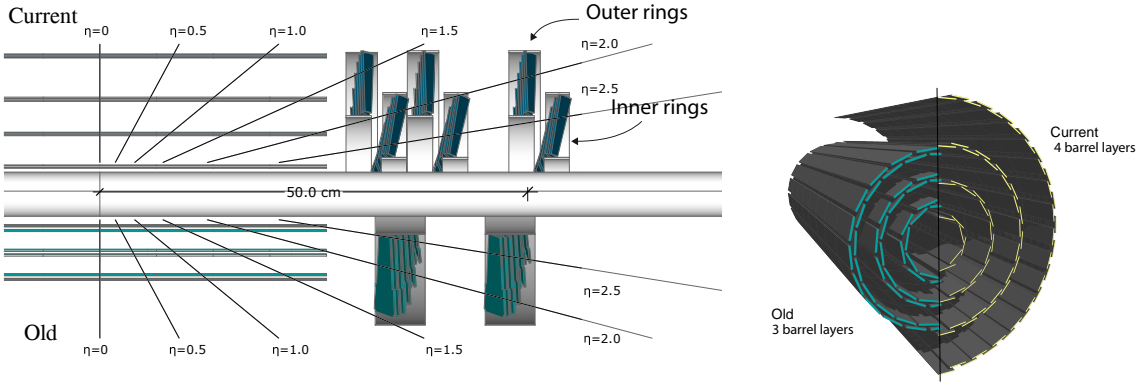


**Figure 3.11:** CMS pixel detector schematic view. Left: layout comparing the layers and disks in the old and current pixel detectors. Right: Transverse-oblique view comparing the pixel barrel layers in the two [70].

1178 particles.

### 1179 3.3.3 Silicon strip tracker

1180 The silicon strip tracker (SST) is the second stage in the CMS tracking system. The  
 1181 top side of figure 3.12 shows a schematic of the SST. The inner tracker region is com-  
 1182 posed of the tracker inner barrel (TIB) and the tracker inner disks (TID) covering the  
 1183 region  $r < 55$  cm and  $|z| < 118$  cm. The TIB is composed of 4 layers while the TID  
 1184 is composed of 3 disks at each end. The silicon sensors in the inner tracker are 320  
 1185  $\mu\text{m}$  thick, providing a resolution of about 13-38  $\mu\text{m}$  in the  $r\phi$  position measurement.

1186

1187 The modules indicated in blue in the schematic view of figure 3.12 are two modules  
 1188 mounted back-to-back and rotated in the plane of the module by a “stereo” angle of  
 1189 100 mrad; the hits from these two modules, known as “stereo hits”, are combined to  
 1190 provide a measurement of the second coordinate ( $z$  in the barrel and  $r$  on the disks)  
 1191 allowing the reconstruction of hit positions in 3-D.

1192

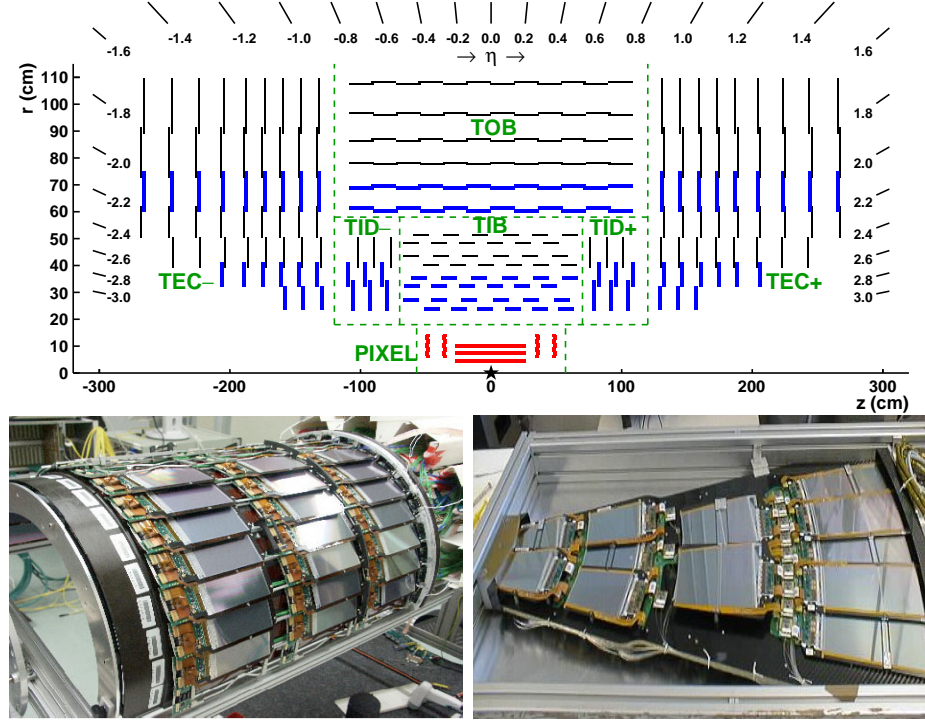


**Figure 3.12:** Top: CMS Silicon Strip Tracker (SST) schematic view. The SST is composed of the tracker inner barrel (TIB), the tracker inner disks (TID), the tracker outer barrel (TOB) and the tracker endcaps (TEC). Each part is made of silicon strip modules; the modules in blue represent two modules mounted back-to-back and rotated in the plane of the module by a stereo angle of 120 mrad in order to provide a 3-D reconstruction of the hit positions. Bottom: pictures of the TIB (left) and TEC (right) modules [71–73].

1193 The outer tracker region is composed of the tracker outer barrel (TOB) and the  
 1194 tracker endcaps (TEC). The six layers of the TOB offer coverage in the region  $r > 55$   
 1195 cm and  $|z| < 118$  cm, while the 9 disks of the TEC cover the region  $124 < |z| < 282$   
 1196 cm. The resolution offered by the outer tracker is about  $13\text{--}38 \mu\text{m}$  in the  $r\phi$  position  
 1197 measurement. The inner four TEC disks use silicon sensors  $320 \mu\text{m}$  thick; those in  
 1198 the TOB and the outer three TEC disks use silicon sensors of  $500 \mu\text{m}$  thickness. The  
 1199 silicon strips run parallel to the  $z$ -axis and the distance between strips varies from 80  
 1200  $\mu\text{m}$  in the inner TIB layers to  $183 \mu\text{m}$  in the inner TOB layers; in the endcaps the  
 1201 wedge-shaped sensors with radial strips, whose pitch range between  $81 \mu\text{m}$  at small  
 1202 radii and  $205 \mu\text{m}$  at large radii.

1203

1204 The whole SST has 15148 silicon modules, 9.3 million silicon strips and cover a total  
 1205 active area of about  $198 \text{ m}^2$ .

1206 **3.3.4 Electromagnetic calorimeter**

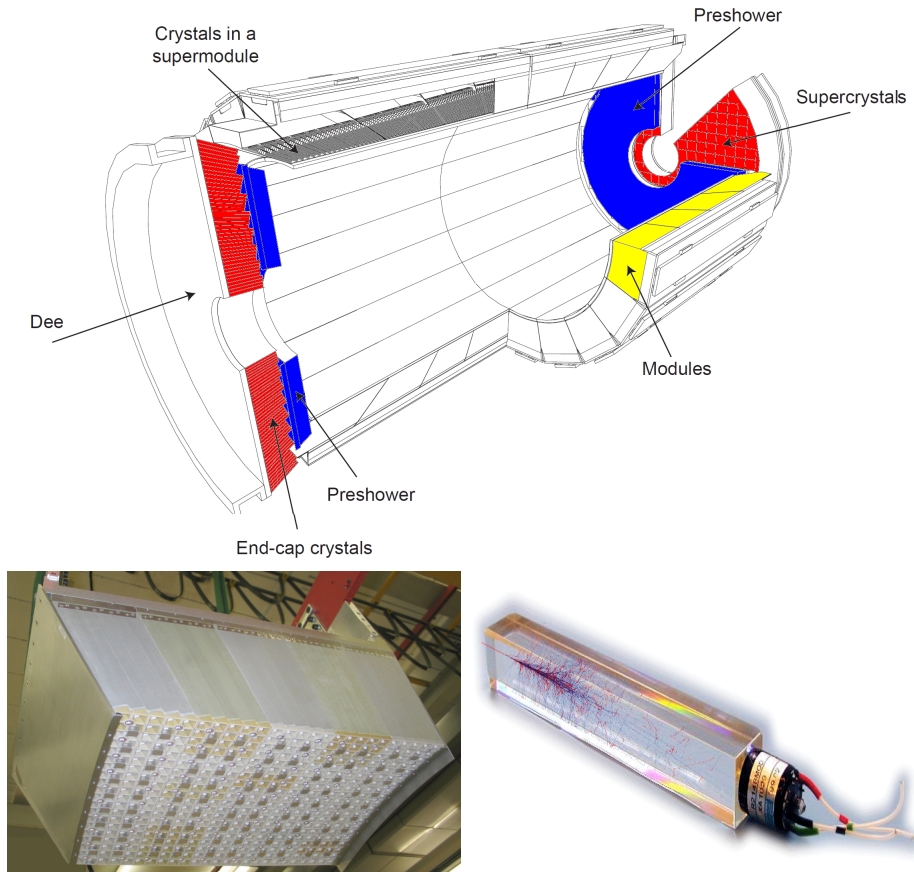


**Figure 3.13:** Top: CMS ECAL schematic view. Bottom: Module equipped with the crystals (left); ECAL crystal(right).

1207 The CMS electromagnetic calorimeter (ECAL) is designed to measure the energy of  
 1208 electrons and photons. It is composed of 75848 lead tungstate crystals which have a  
 1209 short radiation length (0.89 cm) and fast response, since 80% of the light is emitted  
 1210 within 25 ns; however, they are combined with Avalanche photodiodes (APDs) as

1211 photodetectors given that crystals themselves have a low light yield ( $30\gamma/\text{MeV}$ ). A  
 1212 schematic view of the ECAL is shown in figure 3.13.

1213

1214 Energy is measured when electrons and photons are absorbed by the crystals which  
 1215 generates an electromagnetic “shower”, as seen in bottom right picture of the fig-  
 1216 ure3.13; the shower is seen as a *cluster* of energy which depending on the amount  
 1217 of energy deposited can involve several crystals. The ECAL barrel (EB) covers the  
 1218 region  $|\eta| < 1.479$ , using crystals of depth of 23 cm and  $2.2 \times 2.2 \text{ cm}^2$  transverse  
 1219 section; the ECAL endcap (EE) covers the region  $1.479 < |\eta| < 3.0$  using crystals  
 1220 of depth 22 cm and transverse section of  $2.86 \times 2.86 \text{ cm}^2$ ; the photodetectors used  
 1221 are vacuum phototriodes (VPTs). Each EE is divided in two structures called “Dees”.

1222

1223 In front of the EE, it is installed the preshower detector (ES) which covers the region  
 1224  $1.653 < |\eta| < 2.6$ . The ES provides a precise measurement of the position of electro-  
 1225 magnetic showers, which allows to distinguish electrons and photons signals from  $\pi^0$   
 1226 decay signals. The ES is composed of a layer of lead absorber followed by a layer of  
 1227 plastic scintillators

### 1228 3.3.5 Hadronic calorimeter

1229 Hadrons are not absorbed by the ECAL but by the hadron calorimeter (HCAL),  
 1230 which is made of a combination of alternating brass absorber layers and silicon photo-  
 1231 multiplier(SiPM) layers; therefore, particles passing through the scintillator material  
 1232 produce showers, as in the ECAL, as a result of the inelastic scattering of the hadrons  
 1233 with the detector material. Since the particles are not absorbed in the scintillator,  
 1234 their energy is sampled; therefore the total energy is not measured but estimated from

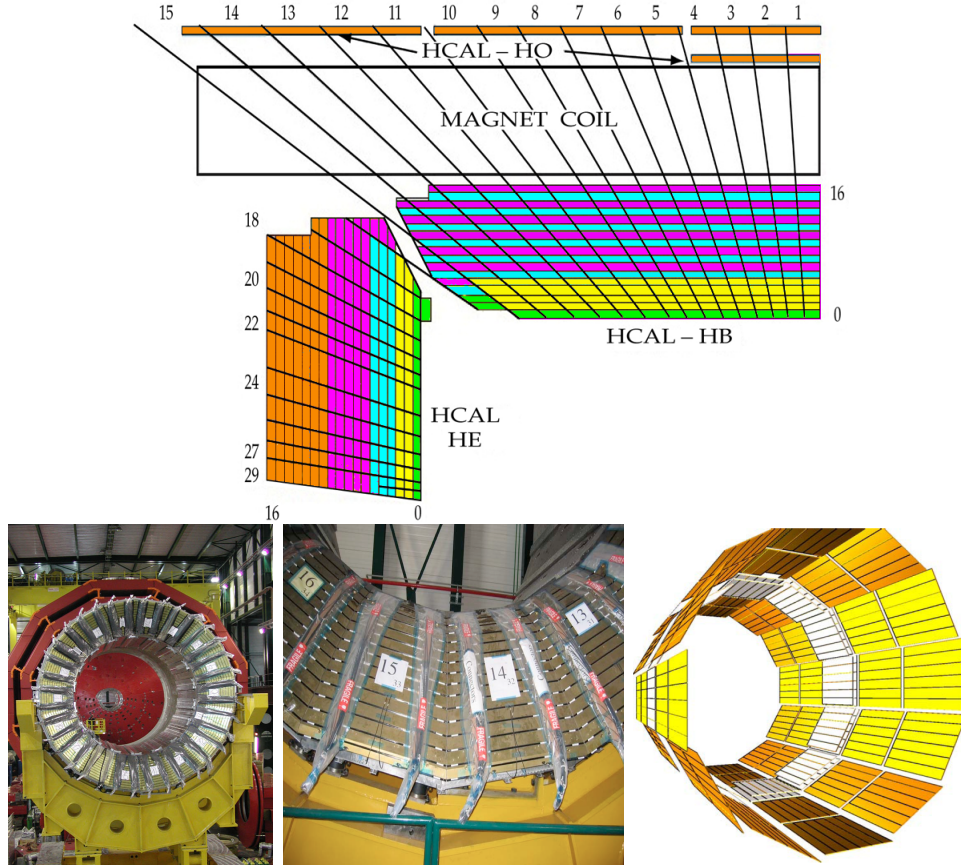


**Figure 3.14:** Top: CMS HCAL schematic view, the colors indicate the layers that are grouped into the same readout channels. Bottom: picture of a section of the HB; the absorber material is the golden region and scintillators are placed in between the absorber material (left and center). Schematic view of the HO (right). [74,75]

1235 the energy clusters, which reduce the resolution of the detector. Brass was chosen  
 1236 as the absorber material due to its short interaction length ( $\lambda_I = 16.42\text{cm}$ ) and its  
 1237 non-magnetivity. Figure 3.14 shows a schematic view of the CMS HCAL.

1238

1239 The HCAL is divided into four sections; the Hadron Barrel (HB), the Hadron Outer  
 1240 (HO), the Hadron Endcap (HE) and the Hadron Forward (HF) sections. The HB  
 1241 covers the region  $0 < |\eta| < 1.4$ , while the HE covers the region  $1.3 < |\eta| < 3.0$ . The HF,  
 1242 made of quartz fiber scintillator and steel as absorption material, covers the forward

region  $3.0 < |\eta| < 5.2$ . Both the HB and HF are located inside the solenoid. The HO is placed outside the magnet as an additional layer of scintillators with the purpose of measure the energy tails of particles passing through the HB and the magnet (see figure 3.14 top and bottom right). The upgrades made to the HCAL during the technical stop 2016-2017 consisted in the replacement of the photo transducer, in order to improve the efficiency.

### 3.3.6 Superconducting solenoid magnet

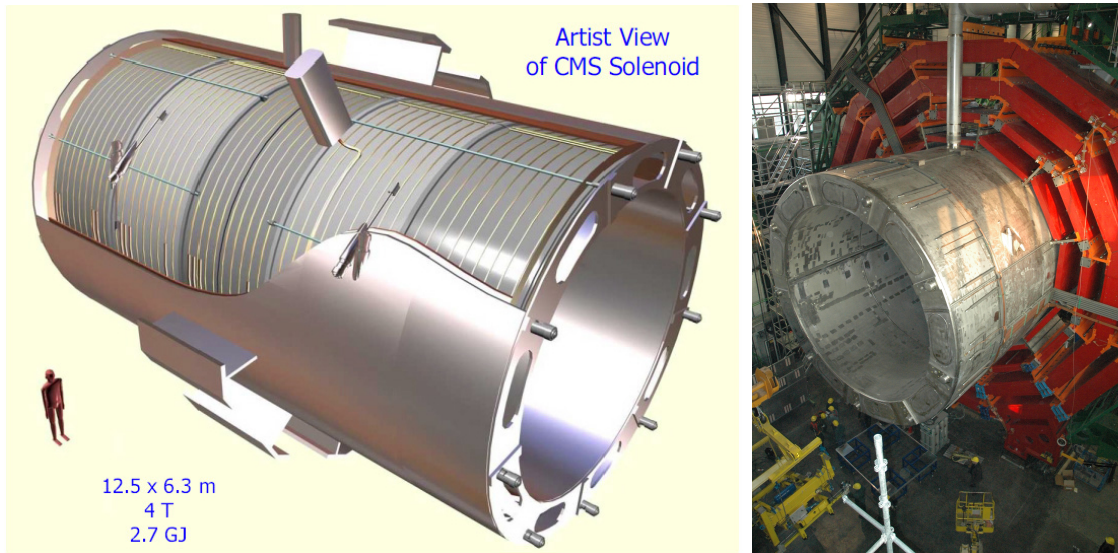


**Figure 3.15:** Artistic representation of the CMS solenoid magnet(left). The magnet is supported on an iron yoke (right) which also serves as the house of the muon detector and as mechanical support for the whole CMS detector [69].

The superconducting magnet installed in the CMS detector is designed to provide an intense and highly uniform magnetic field in the central part of the detector. In fact, the tracking system takes advantage of the bending power of the magnetic field to measure with precision the momentum of the particles that traverse it; the unambiguous determination of the sign for high momentum muons was a driven principle during the design of the magnet. The magnet has a diameter of 6.3 m, a length of 12.5

1256 m and a cold mass of 220 t; the generated magnetic field reaches a strength of 3.8T.  
 1257 Since it is made of Ni-Tb superconducting cable it has to operate at a temperature  
 1258 of 4.7 K by using a helium cryogenic system; the current circulating in the cables  
 1259 reaches 18800 A under normal running conditions. The left side of figure 3.15 shows  
 1260 an artistic view of the CMS magnet, while the right side shows a transverse view of  
 1261 the cold mass where the winding structure is visible.

1262

1263 The yoke (see figure 3.15), composed of 5 barrel wheels and 6 endcap disks made  
 1264 of iron, serves not only as the media for magnetic flux return but also provides the  
 1265 house for the muon detector system and structural stability to the full detector.

### 1266 3.3.7 Muon system

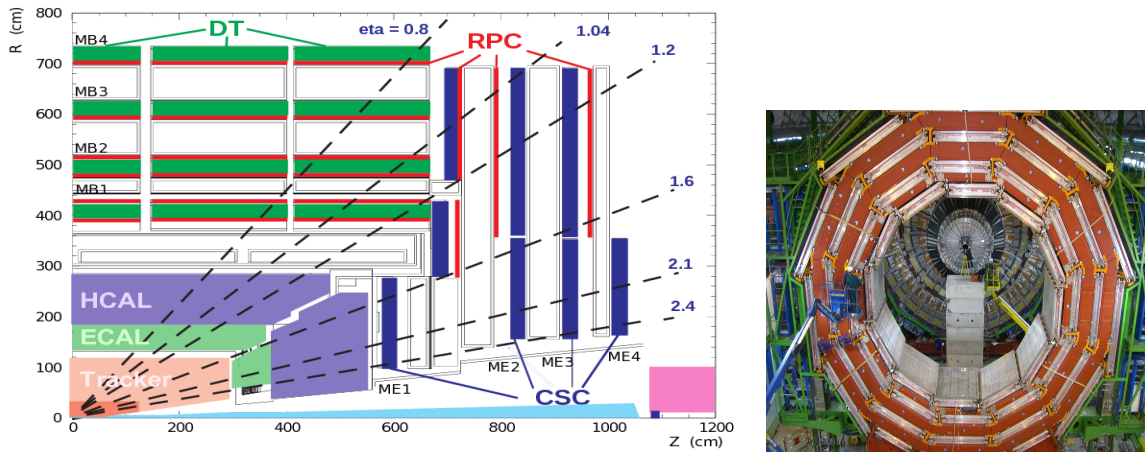


**Figure 3.16:** Left: CMS muon system schematic view; Right: one of the yoke rings with the muon DTs and RPCs installed; in the back it is possible to see the muon endcap [76].

1267 Muons are the only charged particles able to pass through all the CMS detector due  
 1268 to their low ionization energy loss; thus, muons can be separated easily from the  
 1269 high amount of particles produced in a  $pp$  collision. Also, muons are expected to be  
 1270 produced in the decay of several new particles; therefore, a good detection of muons

1271 was on the leading principles when designing the CMS detector.

1272

1273 The CMS muon detection system (muon spectrometer) is embedded in the return  
1274 yoke as seen in figure 3.16. It is composed of three different detector types, the drift  
1275 tube chambers (DT), Cathode strip chambers (CSC), and resistive plate chambers  
1276 (RPC); DT are located in the central region  $\eta < 1.2$  arranged in four layers of drift  
1277 chambers filled with an Ar/CO<sub>2</sub> gas mixture.

1278

1279 The muon endcaps are made of CSCs covering the region  $\eta < 2.4$  and filled with a  
1280 mixture of Ar/CO<sub>2</sub>/CF<sub>4</sub>. The reason behind using a different detector type lies on  
1281 the different conditions in the forward region like the higher muon rate and higher  
1282 residual magnetic field compared to the central region.

1283

1284 The third type of detector used in the muon system is a set of four disks of RPCs  
1285 working in avalanche mode. The RPCs provide good spatial and time resolutions.  
1286 The track of  $high - p_T$  muon candidates is built combining information from the  
1287 tracking system and the signal from up to six RPCs and four DT chambers.

1288 The muon tracks are reconstructed from the hits in the several layers of the muon  
1289 system.

### 1290 3.3.8 CMS trigger system

1291 Under normal conditions, CMS expects  $pp$  collisions every 25 ns, i.e., an interaction  
1292 rate of 40 MHz for which it is not possible to store the recorded data in full. In order  
1293 to handle this high event rate data, an online event selection, known as triggering, is  
1294 performed; triggering reduce the event rate to 100 Hz for storage and further offline

1295 analysis.

1296

1297 The trigger system starts with a reduction of the event rate to 100 kHz in the so-called  
 1298 “level 1 trigger (L1)”. L1 is based on dedicated programmable hardware like Field  
 1299 Programmable Gate Arrays (FPGAs) and Application Specific Integrated Circuits  
 1300 (ASICs), partly located in the detector itself; another portion is located in the CMS  
 1301 under-ground cavern. Hit patterns information from the muon chambers and the en-  
 1302 ergy deposits in the calorimeter are used to decide if an event is accepted or rejected,  
 1303 according to selection requirements previously defined, which reflect the interesting  
 1304 physics processes. Figure 3.17 shows the L1 trigger architecture.

1305

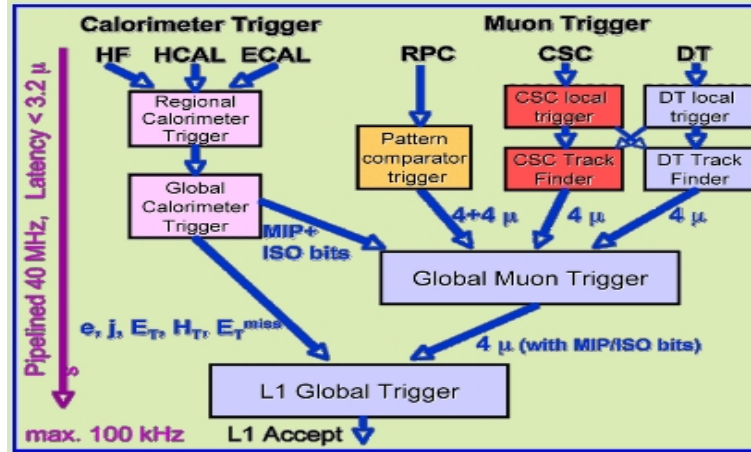


**Figure 3.17:** CMS Level-1 trigger architecture [77].

1306 The second stage in the trigger system is called “high-level trigger (HLT)”; events  
 1307 accepted by L1 are passed to HLT in order to make an initial reconstruction of them.  
 1308 HLT is software based and runs on a dedicated server farm, using selection algo-  
 1309 rithms and high-level object definitions; the event rate at HLT is reduced to 100 Hz.  
 1310 The first HLT stage takes information from the muon detectors and the calorimeters  
 1311 to make the initial object reconstruction; in the next HLT stage, information from

1312 the pixel and strip detectors is used to do first fast-tracking and then full tracking  
1313 online. This initial object reconstruction is used in further steps of the trigger system.

1314

1315 Events and preliminary reconstructed physics objects from HLT are sent to be fully  
1316 reconstructed at the CERN computing center. Again, the pixel detector information  
1317 provides high-quality seeds for the track reconstruction algorithm offline, primary ver-  
1318 tex reconstruction, electron and photon identification, muon reconstruction,  $\tau$  iden-  
1319 tification, and b-tagging. After full reconstruction, data sets are made available for  
1320 offline analyses.

1321

1322 During the 2016-2017 technical stop, the L1 system was updated in order to improve  
1323 the physics object identification by improving the algorithms and accounting for the  
1324 increasing pile-up scenario.

### 1325 **3.3.9 CMS computing**

1326 After the data, coming from the experiment, are processed at several levels, they have  
1327 to be stored and made available for further analysis; in order to cope all the tasks  
1328 implied in the offline data processing, like transfer, simulation, reconstruction and  
1329 reprocessing, among others, a big computing power is required. The CMS computing  
1330 system is based on the distributed architecture concept, where users of the system  
1331 and physical computer centers are distributed worldwide and interconnected by high-  
1332 speed networks.

1333 The worldwide LHC computing grid (WLCG) is the mechanism used to provide that  
1334 distributed environment. WLCG is a tiered structure connecting computing centers  
1335 around the world, which provides the necessary storage and computing facilities. The

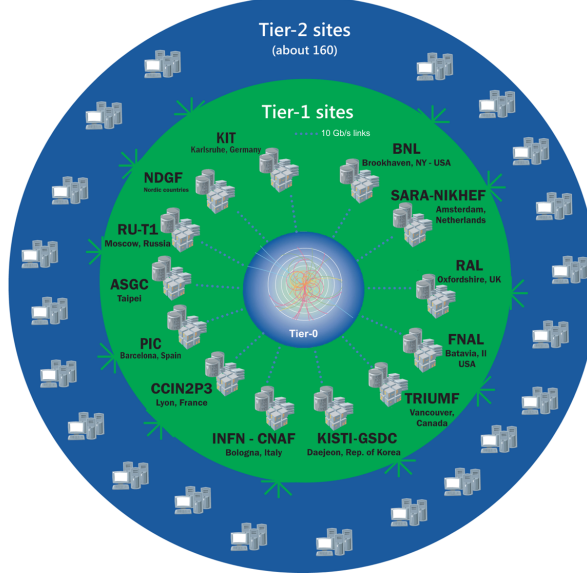


**Figure 3.18:** WLCG structure. The primary computer centers (Tier-0) are located at CERN (data center) and at the Wigner datacenter in Budapest. Tier-1 is composed of 13 centers and Tier-2 is composed of about 160 centers. [78].

1336 primary computing centers of the WLCG are located at the CERN and the Wigner  
 1337 datacenter in Budapest and are known as Tier-0 as shown in figure 3.18. The main  
 1338 responsibilities for each tier level are [78]

- 1339     • **Tier-0:** initial reconstruction of recorded events and storage of the resulting  
       1340 datasets, the distribution of raw data to the Tier-1 centers.
- 1341     • **Tier-1:** provide storage capacity, support for the Grid, safe-keeping of a pro-  
       1342 portional share of raw and reconstructed data, large-scale reprocessing and safe-  
       1343 keeping of corresponding output, generation of simulated events, distribution  
       1344 of data to Tier 2s, safe-keeping of a share of simulated data produced at these  
       1345 Tier 2s.
- 1346     • **Tier-2:** store sufficient data and provide adequate computing power for specific  
       1347 analysis tasks, provide analysis requirements and proportional share of simu-  
       1348 lated event production and reconstruction.

1349 Aside from the general computing strategy to manage the huge amount of data pro-  
1350 duced by experiments, CMS uses a framework to perform a variety of processing,  
1351 selection and analysis tasks. The central concept of the CMS data model referred to  
1352 as “event data model” (EDM) is the “Event”; therefore, an event is the unit that con-  
1353 tains the information from a single bunch crossing as well as any data derived from  
1354 that information like the reconstructed objects, the details under which additional  
1355 data are derived.

1356

1357 Events are passed as the input to the “physics modules” that obtain information from  
1358 them and create new one; for instance, “event data producers” add new data into the  
1359 events, “analyzers” produce an information summary from an event set, “filters” per-  
1360 form selection and triggering.

1361

1362 CMS uses several event formats with different levels of detail and precision

1363 • **Raw format:** events in this format contain the full recorded information from  
1364 the detector as well as trigger decision and other metadata. An extended version  
1365 of raw data is used to store information from the CMS Monte Carlo simulation  
1366 tools. Raw data are stored permanently, occupying about 2MB/event

1367 • **RECO format:** events in this format correspond to raw data that have been  
1368 submitted to reconstruction algorithms like primary and secondary vertex re-  
1369 construction, particle ID, track-finding. RECO events contain physical objects  
1370 and all the information used to reconstruct them; average size is about 0.5  
1371 MB/event.

1372 • **AOD format:** Analysis Object Data (AOD) is the data format used in the  
1373 physics analyses given that it contains the parameters describing the high-level

1374        physics objects in addition to enough information to allow a kinematic refitting if  
 1375        needed. AOD events are filtered versions of the RECO events to which skimming  
 1376        or other kind processes have been applied. Requires about 100 kB/event.

1377        • **Non-event data** are data needed to interpret and reconstruct events. Some  
 1378        of the non-event data used by CMS contains information about the detector  
 1379        contraction and condition data like calibrations, alignment, and detector status.

1380        Figure 3.19 shows the data flow scheme between CMS detector and hardware tiers.

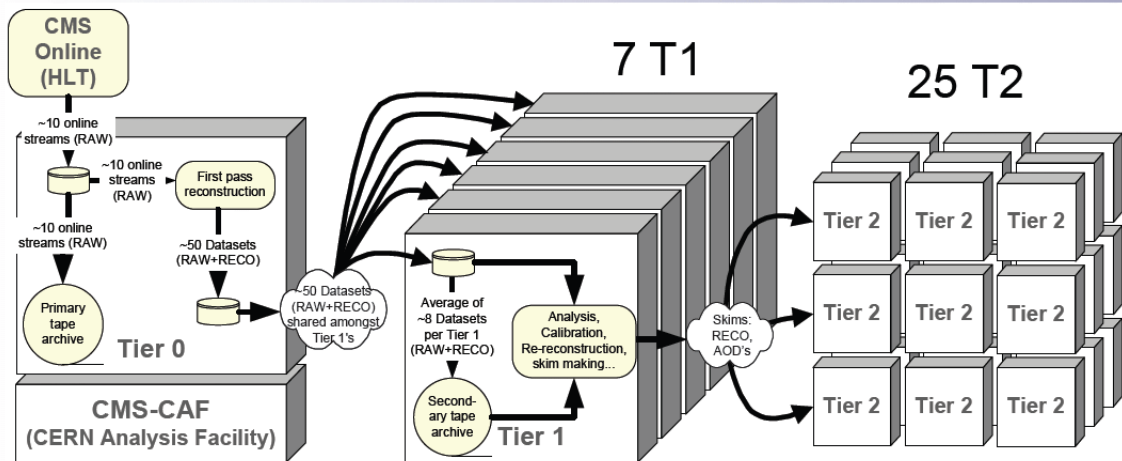


**Figure 3.19:** Data flow from CMS detector through hardware Tiers.

1381        The whole collection of software built as a framework is referred to as “CMSSW”. This  
 1382        framework provides the services needed by the simulation, calibration and alignment,  
 1383        and reconstruction modules that process event data, so that physicists can perform  
 1384        analysis. The CMSSW event processing model is composed of one executable, called  
 1385        cmsRun, and several plug-in modules which contains all the tools (calibration, recon-  
 1386        struction algorithms) needed to process an event. The same executable is used for  
 1387        both detector and Monte Carlo data [79].

1388 **Chapter 4**

1389 **Event generation, simulation and  
1390 reconstruction**

1391 The process of analyzing the data recorded by the CMS experiment involves several  
1392 stages where the data are processed in order to interpret the information provided by  
1393 all the detection systems; in those stages, the particles produced after the  $pp$  collision  
1394 are identified by reconstructing their trajectories and measuring their features. In  
1395 addition, the SM provides a set of predictions that have to be compared with the  
1396 experimental results; however, in most of the cases, theoretical predictions are not  
1397 directly comparable to experimental results due to the diverse source of uncertainties  
1398 introduced by the experimental setup and theoretical approximations among others.

1399

1400 The strategy to face these conditions consist in using statistical methods implemented  
1401 in computational algorithms to produce numerical results that can be contrasted with  
1402 the experimental results. These computational algorithms are commonly known as  
1403 Monte Carlo (MC) methods and, in the case of particle physics, they are designed to  
1404 apply the SM rules and produce predictions about the physical observables measured

in the experiments. Since particle physics is governed by quantum mechanics principles, predictions are not allowed for single events; therefore, a high number of events are “generated” and predictions are produced in the form of statistical distributions for the observables. Effects of the detector presence are included in the predictions by introducing simulations of the detector itself.

1410

1411 This chapter presents a description of the event generation strategy and the tools  
 1412 used to perform the detector simulation and physics objects reconstruction. A com-  
 1413 prehensive review of event generators for LHC physics can be found in reference [80]  
 1414 on which this chapter is based.

## 1415 4.1 Event generation

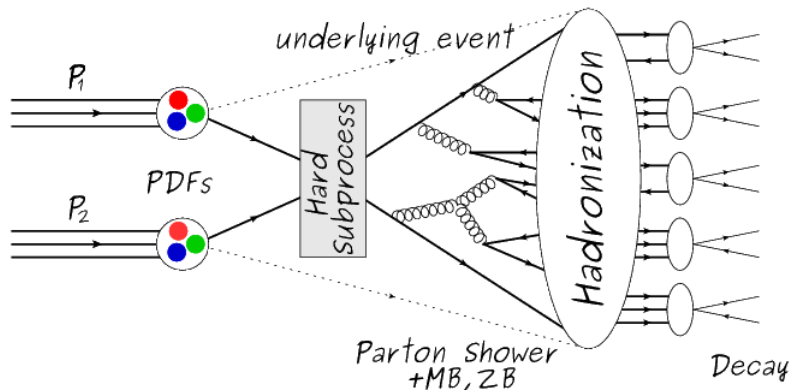


**Figure 4.1:** Event generation process. In the first step, the PDF of the colliding particles is considered so the specific interaction is described. The actual interaction is generated in the hard subprocess; the cross-section of the process is calculated from the matrix element connecting the initial and final states. The parton shower describes the evolution of the partons from the hard subprocess according to the DGLAP equations. At this step, the underlying event and PU effects are included in the generation. The resulting partons from the parton shower are recombined to form hadrons in the hadronization step; most of them are unstable, therefore, their decays are also generated in agreement to the known branching ratios. Modified from reference [81].

1416 The event generation is intended to create events that mimic the behavior of actual  
 1417 events produced in the collisions; they obey a sequence of steps from the particles colli-  
 1418 sion hard process to the decay process into the final state particles. Figure 4.1 shows  
 1419 a schematic view of the event generation process; the fact that the full process can  
 1420 be treated as several independent steps is based on the QCD factorization theorem.

1421

1422 Generation starts by taking into account the PDFs of the incoming particles. Event  
 1423 generators offer the option to choose from several PDF sets depending on the partic-  
 1424 ular process under simulation<sup>1</sup>; in the following  $pp$  collisions will be considered. The  
 1425 *hard subprocess* describes the actual interaction between partons from the incoming  
 1426 protons; it is represented by the matrix element connecting the initial and final states  
 1427 of the interaction. Normally, the matrix element can be written as a sum over Feyn-  
 1428 man diagrams and consider interferences between terms in the summation. During  
 1429 the generation of the hard subprocess, the production cross section is calculated.

1430

1431 The order to which the cross section is calculated depends on the order of the Feyn-  
 1432 man diagrams involved in the calculation; therefore, radiative corrections are included  
 1433 by considering a higher order Feynman diagrams where QCD radiation dominates.  
 1434 Currently, cross sections calculated to LO do not offer a satisfactory description of the  
 1435 processes, i.e., the results are only reliable for the shape of distributions; therefore,  
 1436 NLO calculations have to be performed with the implication that the computing time  
 1437 needed is highly increased.

1438

1439 The final parton content of the hard subprocess is subjected to the *parton shower*  
 1440 which generates the gluon radiation. Parton shower evolves the partons; i.e., gluons

---

<sup>1</sup> Tool in Reference [82] allows to plot different PDF sets under customizable conditions.

1441 split into quark-antiquark pairs and quarks of enough energy radiate gluons giving rise  
 1442 to further parton multiplication, following the DGLAP (Dokshitzer-Gribov-Lipatov-  
 1443 Altarelli-Parisi) equations. Showering continues until the energy scale is low enough  
 1444 to reach the non-perturbative limit.

1445

1446 In the simulation of LHC processes that involve  $b$  quarks like the single top quark or  
 1447 Higgs associated production, it is needed to consider that the  $b$  quark is heavier than  
 1448 the proton; in this sense, the QCD interaction description is made in two different  
 1449 schemes [83]

1450 • four-flavor (4F) scheme.  $b$  quarks appear only in the final state because they  
 1451 are heavier than the proton and therefore they can be produced only from the  
 1452 splitting of a gluon into pairs or singly in association with a  $t$  quark in high  
 1453 energy-scale interactions. During the simulation, the  $b$ -PDFs are set to zero  
 1454 because it cannot be part of the proton. Calculations in this scheme are more  
 1455 complicated due to the presence of the second  $b$  quark but the full kinematics is  
 1456 considered already at LO and therefore the accuracy of the description is better.

1457 • five-flavor (5F) scheme.  $b$  quarks are considered massless, therefore they can  
 1458 appear in both initial and final states since it can now be part of the proton; thus,  
 1459 during the simulation  $b$ -PDFs are not set to zero. In this scheme, calculations  
 1460 are simpler than in the 4F scheme and possible logarithmic divergences are  
 1461 absorbed by the PDFs through the DGLAP evolution.

1462 In this thesis, the  $tHq$  events are generated using the 4F scheme in order to reduce  
 1463 uncertainties, while the  $tHW$  events are generated using the 5F scheme to eliminate  
 1464 LO interference with the  $t\bar{t}H$  process [48].

1465

1466 Partons involved in the  $pp$  collision are the focus of the simulation, however, the rest  
 1467 of the partons inside the incoming protons are also affected because the remnants are  
 1468 colored objects; also, multiple parton interactions can occur. The hadronization of  
 1469 the remnants and multiple parton interactions are known as “underlying event” and  
 1470 it has to be included in the simulation. In addition, multiple  $pp$  collisions in the same  
 1471 bunch crossing (pile-up mentioned in 3.2) occurs, actually in two forms

- 1472 • *in-time PU* which refers to multiple  $pp$  collision in the bunch crossing but that  
 1473 are not considered as primary vertices.
- 1474 • *Out-of-time PU* which refers to overlapping  $pp$  collisions from consecutive bunch  
 1475 crossings; this can occurs due to the time-delays in the detection systems where  
 1476 information from one bunch crossing is assigned to the next or previous one.

1477 While the underlying event effects are included in generation using generator-specific  
 1478 tools, PU effects are added to the generation by overlaying Minimum-bias (MB) and  
 1479 Zero-bias (ZB) events to the generated events. MB events are inelastic events selected  
 1480 by using a loose (minimum bias) trigger with as little bias as possible, therefore ac-  
 1481 cepting a large fraction of the overall inelastic event; ZB events correspond to random  
 1482 events recorded by the detector when collisions are likely. MB model in-time PU and  
 1483 ZB model out-of-time PU.

1484

1485 The next step in the generation process is called “hadronization”. Since particles  
 1486 with a net color charge are not allowed to exits isolated, they have to recombine  
 1487 to form bound states. This is precisely the process by which the partons resulting  
 1488 from the parton shower arrange themselves as color singlets to form hadrons. At  
 1489 this step, the energy-scale is low and the strong coupling constant is large, there-  
 1490 fore hadronization process is non-perturbative and the evolution of the partons is

1491 described using phenomenological models. Most of the baryons and mesons produced  
 1492 in the hadronization are unstable and hence they will decay in the detector.

1493

1494 The last step in the generation process corresponds to the decay of the unstable  
 1495 particles generated during hadronization; it is also simulated in the hadronization  
 1496 step, based on the known branching ratios.

## 1497 4.2 Monte Carlo Event Generators.

1498 The event generation described in the previous section has been implemented in  
 1499 several software packages for which a brief description is given.

- 1500 • **PYTHIA 8.** It is a program designed to perform the generation of high en-  
 1501 ergy physics events which describe the collisions between particles such as elec-  
 1502 trons, protons. Several theories and models are implemented in it, in order to  
 1503 describe physical aspects like hard and soft interaction, parton distributions,  
 1504 initial and final-state parton showers, multiple parton interactions, beam rem-  
 1505 nants, hadronization<sup>2</sup> and particle decay. Thanks to extensive testing, several  
 1506 optimized parametrizations, known as “tunings”, have been defined in order  
 1507 to improve the description of actual collisions to a high degree of precision; for  
 1508 analysis at  $\sqrt{s} = 13$  TeV, the underline event CUETP8M1 tune is employed [85].  
 1509 The calculation of the matrix element is performed at LO which is not enough  
 1510 for the current required level of precision; therefore, pythia is often used for  
 1511 parton shower, hadronization and decays, while other event generators are used  
 1512 to generate the matrix element at NLO.

---

<sup>2</sup> based in the Lund string model [84]

1513     • **MadGraph5\_aMC@NLO.** MadGraph is a matrix element generator which  
 1514       calculates the amplitudes for all contributing Feynman diagrams of a given pro-  
 1515       cess but does not provide a parton shower while MC@NLO incorporate NLO  
 1516       QCD matrix elements consistently into a parton shower framework; thus, Mad-  
 1517       Graph5\_aMC@NLO, as a merger of the two event generators MadGraph5 and  
 1518       aMC@NLO, is an event generator capable to calculate tree-level and NLO cross  
 1519       sections and perform the matching of those with the parton shower. It is one of  
 1520       the most frequently used matrix element generators; however, it has the partic-  
 1521       ular feature of the presence of negative event weights which reduce the number  
 1522       of events used to reproduce the properties of the objects generated [86].

1523

1524     • **POWHEG.** It is an NLO matrix element generator where the hardest emis-  
 1525       sion of color charged particles is generated in such a way that the negative event  
 1526       weights issue of MadGraph5\_aMC@NLO is overcome; however, the method re-  
 1527       quires an interface with  $p_T$ -ordered parton shower or a parton shower generator  
 1528       where this highest emission can be vetoed in order to avoid double counting of  
 1529       this highest-energetic emission. PYTHIA is a commonly matched to POWHEG  
 1530       event generator [87].

1531 Events resulting from the whole generation process are known as MC events.

### 1532 4.3 CMS detector simulation.

1533 After generation, MC events contain the physics of the collisions but they are not  
 1534 ready to be compared to the events recorded by the experiment since these recorded  
 1535 events correspond to the response of the detection systems to the interaction with

1536 the particles traversing them. The simulation of the CMS detector has to be applied  
1537 on top of the event generation; it is simulated with a MC toolkit for the simulation  
1538 of particles passing through matter called Geant4 which is also able to simulate the  
1539 electronic signals that would be measured by all detectors inside CMS.

1540

1541 The simulation takes the generated particles contained in the MC events as input,  
1542 makes them pass through the simulated geometry, and models physics processes that  
1543 particles experience during their passage through matter. The full set of results from  
1544 particle-matter interactions correspond to the simulated hit which contains informa-  
1545 tion about the energy loss, momentum, position. Particles of the input event are  
1546 called “primary”, while the particles originating from GEANT4-modeled interactions  
1547 of a primary particle with matter are called a “secondary”. Simulated hits are the in-  
1548 put of subsequent modules that emulate the response of the detector readout system  
1549 and triggers. The output from the emulated detection systems and triggers is known  
1550 as digitization [88, 89].

1551

1552 The modeling of the CMS detector corresponds to the accurate modeling of the  
1553 interaction among particles, the detector material, and the magnetic field. This  
1554 simulation procedure includes the following standard steps

- 1555       • Modeling of the Interaction Region.
- 1556       • Modeling of the particle passage through the hierarchy of volumes that compose  
1557            CMS detector and of the accompanying physics processes.
- 1558       • Modeling of the effect of multiple interactions per beam crossing and/or the  
1559            effect of events overlay ( Pile-Up simulation).

1560        • Modeling of the detector’s electronics response, signal shape, noise, calibration  
 1561            constants (digitization).

1562      In addition to the full simulation, i.e. a detailed detector simulation, a faster simula-  
 1563      tion (FastSim) have been developed, that may be used where much larger statistics  
 1564      are required. In FastSim, detector material effects are parametrized and included in  
 1565      the hits; those hits are used as input of the same higher-level algorithms<sup>3</sup> used to an-  
 1566      alyze the recorded events. In this way, comparisons between fast and full simulations  
 1567      can be performed [91].

1568

1569      After the full detector simulation, the output events can be directly compared with  
 1570      events actually recorded in the CMS detector. The collection of MC events that  
 1571      reproduce the expected physics for a given process are known as MC samples.

## 1572      4.4 Event reconstruction.

1573      In contrast to MC samples for which all the particles’ information is available from  
 1574      it’s identity to its mass and energy, recorded events contain the electronic signals,  
 1575      provided by the CMS detection systems, encoding the interaction of physical parti-  
 1576      cles with the detector matter; these electronic signals have to be combined in order  
 1577      to identify these particles and measure their features i.e., particles have to be “recon-  
 1578      structed” using the signals provided by the detection systems. The CMS experiment  
 1579      use the “particle-flow event reconstruction algorithm (PF)” to do the reconstruction  
 1580      of particles produced in  $pp$  collisions. Next sections will present a basic description

---

<sup>3</sup> track fitting, calorimeter clustering, b tagging, electron identification, jet reconstruction and calibration, trigger algorithms which will be considered in the next sections

1581 of the *Elements* used by PF (tracker tracks, energy clusters, and muon tracks), based  
 1582 in the references [92, 93] where more detailed descriptions can be found.

1583 **4.4.1 Particle-Flow Algorithm.**

1584 Each of the several sub detection systems of the CMS detector is dedicated to identi-  
 1585 fying a specific type of particles, i.e., photons and electrons are absorbed by the ECAL  
 1586 and their reconstruction is based on ECAL information; hadrons are reconstructed  
 1587 from clusters in the HCAL while muons are reconstructed from hits in the muon  
 1588 chambers. PF is designed to correlate signals from all the detector layers (tracks and  
 1589 energy clusters) in order to reconstruct and identify each final state particle and its  
 1590 properties as sketched in figure 4.2.

1591

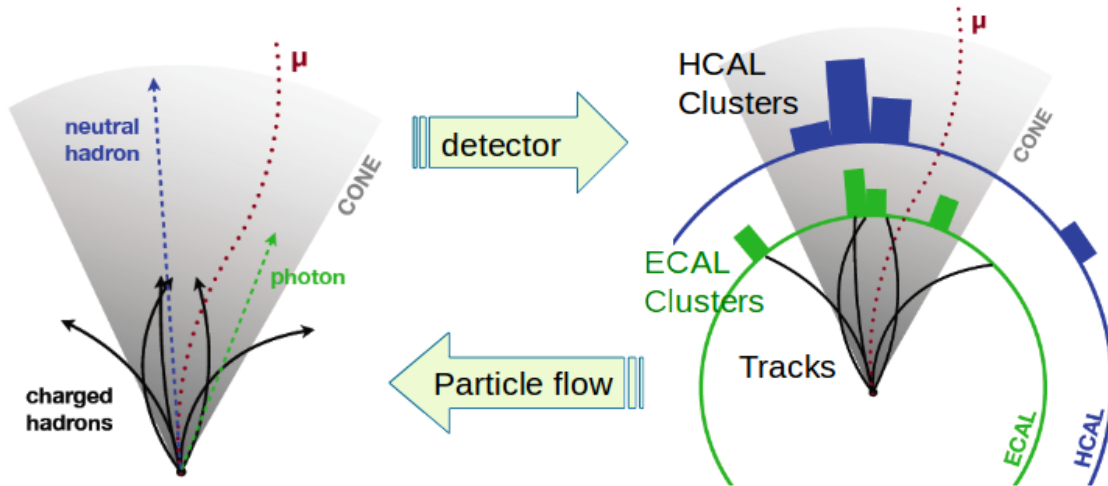


**Figure 4.2:** Particle flow algorithm. Information from the several CMS detection systems if provided as input to the algorithm which then combine it to identify and reconstruct all the particles in the final state and their properties. Reconstruction of simulated events is also performed by providing information from MC samples, detector and trigger simulation [94].

1592 For instance, a charged hadron is identified by a geometrical connection, know as *link*  
 1593 between one or more calorimeter clusters and a track in the tracker provided there

1594 are no hits in the muon system; combining several measurements allows a better  
 1595 determination of the energy and charge sign of the charged hadron.

1596 **Charged-particle track reconstruction.**

1597 The strategy used by PF in order to reconstruct tracks is called “Iterative Tracking”  
 1598 which occurs in four steps

1599 • Seed generation where initial track candidates are found by looking for a combi-  
 1600 nation of hits in the pixel detector, strip tracker, and muon chambers. In total  
 1601 ten iterations are performed, each one with a different seeding requirement.  
 1602 Seeds are used to estimate the trajectory parameters and uncertainties at the  
 1603 time of the full track reconstruction. Seeds are also considered track candidates.

1604 • Track finding using a tracking software known as Combinatorial Track Finder  
 1605 (CTF) [95]. The seed trajectories are extrapolated along the expected flight  
 1606 path of a charged particle, in agreement to the trajectory parameters obtained  
 1607 in the first step, in an attempt to find additional hits that can be assigned to  
 1608 the track candidates.

1609 • Track-fitting where the found tracks are passed as input to a module which  
 1610 provides the best estimate of the parameters of each trajectory.

1611 • Track selection where track candidates are submitted to a selection which dis-  
 1612 cards those that fail a set of defined quality criteria.

1613 Iterations differ in the seeding configuration and the final track selection as elaborated  
 1614 in references [92, 93]. In the first iteration, high  $p_T$  tracks and tracks produced near  
 1615 to the interaction region are identified and those hits are masked thereby reducing  
 1616 the combinatorial complexity. Next iterations search for more complicated tracks,

1617 like low  $p_T$  tracks and tracks from b hadron decays, which tend to be displaced from  
 1618 the interaction region.

1619 **Vertex reconstruction.**

1620 During the track reconstruction, an extrapolation toward to the calorimeters is per-  
 1621 formed in order to match energy deposits; that extrapolation is performed also toward  
 1622 the beamline in order to find the origin of the track known as *vertex*. The vertex re-  
 1623 construction is performed by selecting from the available reconstructed tracks, those  
 1624 that are consistent with being originated in the interaction region where  $pp$  collisions  
 1625 are produced. The selection involves a requirement on the number of tracker (pixel  
 1626 and strip) hits and the goodness of the track fit.

1627

1628 Selected tracks are clustered using a “deterministic annealing algorithm (DA)”<sup>4</sup>. A  
 1629 set of candidate vertices and their associated tracks, resulting from the DA, are then  
 1630 fitted with an “adaptive vertex fitter (AVF)” to produce the best estimate of the  
 1631 vertices locations.

1632

1633 The  $p_T$  of the several tracks associated to a reconstructed vertex is added, squared and  
 1634 used to organize the vertices; the vertex with the highest squared sum is designated  
 1635 as the *primary vertex (PV)* while the rest are designated as PU vertices.

1636 **Calorimeter clustering.**

1637 After traversing the CMS tracker system, electrons, photons and hadrons deposit their  
 1638 energy in the ECAL and HCAL cells. The PF clustering algorithm aims to provide  
 1639 a high detection efficiency even for low-energy particles and an efficient distinction

---

<sup>4</sup> DA algorithm and AVF are described in detail in references [97,98]

1640 between close energy deposits. The clustering runs independently in the ECAL barrel  
 1641 and endcaps, HCAL barrel and endcaps, and the two preshower layers, following two  
 1642 steps

- 1643     • cells with an energy larger than a given seed threshold and larger than the energy  
 1644        of the neighboring cells are identified as cluster seeds. The neighbor cells are  
 1645        those that either share a side with the cluster seed candidate, or the eight closest  
 1646        cells including cells that only share a corner with the seed candidate.
- 1647     • cells with at least a corner in common with a cell already in the cluster seed  
 1648        and with an energy above a cell threshold are grouped into topological clusters.

1649 Clusters formed in this way are known as *particle-flow clusters*. With this clustering  
 1650 strategy, it is possible to detect and measure the energy and direction of photons and  
 1651 neutral hadrons as well as differentiate these neutral particles from the charged hadron  
 1652 energy deposits. In cases involving charged hadrons for which the track parameters  
 1653 are not determined accurately, for instance, low-quality and high- $p_T$  tracks, clustering  
 1654 helps in the energy measurements.

### 1655 **Electron track reconstruction.**

1656 Although the charged-particle track reconstruction described above works for elec-  
 1657 trons, they lose a significant fraction of their energy via bremsstrahlung photon radi-  
 1658 ation before reaching the ECAL; thus, the reconstruction performance depends on the  
 1659 ability to measure also the radiated energy. The reconstruction strategy, in this case,  
 1660 requires information from the tracking system and from the ECAL. Bremsstrahlung  
 1661 photons are emitted at similar  $\eta$  values to that of the electron but at different values  
 1662 of  $\phi$ ; therefore, the radiated energy can be recovered by grouping ECAL clusters in a  
 1663  $\eta$  window over a range of  $\phi$  around the electron direction. The group is called ECAL

1664 supercluster.

1665

1666 Electron candidates from the track-seeding and ECAL super clustering are merged  
 1667 into a single collection which is submitted to a full electron tracking fit with a  
 1668 Gaussian-sum filter (GSF) [96]. The electron track and its associated ECAL su-  
 1669 percluster form a *particle-flow electron*.

## 1670 Muon track reconstruction.

1671 Given that the CMS detector is equipped with a muon spectrometer capable to iden-  
 1672 tify and measure the momentum of the muons traversing it, the muon reconstruction  
 1673 is not specific to PF; therefore, three different muon types are defined

- 1674     • *Standalone muon*. A clustering on the DTs or CSCs hits is performed to form  
   1675       track segments; those segments are used as seeds for the reconstruction in the  
   1676       muon spectrometer. All DTs, CSCs, and RPCs hits along the muon trajectory  
   1677       are combined and fitted to form the full track. The fitting output is called a  
   1678       *standalone-muon track*.
- 1679     • *tracker muon*. Each track in the inner tracker with  $p_T$  larger than 0.5 GeV and  
   1680       a total momentum  $p$  larger than 2.5 GeV is extrapolated to the muon system. A  
   1681       *tracker muon track* corresponds to the extrapolated tracks that match at least  
   1682       one muon segment.
- 1683     • *Global muon*. When tracks in the inner tracker (inner tracks) and standalone-  
   1684       muon tracks are matched and turn out being compatibles, their hits are com-  
   1685       bined and fitted to form a *global-muon track*.

1686 Global muons sharing the same inner track with tracker muons are merged into a  
 1687 single candidate. PF muon identification uses the muon energy deposits in ECAL,  
 1688 HCAL, and HO associated with the muon track to improve the muon identification.

1689 **Particle identification and reconstruction.**

1690 PF elements are connected by a linker algorithm that tests the connection between any  
 1691 pair of elements; if they are found to be linked, a geometrical distance that quantifies  
 1692 the quality of the link is assigned. Two elements may be linked indirectly through  
 1693 common elements. Linked elements form *PF blocks* and a PF block may contain  
 1694 elements originating in one or more particles. Links can be established between  
 1695 tracks, between calorimeter clusters, and between tracks and calorimeter clusters.  
 1696 The identification and reconstruction start with a PF block and proceeds as follows

1697 • Muons. An “isolated global muon” is identified by evaluating the presence of  
 1698 inner track and energy deposits close to the global muon track in the  $(\eta, \phi)$   
 1699 plane, i.e., in a particular point of the global muon track, inner tracks and  
 1700 energy deposits are sought within a radius of  $\Delta R = 0.3$  (see eqn. 3.7) from the  
 1701 muon track; if they exist and the  $p_T$  of the found track added to the  $E_T$  of the  
 1702 found energy deposit does not exceed 10% of the muon  $p_T$  then the global muon  
 1703 is an isolated global muon. This isolation condition is stringent enough to reject  
 1704 hadrons misidentified as muons.

1705 “Non-isolated global muons” are identified using additional selection require-  
 1706 ments on the number of track segments in the muon system and energy deposits  
 1707 along the muon track. Muons inside jets are identified with more stringent crite-  
 1708 ria in isolation and momentum as described in reference [99]. The PF elements  
 1709 associated with an identified muon are masked from the PF block.

- 1710     ● Electrons are identified and reconstructed as described above plus some addi-  
 1711       tional requirements on fourteen variables like the amount of energy radiated,  
 1712       the distance between the extrapolated track position at the ECAL and the po-  
 1713       sition of the associated ECAL supercluster among others, which are combined  
 1714       in a specialized multivariate analysis strategy that improves the electron iden-  
 1715       tification. Tracks and clusters used to identify and reconstruct electrons are  
 1716       masked in the PF block.
  
- 1717     ● Isolated photons are identified from ECAL superclusters with  $E_T$  larger than 10  
 1718       GeV, for which the energy deposited at a distance of 0.15, from the supercluster  
 1719       position on the  $(\eta, \phi)$  plane, does not exceed 10% of the supercluster energy;  
 1720       note that this is an isolation requirement. In addition, there must not be links  
 1721       to tracks. Clusters involved in the identification and reconstruction are masked  
 1722       in the PF block.
  
- 1723     ● Bremsstrahlung photons and prompt photons tend to convert to electron-positron  
 1724       pairs inside the tracker, therefore, a dedicated finder algorithm is used to link  
 1725       tracks that seem to originate from a photon conversion; in case those two tracks  
 1726       are compatible with the direction of a bremsstrahlung photon, they are also  
 1727       linked to the original electron track. Photon conversion tracks are also masked  
 1728       in the PF block.
  
- 1729     ● The remaining elements in the PF block are used to identify hadrons. In the  
 1730       region  $|\eta| \leq 2.5$ , neutral hadrons are identified with HCAL clusters not linked  
 1731       to any track while photons from neutral pion decays are identified with ECAL  
 1732       clusters without links to tracks. In the region  $|\eta| > 2.5$  ECAL clusters linked to  
 1733       HCAL clusters are identified with a charged or neutral hadron shower; ECAL  
 1734       clusters with no links are identified with photons. HCAL clusters not used yet,

1735        are linked to one or more unlinked tracks and to an unlinked ECAL in order to  
 1736        reconstruct charged-hadrons or a combination of photons and neutral hadrons  
 1737        according to certain conditions on the calibrated calorimetric energy.

- 1738        • Charged-particle tracks may be liked together when they converge to a “sec-  
 1739        ondary vertex (SV) ” displaced from the interaction point where the PV and  
 1740        PU vertices are reconstructed; at least three tracks are needed in that case,  
 1741        of which at most one has to be an incoming track with hits in tracker region  
 1742        between a PV and the SV.

1743

1744        The linker algorithm, as well as the whole PF algorithm, has been validated and  
 1745        commissioned; results from that validation are presented in the references [92].

1746        **Jet reconstruction.**

1747        Quarks and gluons may be produced in the  $pp$  collisions, therefore, their hadronization  
 1748        will be seen in the detector as a shower of hadrons and their decay products in the  
 1749        form of a “jet”. The anti- $k_t$  algorithm [100] is used to perform the jet reconstruction  
 1750        by clustering those PF particles within a cone (see figure 4.3); previously, isolated  
 1751        electrons, isolated muons, and charged particles associated with other interaction  
 1752        vertices are excluded from the clustering.

1753        The anti- $k_t$  algorithm proceeds in a sequential recombination of PF particles; the  
 1754        distance between particles  $i$  and  $j$  ( $d_{ij}$ ) and the distance between particles and the  
 1755        beam are defined as

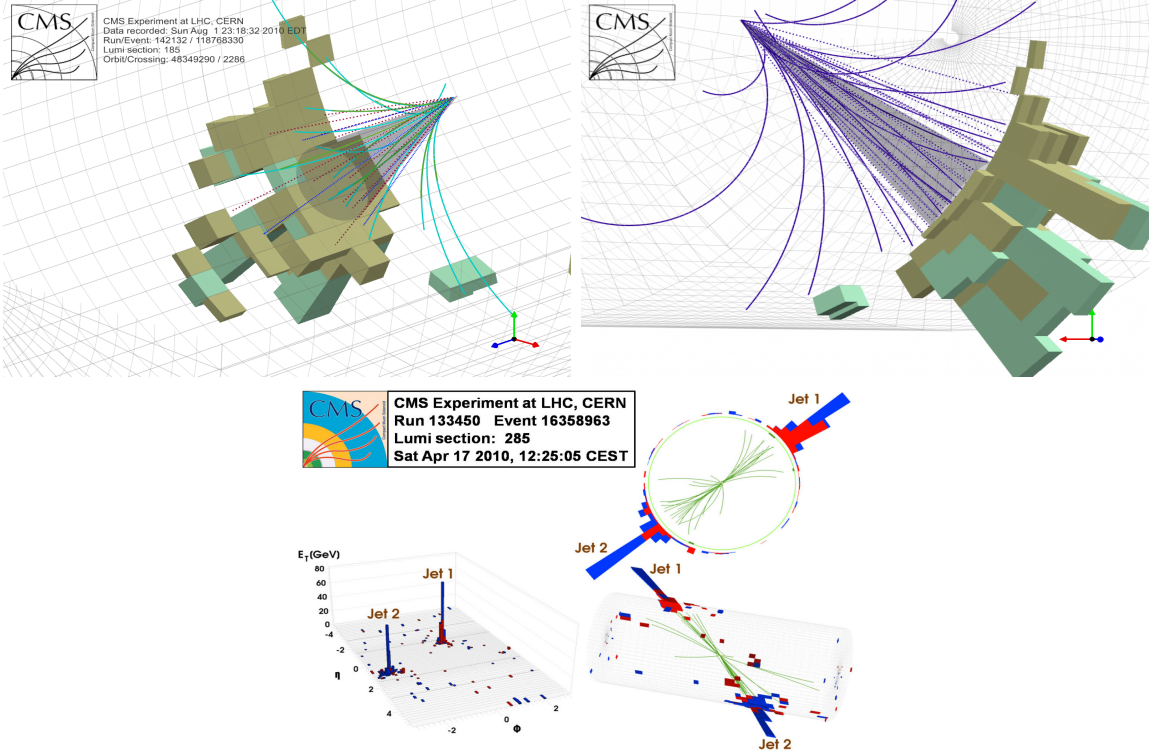


**Figure 4.3:** Jet reconstruction performed by the anti- $k_t$  algorithm. Top: Two different views of a CMS recorded event are presented. Continuous lines correspond to the tracks left by charged particles in the tracker while dotted lines are the imaginary paths followed by neutral particles. The green cubes represent the ECAL cells while the blue ones represent the HCAL cells; in both cases, the height of the cube represent the amount of energy deposited in the cells [101]. Bottom: Reconstruction of a recorded event with two jets [102].

$$d_{ij} = \min\left(\frac{1}{k_{ti}^2}, \frac{1}{k_{tj}^2}\right) \frac{\Delta_{ij}^2}{R^2}$$

$$d_{iB} = \frac{1}{k_{ti}^2} \quad (4.1)$$

1756 where  $\Delta_{ij}^2 = (y_i - y_j)^2 + (\phi_i - \phi_j)^2$ ,  $k_{ti}$ ,  $y_i$  and  $\phi_i$  are the transverse momentum, ra-  
1757 pidity and azimuth of particle  $i$  respectively and  $R$  is the called jet radius. For all  
1758 the remaining PF particles, after removing the isolated ones,  $d_{ij}$  and  $d_{iB}$  are calcu-

lated<sup>5</sup> and the smallest is identified; if it is a  $d_{ij}$ , particles  $i$  and  $j$  are replaced with a new object whose momentum is the vectorial sum of the combined particles. If the smallest distance is a  $d_{iB}$  the clustering process ends, the object  $i$  (which at this stage should be a combination of several PF particles) is declared as a *Particle-flow-jet* (PF jet) and all the associated PF particles are removed from the detector. The clustering process is repeated until no PF particles remain.

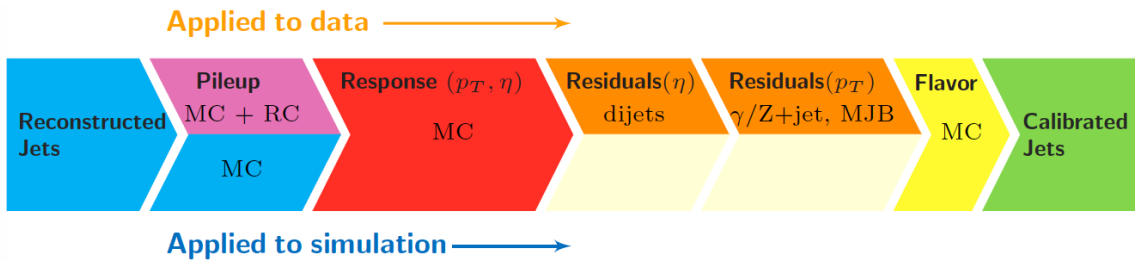


**Figure 4.4:** Jet energy correction diagram. Correction levels are applied sequentially in the indicated fixed order [104].

Even though jets can be reconstructed efficiently, there are some effects that are not included in the reconstruction and that lead to discrepancies between the reconstructed results and the predicted results; in order to overcome these discrepancies, a factorized model has been designed in the form of jet energy corrections (JEC) [103, 104] applied sequentially as shown in the diagram of figure 4.4.

At each level, the jet four-momentum is multiplied by a scaling factor based on jet properties, i.e.,  $\eta$ , flavor, etc.

- Level 1 correction removes the energy coming from pile-up. The scale factor is determined using a MC sample of QCD dijet events with and without pileup overlay; it is parametrized in terms of the offset energy density  $\rho$ , jet area  $A$ , jet  $\eta$  and jet  $p_T$ . Different corrections are applied to data and MC due to the detector simulation.

<sup>5</sup> Notice that this is a combinatorial calculation.

- 1777     • MC-truth correction accounts for differences between the reconstructed jet en-
- 1778         ergy and the MC particle-level energy. The correction is determined on a QCD
- 1779         dijet MC sample and is parametrized in terms of the jet  $p_T$  and  $\eta$ .
- 1780     • Residuals correct remaining small differences within jet response in data and
- 1781         MC. The Residuals  $\eta$ -dependent correction compares jets of similar  $p_T$  in the
- 1782         barrel reference region. The Residuals  $p_T$ -dependent correct the jet absolute
- 1783         scale (JES vs  $p_T$ ).
- 1784     • Jet-flavor corrections are derived in the same way as MC-truth corrections but
- 1785         using QCD pure flavor samples.

1786 ***b*-tagging of jets.**

1787 A particular feature of the hadrons containing bottom quarks (b-hadrons) is that

1788 they have a lifetime long enough to travel some distance before decaying, but it is

1789 not as long as those of light quark hadrons; therefore, when looking at the hadrons

1790 produced in  $pp$  collisions, b-hadrons decay typically inside the tracker rather than

1791 reach the calorimeters as some light-hadrons do. As a result, a b-hadron decay gives

1792 rise to a displaced vertex (secondary vertex) with respect to the primary vertex as

1793 shown in figure 4.5; the SV displacement is in the order of a few millimeters. A jet

1794 resulting from the decay of a b-hadron is called *b* jet; other jets are called light jets.

1795

1796 Several methods to identify *b*-jets (*b*-tagging) have been developed; the method used in

1797 this thesis is known as “Combined Secondary Vertex” algorithm in its second version

1798 (CSVv2) [105]. By using information of the impact parameter, the reconstructed

1799 secondary vertices and the jet kinematics in a multivariate analysis that combines

1800 the discrimination power of each variable in one global discriminator variable, three

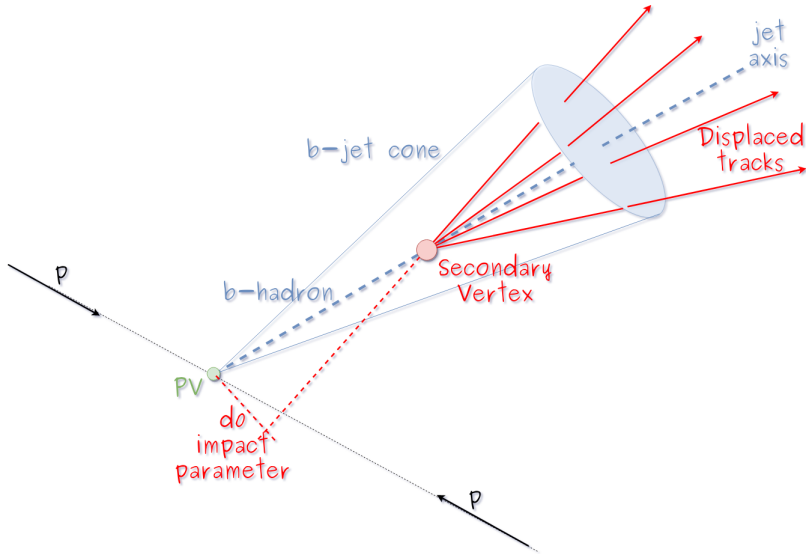


**Figure 4.5:** Secondary vertex in a b-hadron decay.

1801 working points (references): loose, medium and tight, are defined which quantify the  
 1802 probabilities of mistag jets from light quarks as jets from  $b$  quarks; 10, 1 and 0.1 %  
 1803 respectively. Although the mistagging probability decrease with the working point  
 1804 strength, the efficiency to correctly tag  $b$ -jets also decrease as 83, 69 and 49 % for the  
 1805 respective working point; therefore, a balance needs to be achieved according to the  
 1806 specific requirements of the analysis.

### 1807 Missing transverse energy.

1808 The fact that proton bunches carry momentum along the  $z$  axis implies that for each  
 1809 event, momentum balance in the transverse plane is expected. Imbalances are quan-  
 1810 tified by the missing transverse energy (MET) and are attributed to several sources  
 1811 including particles escaping undetected through the beam pipe, neutrinos produced in  
 1812 weak interactions processes which do not interact with the detector and thus escaping  
 1813 without leaving a sign, or even undiscovered particles predicted by models beyond  
 1814 the SM.

1815

1816 The PF algorithm assign the negative sum of the momenta of all reconstructed PF  
 1817 particles to the *particle-flow MET* according to

$$\vec{E}_T = - \sum_i \vec{p}_{T,i} \quad (4.2)$$

1818 JEC are propagated to the calculation of the  $\vec{E}_T$  as described in the reference [106].

1819

#### 1820 4.4.2 Event reconstruction examples

1821 Figures 4.6-4.8 show the results of the reconstruction performed on 3 recorded events.  
 1822 Descriptions are taken directly from the source.

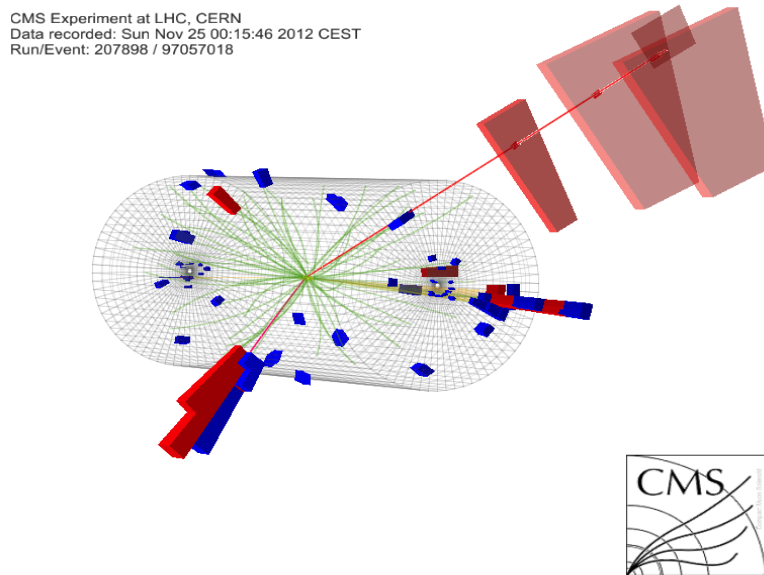


**Figure 4.6:** HIG-13-004 Event 1 reconstruction results; “HIG-13-004 Event 1: Event recorded with the CMS detector in 2012 at a proton-proton center-of-mass energy of 8 TeV. The event shows characteristics expected from the decay of the SM Higgs boson to a pair of  $\tau$  leptons. Such an event is characterized by the production of two forward-going jets, seen here in opposite endcaps. One of the  $\tau$  decays to a muon (red lines on the right) and neutrinos, while the other  $\tau$  decays into a charged hadron and a neutrino.” [?].

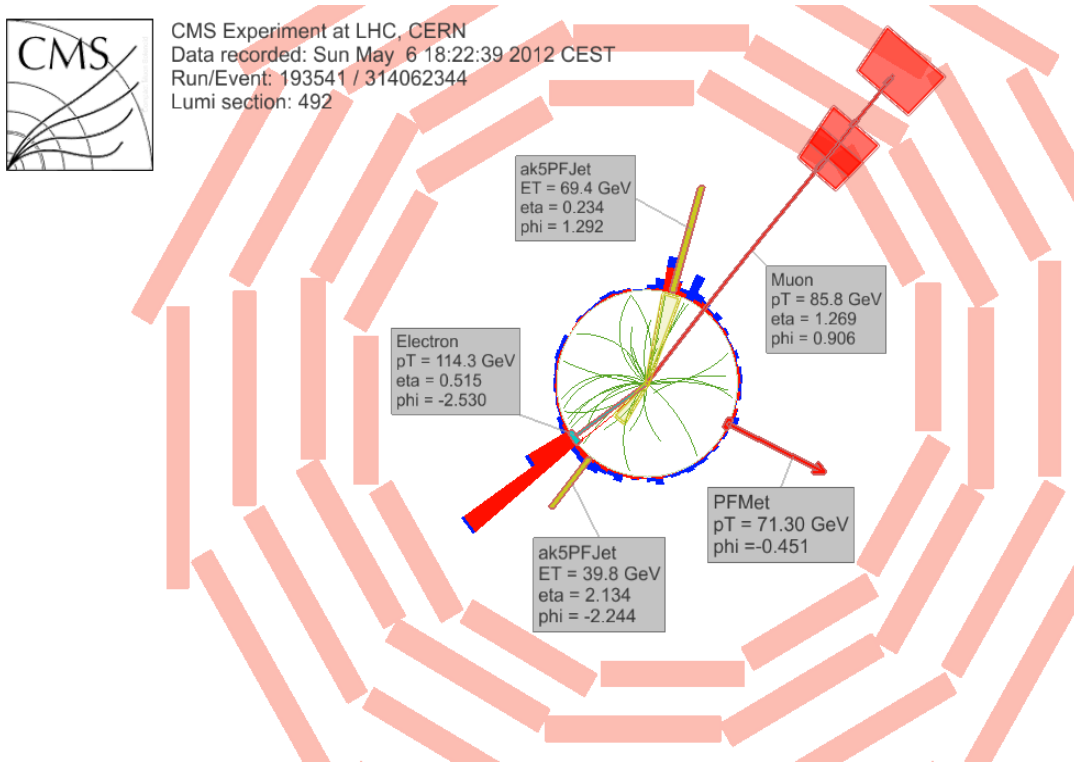


**Figure 4.7:**  $e\mu$  event reconstruction results; “An  $e\mu$  event candidate selected in 8 TeV data, as seen from the direction of the proton beams. The kinematics of the main objects used in the event selection are highlighted: two isolated leptons and two particle-flow jets. The reconstructed missing transverse energy is also displayed for reference” [?].

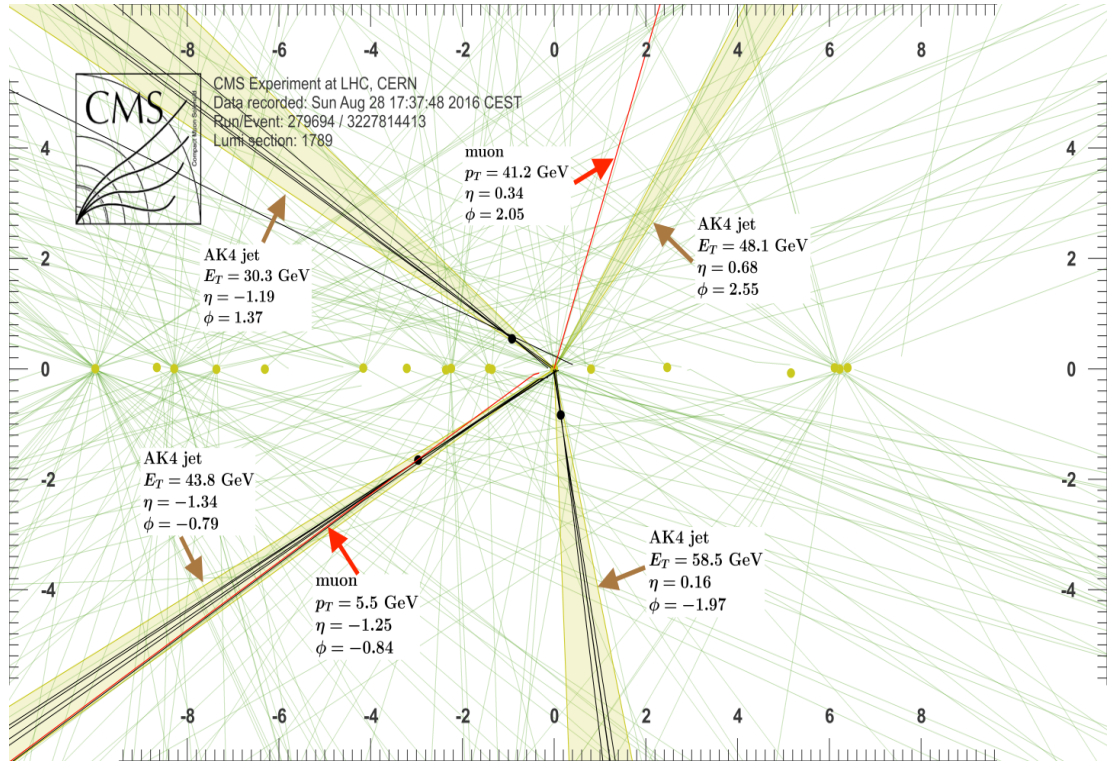


**Figure 4.8:** Recorded event reconstruction results; “Recorded event ( $\rho$ - $z$  projection) with three jets with  $p_T > 30$  GeV with one displaced muon track in 2016 data collected at 13 TeV. Each of the three jets has a displaced reconstructed vertex. The jet with  $p_T(j) = 43.8$  GeV,  $\eta(j) = -1.34$ ,  $\phi(j) = -0.79$  contains muon with  $p_T(\mu) = 5.5$  GeV,  $\eta(\mu) = -1.25$ ,  $\phi(\mu) = -0.84$ . Event contains reconstructed isolated muon with  $p_T(\mu) = 41.2$  GeV,  $\eta(\mu) = 0.34$ ,  $\phi(\mu) = 2.05$  and MET with  $p_T = 72.5$  GeV,  $\phi = -0.32$ . Jet candidates for a  $b$ -jet from top quark leptonic and hadronic decays are tagged by CSVv2T algorithm. One of the other two jets is tagged by CharmT algorithm. Tracks with  $p_T > 0.5$  GeV are shown. The number of reconstructed primary vertices is 18. Reconstructed  $m_T(W)$  is 101.8 GeV. Beam spot position correction is applied. Reconstructed primary vertices are shown in yellow color, while reconstructed displaced vertices and associated tracks are presented in black color. Dimensions are given in cm” [107].

1823 **Chapter 5**

1824 **Statistical methods**

1825 In the course of analyzing the data sets provided by the CMS experiment and used in  
1826 this thesis, several statistical tools have been employed; in this chapter, a description  
1827 of these tools will be presented, starting with the general statement of the multivariate  
1828 analysis method, followed by the particularities of the Boosted Desicion Trees (BDT)  
1829 method and its application to the classification problem. Statistical inference methods  
1830 used will also be presented. This chapter is based mainly on the reference [108].

1831 **5.1 Multivariate analysis**

1832 Multivariate data analysis (MVA) makes reference to statistical techniques that an-  
1833 alyze data containing information of more than one variable, commonly taking into  
1834 account the effects of all variables on the response of the particular variable under  
1835 investigation, i.e., considering all the correlations between variables. MVA is em-  
1836 ployed in a variety of fields like consumer and market research, quality control and  
1837 process optimization. From a MVA it is possible to identify the dominant patterns  
1838 in the data, like groups, outliers and trends, and determine to which group a set of

1839 values belong; in the particle physics context, MVA methods are used to perform the  
 1840 selection of certain type of events, from a large data set, using a potentially large  
 1841 number of measurable properties for each event.

1842 Processes with small cross section, as the  $tHq$  process, normally are hidden behind  
 1843 more common processes; therefore, the data set results in a subset of events with  
 1844 characteristic features of interest (signal) mixed in randomly with a much larger  
 1845 number of SM events that can mimic these features of interest (background) which  
 1846 implies that it is not possible to say with certainty that a given event is signal or  
 1847 background. In that sense, the problem can be formulated as one where a set of  
 1848 events have to be classified according to some features; these features correspond to  
 1849 the measurements of several parameters like energy, momentum organized in a set  
 1850 of “input variables”. The measurements for each event can be written in a vector  
 1851  $\mathbf{x} = (x_1, \dots, x_n)$  for which

- 1852     • Signal hypotheses  $\rightarrow f(\mathbf{x}|s)$  is the probability density for  $\mathbf{x}$  given it is a signal  
   1853       event
- 1854     • Background Hypotheses  $\rightarrow f(\mathbf{x}|b)$  is the probability density of  $\mathbf{x}$  given it is a  
   1855       background event

1856     Figure 5.1 shows three ways to perform a classification of events for which mea-  
 1857       surements of two properties, two input variables, have been performed; blue circles  
 1858       represent signal events while red triangles represent background events. The classifi-  
 1859       cation on (a) is “cut-based” requiring  $x_1 < c_1$  and  $x_2 < c_2$ ; usually the cut values are  
 1860       chosen according to some knowledge about the event process. In (b), the classifica-  
 1861       tion is performed by stating a cut involving a linear function of the input variables  
 1862       and so the boundary, while in (c) the relationship between the input variables is  
 1863       not linear thus the boundary is not linear either.

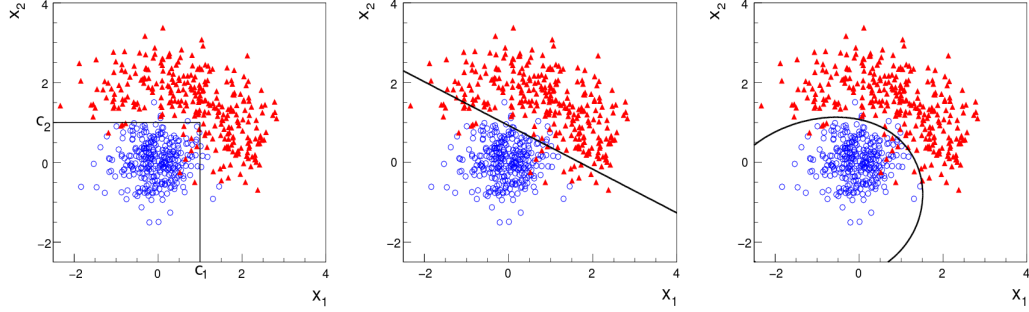


**Figure 5.1:** Scatter plots-MVA event classification. Distribution of two input variables  $x_1$  and  $x_2$  measured for a set of events; blue circles represent signal events and red triangles represent background events. The classification is based on (a) cuts, (b) linear boundary, and (c) nonlinear boundary [108]

1864 **5.2 MVA methods, NN, BDT, boosting,**

1865 **overtraining, variable ranking**

1866 **5.3 statistical inference, likelihood**

1867 **parametrization**

1868 **5.4 nuisance parameters**

1869 **5.5 exclusion limits**

1870 **5.6 asymptotic limits**

<sup>1871</sup> **Chapter 6**

<sup>1872</sup> **Search for production of a Higgs**

<sup>1873</sup> **boson and a single top quark in**

<sup>1874</sup> **multilepton final states in pp**

<sup>1875</sup> **collisions at  $\sqrt{s} = 13$  TeV**

<sup>1876</sup> **6.1 Introduction**

<sup>1877</sup> Dont forget to mention previous constrains to ct check reference ?? and references

<sup>1878</sup> <https://link.springer.com/content/pdf/10.1007%2FJHEP01>

<sup>1879</sup> A. Azatov, R. Contino and J. Galloway,  $\rightarrow$ IJModel-Independent Bounds on a

<sup>1880</sup> Light Higgs, $\rightarrow$ JHEP 1204 (2012) 127 [arXiv:1202.3415 [hep-ph]].

<sup>1881</sup> J. R. Espinosa, C. Grojean, M. Muhlleitner and M. Trott,  $\rightarrow$ IJFingerprinting

<sup>1882</sup> Higgs Suspects at the LHC, $\rightarrow$ JHEP 1205 (2012) 097 [arXiv:1202.3697 [hep-ph]].

<sup>1883</sup> This chapter present the search for the associated production of a Higgs boson and

<sup>1884</sup> a single top quark events with three leptons in the final state, targeting Higgs decay

1885 modes to  $WW$ ,  $ZZ$ , and  $\tau\tau$ . The analysis uses the 13 TeV dataset produced in 2016,  
 1886 corresponding to an integrated luminosity of  $35.9 fb^{-1}$ . It is based on and expands  
 1887 previous analyses at 8 TeV [?, ?] and searches for associated production of  $t\bar{t}$  and  
 1888 Higgs in the same channel [?], and complements searches in other decay channels  
 1889 targeting  $H \rightarrow b\bar{b}$  [?].  
 1890 As showed in section 2.4, the cross section of the associated production of a Higgs  
 1891 boson and a single top quark ( $tHq$ ) process is driven by a destructive interference of  
 1892 two contributions (see Figure 6.1), where the Higgs couples to either the W boson or  
 1893 the top quark. Any deviation from the standard model (SM) in the Higgs coupling  
 1894 structure could therefore lead to a large enhancement of the cross section, making  
 1895 this analysis sensitive to such deviations. A second process, where the Higgs and  
 1896 top quark are accompanied by a W boson ( $tHW$ ) has similar behavior, albeit with a  
 1897 weaker interference pattern.

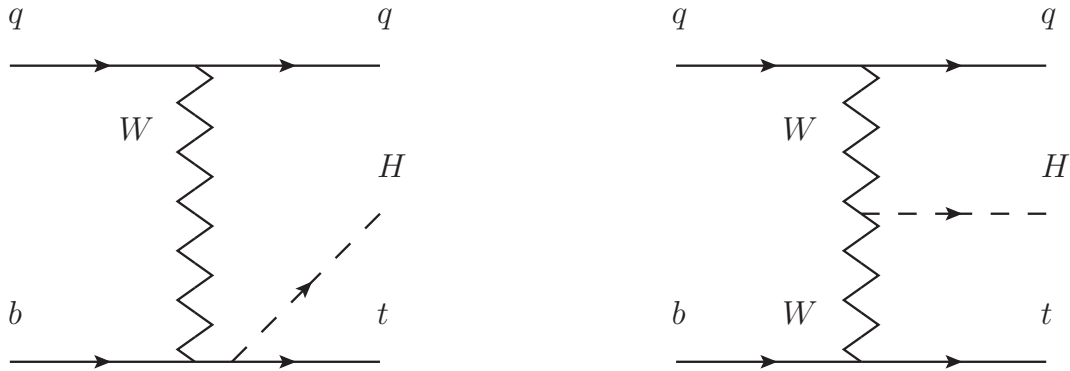


**Figure 6.1:** The two leading-order diagrams of  $tHq$  production.

1898 We selects events with three leptons and a  $b$  tagged jet in the final state. The  $tHq$   
 1899 signal contribution is then determined in a fit of the observed data to two multivariate  
 1900 classifier outputs, each trained to discriminate against one of the two dominant back-  
 1901 grounds of events with non-prompt leptons from  $t\bar{t}$  and of associated production of  $t\bar{t}$

1902 and vector bosons ( $t\bar{t}W$ ,  $t\bar{t}Z$ ). The fit result is then used to set an upper limit on the  
 1903 combined  $t\bar{t}H$ ,  $tHq$  and  $tHW$  production cross section, as a function of the relative  
 1904 coupling strengths of Higgs and top quark and Higgs and W boson, respectively.

## 1905 6.2 Data and MC Samples

1906 The data considered in this analysis were collected by the CMS experiment dur-  
 1907 ing 2016 and correspond to a total integrated luminosity of  $35.9\text{fb}^{-1}$ . Only periods  
 1908 when the CMS magnet was on were considered when selecting the data samples, that  
 1909 corresponds to the 23 Sep 2016 (Run B to G) and PromptReco (Run H) versions  
 1910 of the datasets. The MC samples used in this analysis correspond to the RunI-  
 1911 ISummer16MiniAODv2 campaign produced with CMSSW 80X. The two signal sam-  
 1912 ples (for  $tHq$  and  $tHW$ ) were produced with MG5\_aMC@NLO (version 5.222), in  
 1913 leading-order mode, and are normalized to next-to-leading-order cross sections,  
 1914 see Tab. 6.1. Each sample is generated with a set of event weights corresponding to  
 1915 different values of  $\kappa_t$  and  $\kappa_V$  couplings as shown in Tab. 6.2.

### 1916 6.2.1 Full 2016 dataset and MC samples

Sample	$\sigma$ [pb]	BF
/THQ_Hincl_13TeV-madgraph-pythia8_TuneCUETP8M1/	0.7927	0.324
/THW_Hincl_13TeV-madgraph-pythia8_TuneCUETP8M1/	0.1472	1.0

**Table 6.1:** Signal samples and their cross section and branching fraction used in this analysis. See Ref. [?] for more details.

1917 Different MC generators were used to generate the background processes. The  
 1918 dominant sources ( $t\bar{t}$ ,  $t\bar{t}W$ ,  $t\bar{t}Z$ ,  $t\bar{t}H$ ) were produced using AMC@NLO interfaced  
 1919 to PYTHIA8, and are scaled to NLO cross sections. Other processes are simulated

		<i>tHq</i>		<i>tHW</i>		
$\kappa_V$	$\kappa_t$	sum of weights	cross section [pb]	sum of weights	cross section [pb]	LHE weights
1.0	-3.0	35.700022	2.991	11.030445	0.6409	LHEweight_wgt[446]
1.0	-2.0	20.124298	1.706	5.967205	0.3458	LHEweight_wgt[447]
1.0	-1.5	14.043198	1.205	4.029093	0.2353	LHEweight_wgt[448]
1.0	-1.25	11.429338	0.9869	3.208415	0.1876	LHEweight_wgt[449]
1.0	-1.0		0.7927		0.1472	
1.0	-0.75	7.054998	0.6212	1.863811	0.1102	LHEweight_wgt[450]
1.0	-0.5	5.294518	0.4723	1.339886	0.07979	LHEweight_wgt[451]
1.0	-0.25	3.818499	0.3505	0.914880	0.05518	LHEweight_wgt[452]
1.0	0.0	2.627360	0.2482	0.588902	0.03881	LHEweight_wgt[453]
1.0	0.25	1.719841	0.1694	0.361621	0.02226	LHEweight_wgt[454]
1.0	0.5	1.097202	0.1133	0.233368	0.01444	LHEweight_wgt[455]
1.0	0.75	0.759024	0.08059	0.204034	0.01222	LHEweight_wgt[456]
1.0	1.0	0.705305	0.07096	0.273617	0.01561	LHEweight_wgt[457]
1.0	1.25	0.936047	0.0839	0.442119	0.02481	LHEweight_wgt[458]
1.0	1.5	1.451249	0.1199	0.709538	0.03935	LHEweight_wgt[459]
1.0	2.0	3.335034	0.2602	1.541132	0.08605	LHEweight_wgt[460]
1.0	3.0	10.516125	0.8210	4.391335	0.2465	LHEweight_wgt[461]
1.5	-3.0	45.281492	3.845	13.426212	0.7825	LHEweight_wgt[462]
1.5	-2.0	27.606715	2.371	7.809713	0.4574	LHEweight_wgt[463]
1.5	-1.5	20.476088	1.784	5.594971	0.3290	LHEweight_wgt[464]
1.5	-1.25	17.337465	1.518	4.635978	0.2749	LHEweight_wgt[465]
1.5	-1.0	14.483302	1.287	3.775902	0.2244	LHEweight_wgt[466]
1.5	-0.75	11.913599	1.067	3.014744	0.1799	LHEweight_wgt[467]
1.5	-0.5	9.628357	0.874	2.352505	0.1410	LHEweight_wgt[468]
1.5	-0.25	7.627574	0.702	1.789184	0.1081	LHEweight_wgt[469]
1.5	0.0	5.911882	0.5577	1.324946	0.08056	LHEweight_wgt[470]
1.5	0.25	4.479390	0.4365	0.959295	0.05893	LHEweight_wgt[471]
1.5	0.5	3.331988	0.3343	0.692727	0.04277	LHEweight_wgt[472]
1.5	0.75	2.469046	0.2558	0.525078	0.03263	LHEweight_wgt[473]
1.5	1.0	1.890565	0.2003	0.456347	0.02768	LHEweight_wgt[474]
1.5	1.25	1.596544	0.1689	0.486534	0.02864	LHEweight_wgt[475]
1.5	1.5	1.586983	0.1594	0.615638	0.03509	LHEweight_wgt[476]
1.5	2.0	2.421241	0.2105	1.170602	0.06515	LHEweight_wgt[477]
1.5	3.0	7.503280	0.5889	3.467546	0.1930	LHEweight_wgt[478]
0.5	-3.0	27.432685	2.260	8.929074	0.5136	LHEweight_wgt[479]
0.5	-2.0	13.956013	1.160	4.419093	0.2547	LHEweight_wgt[480]
0.5	-1.5	8.924438	0.7478	2.757611	0.1591	LHEweight_wgt[481]
0.5	-1.25	6.835341	0.5726	2.075247	0.1204	LHEweight_wgt[482]
0.5	-1.0	5.030704	0.4273	1.491801	0.08696	LHEweight_wgt[483]
0.5	-0.75	3.510528	0.2999	1.007273	0.05885	LHEweight_wgt[484]
0.5	-0.5	2.274811	0.1982	0.621663	0.03658	LHEweight_wgt[485]
0.5	-0.25	1.323555	0.1189	0.334972	0.01996	LHEweight_wgt[486]
0.5	0.0	0.656969	0.06223	0.147253	0.008986	LHEweight_wgt[487]
0.5	0.25	0.274423	0.02830	0.058342	0.003608	LHEweight_wgt[488]
0.5	0.5	0.176548	0.01778	0.068404	0.003902	LHEweight_wgt[489]
0.5	0.75	0.363132	0.03008	0.177385	0.009854	LHEweight_wgt[490]
0.5	1.0	0.834177	0.06550	0.385283	0.02145	LHEweight_wgt[491]
0.5	1.25	1.589682	0.1241	0.692099	0.03848	LHEweight_wgt[492]
0.5	1.5	2.629647	0.2047	1.097834	0.06136	LHEweight_wgt[493]
0.5	2.0	5.562958	0.4358	2.206057	0.1246	LHEweight_wgt[494]
0.5	3.0	14.843102	1.177	5.609519	0.3172	LHEweight_wgt[495]

**Table 6.2:**  $\kappa_V$  and  $\kappa_t$  combinations generated for the two signal samples and their NLO cross sections. The *tHq* cross section is multiplied by the branching fraction of the enforced leptonic decay of the top quark (0.324). See also Ref. [?].

Sample	$\sigma$ [pb]
TTWJetsToLNu_TuneCUETP8M1_13TeV-amcatnloFXFX-madspin-pythia8	0.2043
TTZToLLNuNu_M-10_TuneCUETP8M1_13TeV-amcatnlo-pythia8	0.2529
tthJetToNonbb_M125_13TeV_amcatnloFXFX_madspin_pythia8_mWCutfix /store/cmst3/group/susy/gpetrucc/13TeV/u/TTLL_m1to10_L0_NoMS_for76X/	0.2151 0.0283
WGToLNuG_TuneCUETP8M1_13TeV-madgraphMLM-pythia8	585.8
ZGTo2LG_TuneCUETP8M1_13TeV-amcatnloFXFX-pythia8	131.3
TGJets_TuneCUETP8M1_13TeV_amcatnlo_madspin_pythia8	2.967
TGJets_TuneCUETP8M1_13TeV_amcatnlo_madspin_pythia8	2.967
TTGJets_TuneCUETP8M1_13TeV-amcatnloFXFX-madspin-pythia8	3.697
WpWpJJ_EWK_QCD_TuneCUETP8M1_13TeV-madgraph-pythia8	0.03711
ZZZ_TuneCUETP8M1_13TeV-amcatnlo-pythia8	0.01398
WWZ_TuneCUETP8M1_13TeV-amcatnlo-pythia8	0.1651
WZZ_TuneCUETP8M1_13TeV-amcatnlo-pythia8	0.05565
WW_DoubleScattering_13TeV-pythia8	1.64
tZq_ll_4f_13TeV-amcatnlo-pythia8_TuneCUETP8M1	0.0758
ST_tWll_5f_LO_13TeV-MadGraph-pythia8	0.01123
TTTT_TuneCUETP8M1_13TeV-amcatnlo-pythia8	0.009103
WZTo3LNu_TuneCUETP8M1_13TeV-powheg-pythia8	4.4296
ZZTo4L_13TeV_powheg_pythia8	1.256
TTJets_SingleLeptFromTbar_TuneCUETP8M1_13TeV-madgraphMLM-pythia8	182.1754
TTJets_SingleLeptFromT_TuneCUETP8M1_13TeV-madgraphMLM-pythia8	182.1754
TTJets_DiLept_TuneCUETP8M1_13TeV-madgraphMLM-pythia8	87.3
DYJetsToLL_M-10to50_TuneCUETP8M1_13TeV-amcatnloFXFX-pythia8	18610
DYJetsToLL_M-50_TuneCUETP8M1_13TeV-madgraphMLM-pythia8	6024
WJetsToLNu_TuneCUETP8M1_13TeV-amcatnloFXFX-pythia8	61526.7
ST_tW_top_5f_inclusiveDecays_13TeV-powheg-pythia8_TuneCUETP8M1	35.6
ST_tW_antitop_5f_inclusiveDecays_13TeV-powheg-pythia8_TuneCUETP8M1	35.6
ST_t-channel_4f_leptonDecays_13TeV-amcatnlo-pythia8_TuneCUETP8M1	70.3144
ST_t-channel_antitop_4f_leptonDecays_13TeV-powheg-pythia8_TuneCUETP8M1	26.2278
ST_s-channel_4f_leptonDecays_13TeV-amcatnlo-pythia8_TuneCUETP8M1	3.68064
WWTo2L2Nu_13TeV-powheg	10.481

**Table 6.3:** List of background samples used in this analysis (CMSSW 80X). In the first section of the table are listed the samples of the processes for which we use the simulation to extract the final yields and shapes, in the second section the samples of the processes we will estimate from data. The MC simulation is used to design the data driven methods and derive the associated systematics.

Sample	$\sigma$ [pb]
ttWJets_13TeV_madgraphMLM	0.6105
ttZJets_13TeV_madgraphMLM	0.5297/0.692

**Table 6.4:** Leading-order  $t\bar{t}W$  and  $t\bar{t}Z$  samples used in the signal BDT training.

1920 using POWHEG interfaced to PYTHIA, or bare PYTHIA (see table 6.3 and [?] for  
1921 more details).

Three lepton and Four lepton
HLT_DiMu9_Ele9_CaloIdL_TrackIdL_v*
HLT_Mu8_DiEle12_CaloIdL_TrackIdL_v*
HLT_TripleMu_12_10_5_v*
HLT_Ele16_Ele12_Ele8_CaloIdL_TrackIdL_v*
HLT_Mu23_TrkIsoVVL_Ele8_CaloIdL_TrackIdL_IsoVL_v*
HLT_Mu23_TrkIsoVVL_Ele8_CaloIdL_TrackIdL_IsoVL_DZ_v*
HLT_Mu8_TrkIsoVVL_Ele23_CaloIdL_TrackIdL_IsoVL_v*
HLT_Mu8_TrkIsoVVL_Ele23_CaloIdL_TrackIdL_IsoVL_DZ_v*
HLT_Ele23_Ele12_CaloIdL_TrackIdL_IsoVL_DZ_v*
HLT_Mu17_TrkIsoVVL_Mu8_TrkIsoVVL_DZ_v*
HLT_Mu17_TrkIsoVVL_TkMu8_TrkIsoVVL_DZ_v*
HLT_IsoMu22_v*
HLT_IsoTkMu22_v*
HLT_IsoMu22_eta2p1_v*
HLT_IsoTkMu22_eta2p1_v*
HLT_IsoMu24_v*
HLT_IsoTkMu24_v*
HLT_Ele27_WPTight_Gsf_v*
HLT_Ele25_eta2p1_WPTight_Gsf_v*
HLT_Ele27_eta2p1_WPLoose_Gsf_v*

**Table 6.5:** Table of high-level triggers that we consider in the analysis.

## 1922 6.2.2 Triggers

1923 We consider online-reconstructed events triggered by one, two, or three leptons.  
 1924 Single-lepton triggers are included to boost the acceptance of events where the  $p_T$  of  
 1925 the sub-leading lepton falls below the threshold of the double-lepton triggers. Ad-  
 1926 ditionally, by including double-lepton triggers in the  $\geq 3$  lepton category, as well  
 1927 as single-lepton triggers in all categories, we increase the efficiency, considering the  
 1928 logical “or” of the trigger decisions of all the individual triggers in a given category.  
 1929 Tab. 6.5 shows the lowest-threshold non-prescaled triggers present in the High-Level  
 1930 Trigger (HLT) menus for both Monte-Carlo and data in 2016.

### 1931 6.2.2.1 Trigger efficiency scale factors

1932 The efficiency of events to pass the trigger is measured in simulation (trivially using  
 1933 generator information) and in the data (using event collected by an uncorrelated

Category	Scale Factor
ee	$1.01 \pm 0.02$
e $\mu$	$1.01 \pm 0.01$
$\mu\mu$	$1.00 \pm 0.01$
3l	$1.00 \pm 0.03$

**Table 6.6:** Trigger efficiency scale factors and associated uncertainties, shown here rounded to the nearest percent.

1934 MET trigger). Small differences between the data and MC efficiencies are corrected  
 1935 by applying scale factors as shown in Tab. 6.6. The exact procedure and control plots  
 1936 are documented in [?] for the current analysis.

## 1937 6.3 Object Identification and event selection

### 1938 6.3.1 Jets and $b$ tagging

1939 The analysis uses anti- $k_t$  (0.4) particle-flow (PF) jets, corrected for charged hadrons  
 1940 not coming from the primary vertex (charged hadron subtraction), and having jet  
 1941 energy corrections (`Summer16_23Sep2016V3`) applied as a function of the jet  $E_T$  and  
 1942  $\eta$ . Jets are only considered if they have a transverse energy above 25GeV.

1943 In addition, they are required to be separated from any lepton candidates passing  
 1944 the fakeable object selections (see Tables 6.7 and 6.8) by  $\Delta R > 0.4$ .

1945 The loose and medium working points of the CSV b-tagging algorithm are used to  
 1946 identify  $b$  jets. Data/simulation differences in the  $b$  tagging performance are corrected  
 1947 by applying per-jet weights to the simulation, dependent on the jet  $p_T$ , eta,  $b$  tagging  
 1948 discriminator, and flavor (from simulation truth) [?]. The per-event weight is taken  
 1949 as the product of the per-jet weights, including those of the jets associated to the  
 1950 leptons. More details can be found in the corresponding  $t\bar{t}H$  documentation [?, ?].

1951 **6.3.2 Lepton selection**

Cut	Loose	Fakeable object	Tight
$ \eta  < 2.4$	✓	✓	✓
$p_T$	$> 5\text{GeV}$	$> 15\text{GeV}$	$> 15\text{GeV}$
$ d_{xy}  < 0.05 \text{ (cm)}$	✓	✓	✓
$ d_z  < 0.1 \text{ (cm)}$	✓	✓	✓
$\text{SIP}_{3D} < 8$	✓	✓	✓
$I_{\text{mini}} < 0.4$	✓	✓	✓
is Loose Muon	✓	✓	✓
jet CSV	—	$< 0.8484$	$< 0.8484$
is Medium Muon	—	—	✓
tight-charge	—	—	✓
lepMVA $> 0.90$	—	—	✓

**Table 6.7:** Requirements on each of the three muon selections. In the cases where the cut values change between the selections, those values are listed in the table. Otherwise, whether the cut is applied is indicated. For the two  $p_T^{\text{ratio}}$  and CSV rows, the cuts marked with a † are applied to leptons that fail the lepton MVA cut, while the loose cut value is applied to those that pass the lepton MVA cut.

1952        The lepton reconstruction and selection is identical to that used in the  $t\bar{t}H$  mul-  
 1953 tilepton analysis, as documented in Refs. [?, ?]. For details on the reconstruction  
 1954 algorithms, isolation, pileup mitigation, and a description of the lepton MVA dis-  
 1955 criminator and validation plots thereof, we refer to that document since they are out  
 1956 of the scope of this thesis. Three different selections are defined both for the electron  
 1957 and muon object identification: the *Loose*, *Fakeable Object*, and *Tight* selection. As  
 1958 described in more detail later, these are used for event level vetoes, the fake rate  
 1959 estimation application region, and the final signal selection, respectively. The  $p_T$  of  
 1960 fakeable objects is defined as  $0.85 \times p_T(\text{jet})$ , where the jet is the one associated to the  
 1961 lepton object. This mitigates the dependence of the fake rate on the momentum of  
 1962 the fakeable object and thereby improves the precision of the method.

1963        Tables 6.7 and 6.8 list the full criteria for the different selections of muons and  
 1964 electrons.

Cut	Loose	Fakeable Object	Tight
$ \eta  < 2.5$	✓	✓	✓
$p_T$	$> 7\text{GeV}$	$> 15\text{GeV}$	$> 15\text{GeV}$
$ d_{xy}  < 0.05 \text{ (cm)}$	✓	✓	✓
$ d_z  < 0.1 \text{ (cm)}$	✓	✓	✓
$\text{SIP}_{3D} < 8$	✓	✓	✓
$I_{\text{mini}} < 0.4$	✓	✓	✓
MVA ID $> (0.0, 0.0, 0.7)$	✓	✓	✓
$\sigma_{in\eta} < (0.011, 0.011, 0.030)$	—	✓	✓
$\text{H/E} < (0.10, 0.10, 0.07)$	—	✓	✓
$\Delta\eta_{in} < (0.01, 0.01, 0.008)$	—	✓	✓
$\Delta\phi_{in} < (0.04, 0.04, 0.07)$	—	✓	✓
$-0.05 < 1/E - 1/p < (0.010, 0.010, 0.005)$	—	✓	✓
$p_T^{\text{ratio}}$	—	$> 0.5^\dagger / -$	—
jet CSV	—	$< 0.3^\dagger / < 0.8484$	$< 0.8484$
tight-charge	—	—	✓
conversion rejection	—	—	✓
Number of missing hits	$< 2$	$== 0$	$== 0$
lepMVA $> 0.90$	—	—	✓

**Table 6.8:** Criteria for each of the three electron selections. In cases where the cut values change between selections, those values are listed in the table. Otherwise, whether the cut is applied is indicated. In some cases, the cut values change for different  $\eta$  ranges. These ranges are  $0 < |\eta| < 0.8$ ,  $0.8 < |\eta| < 1.479$ , and  $1.479 < |\eta| < 2.5$  and the respective cut values are given in the form (value<sub>1</sub>, value<sub>2</sub>, value<sub>3</sub>).

### 1965 6.3.3 Lepton selection efficiency

1966 Efficiencies of reconstruction and selecting loose leptons are measured both for muons  
 1967 and electrons using a tag and probe method on both data and MC, using  $Z \rightarrow \ell^+ \ell^-$ .  
 1968 Corresponding scale factors are derived from the ratio of efficiencies and applied to the  
 1969 selected These. Events are produced for the leptonic SUSY analyses using equivalent  
 1970 lepton selections and recycled for the  $t\bar{t}H$  analysis as well as for this analysis. The  
 1971 efficiencies of applying the tight selection as defined in Tables 6.7 and 6.8, on the  
 1972 loose leptons are determined again by using a tag and probe method on a sample of  
 1973 DY-enriched events. They are documented for the  $t\bar{t}H$  analysis in Ref. [?] and are  
 1974 exactly equivalent for this analysis.

## 1975 6.4 Background predictions

1976 The modeling of reducible and irreducible backgrounds in this analysis uses the exact  
 1977 methods, analysis code, and ROOT trees used for the  $t\bar{t}H$  multilepton analysis. We  
 1978 give a brief description of the methods and refer to the documentation of that analysis  
 1979 in Refs. [?, ?] for any details.

1980 The backgrounds in three-lepton final states can be split in two broad categories:  
 1981 irreducible backgrounds with genuine prompt leptons (i.e. from on-shell W and Z  
 1982 boson decays); and reducible backgrounds where at least one of the leptons is “non-  
 1983 prompt”, i.e. produced within a hadronic jet, either a genuine lepton from heavy  
 1984 flavor decays, or simply mis-reconstructed jets.

1985 Irreducible backgrounds can be reliably estimated directly from Monte-Carlo sim-  
 1986 ulated events, using higher-order cross sections or data control regions for the overall  
 1987 normalization. This is done in this analysis for all backgrounds involving prompt lep-  
 1988 tons:  $t\bar{t}W$ ,  $t\bar{t}Z$ ,  $t\bar{t}H$ ,  $WZ$ ,  $ZZ$ ,  $W^\pm W^\pm qq$ ,  $t\bar{t}t\bar{t}$ ,  $tZq$ ,  $tZW$ ,  $WWW$ ,  $WWZ$ ,  $WZZ$ ,  
 1989  $ZZZ$ .

1990 Reducible backgrounds, on the other hand, are not well predicted by simulation,  
 1991 and are estimated using data-driven methods. In the case of non-prompt leptons, a  
 1992 fake rate method is used, where the contribution to the final selection is estimated by  
 1993 extrapolating from a sideband (or “application region”) with a looser lepton definition  
 1994 (the fakeable object definitions in Tabs. 6.7 and 6.8) to the signal selection. The tight-  
 1995 to-loose ratios (or “fake rates”) are measured in several background dominated data  
 1996 events with dedicated triggers, subtracting the residual prompt lepton contribution  
 1997 using MC. Non-prompt leptons in our signal regions are predominantly produced in  $t\bar{t}$   
 1998 events, with a much smaller contribution, from Drell–Yan production. The systematic  
 1999 uncertainty on the normalization of the non-prompt background estimation is on the

order of 50%, and thereby one of the dominant limitations on the performance of multilepton analyses in general and this analysis in particular. It consists of several individual sources, such as the result of closure tests of the method using simulated events, limited statistics in the data control regions due to necessary prescaling of lepton triggers, and the uncertainty in the subtraction of residual prompt leptons from the control region.

The fake background where the leptons pass the looser selection are weighted according to how many of them fail the tight criteria. Events with a single failing lepton are weighted with the factor  $f/(1-f)$  for the estimate to the tight selection region, where  $f$  is the fake rate. Events with two failing leptons are given the negative weight  $-f_i f_j / (1-f_i)(1-f_j)$ , and for three leptons the weight is positive and equal to the product of  $f/(1-f)$  factor evaluated for each failing lepton.

Figures 6.2 show the distributions of some relevant kinematic variables, normalized to the cross section of the respective processes and to the integrated luminosity.

## 6.5 Signal discrimination

The  $tHq$  signal is separated from the main backgrounds using a boosted decision tree (BDT) classifier, trained on simulated signal and background events. A set of discriminating variables are given as input to the BDT which produces a output distribution maximizing the discrimination power. Table 6.9 lists the input variables used while Figures 6.3 show their distributions for the relevant signal and background samples, for the three lepton channel. Two BDT classifiers are trained for the two main backgrounds expected in the analysis: events with prompt leptons from  $t\bar{t}W$  and  $t\bar{t}Z$ (also referred to as  $t\bar{t}V$ ), and events with non-prompt leptons from  $t\bar{t}$ . The datasets used in the training are the  $tHq$  signal (see Tab. 6.1), and LO MADGRAPH samples

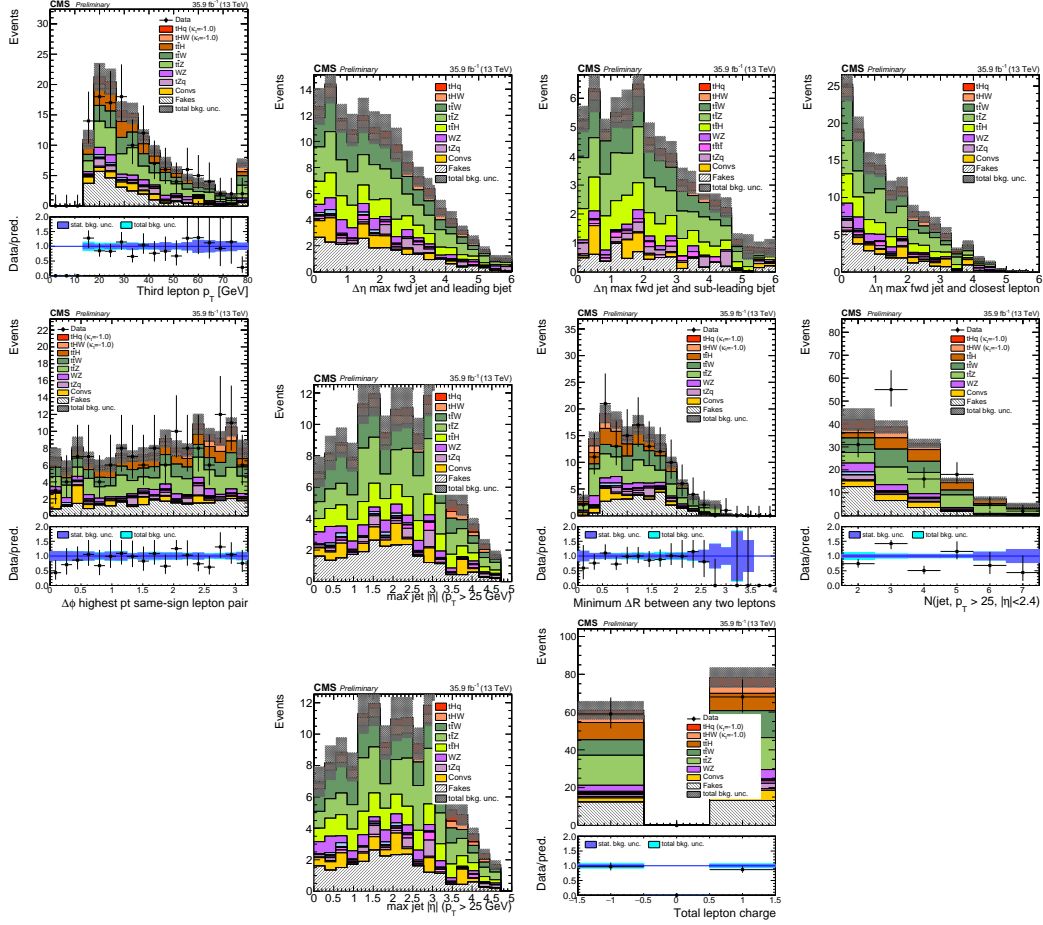


**Figure 6.2:** Distributions of input variables to the BDT for signal discrimination, three lepton channel, normalized to their cross section and to  $35.9\text{fb}^{-1}$ .

of  $t\bar{t}W$  and  $t\bar{t}Z$ , in an admixture proportional to their respective cross sections (see Tab. 6.4).

The MVA analysis consist of two stages: first a “training” where the MVA method is trained to discriminate between simulated signal and background events, then a “test” stage where the trained algorithm is used to classify different events from the samples. The sample is obtained from a pre-selection (see Tab. ?? with pre-selection cuts). Figures 6.4 show the input variables distributions as seen by the MVA algorithm. Note that in contrast to the distributions in Fig. 6.3 only the main backgrounds ( $t\bar{t}$  from simulation,  $t\bar{t}V$ ) are included.

Variable name	Description
nJet25	Number of jets with $p_T > 25$ GeV, $ \eta  < 2.4$
MaxEtaJet25	Maximum $ \eta $ of any (non-CSV-loose) jet with $p_T > 25$ GeV
totCharge	Sum of lepton charges
nJetEta1	Number of jets with $ \eta  > 1.0$ , non-CSV-loose
detaFwdJetBJet	$\Delta\eta$ between forward light jet and hardest CSV loose jet
detaFwdJet2BJet	$\Delta\eta$ between forward light jet and second hardest CSV loose jet (defaults to -1 in events with only one CSV loose jet)
detaFwdJetClosestLep	$\Delta\eta$ between forward light jet and closest lepton
dphiHighestPtSSPair	$\Delta\phi$ of highest $p_T$ same-sign lepton pair
minDRll	minimum $\Delta R$ between any two leptons
Lep3Pt/Lep2Pt	$p_T$ of the 3 <sup>rd</sup> lepton (2 <sup>nd</sup> for ss2l)

**Table 6.9:** MVA input discriminating variables

2033 Note that splitting the training in two groups reveals that some variables show  
 2034 opposite behavior for the two background sources; potentially screening the discrimi-  
 2035 nation power if they were to be used in a single discriminant. For some other variables  
 2036 the distributions are similar in both background cases.

2037 From table 6.9, it is clear that the input variables are correlated to some extend.  
 2038 These correlations play an important role for some MVA methods like the Fisher  
 2039 discriminant method in which the first step consist of performing a linear transfor-  
 2040 mation to an phase space where the correlations between variables are removed. In  
 2041 case a boosted decision tree (BDT) method however, correlations do not affect the  
 2042 performance. Figure 6.6 show the linear correlation coefficients for signal and back-  
 2043 ground for the two training cases (the signal values are identical by construction). As  
 2044 expected, strong correlations appears for variables related to the forward jet activity.  
 2045 Same trend is seen in case of the same sign dilepton channel in Figure ??.

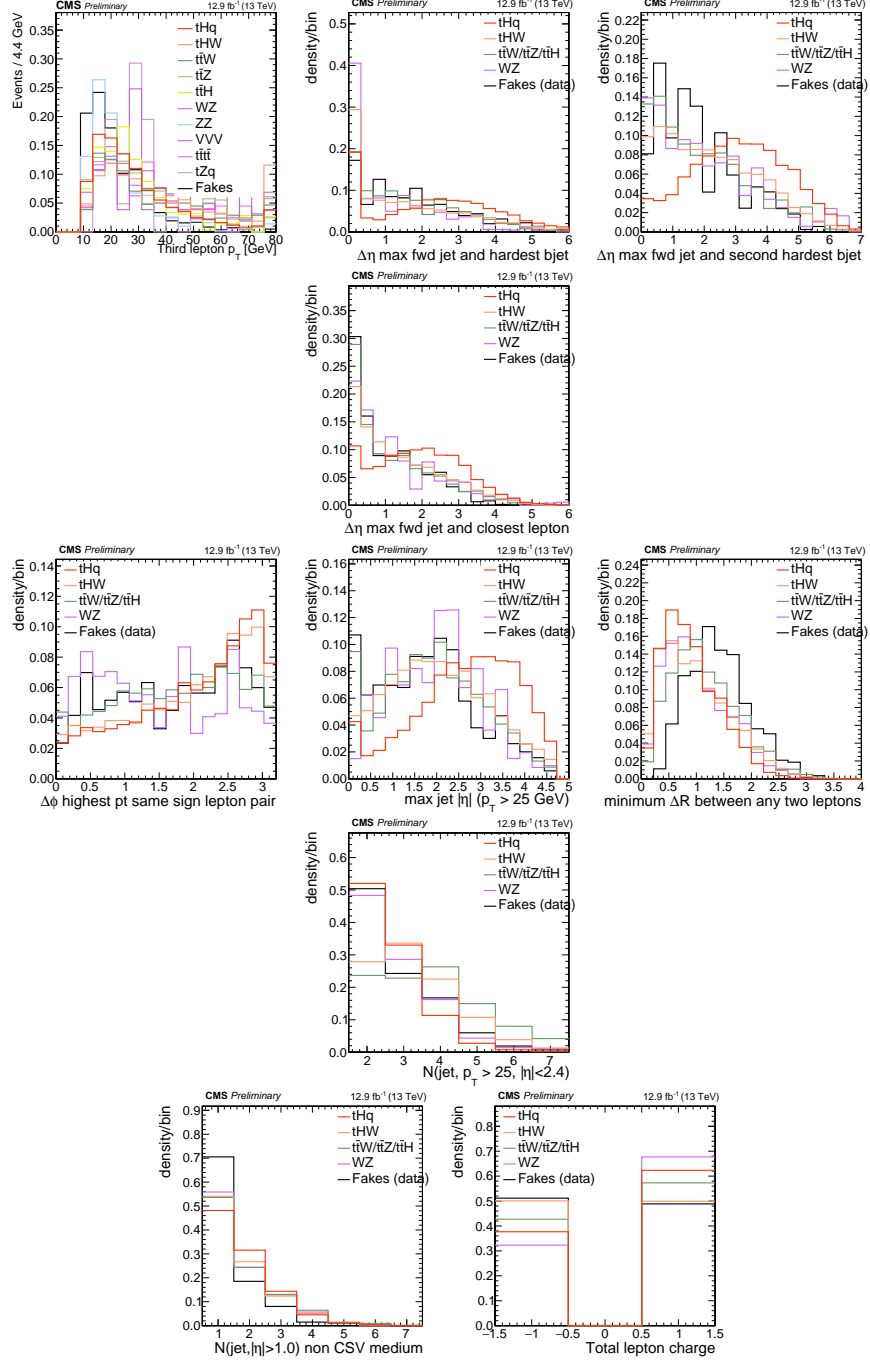


**Figure 6.3:** Distributions of input variables to the BDT for signal discrimination, three lepton channel.

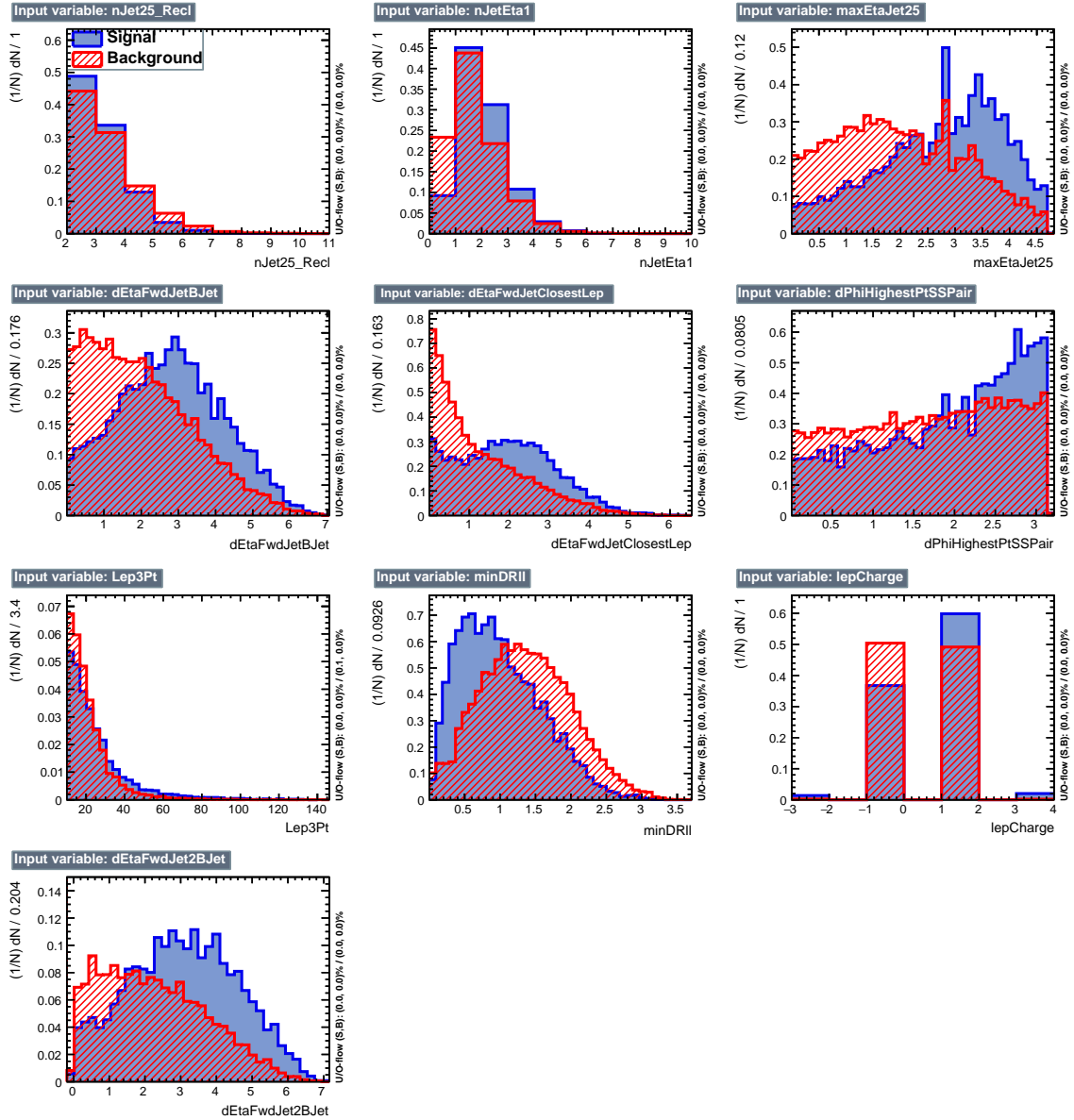


**Figure 6.4:** BDT inputs as seen by TMVA (signal, in blue, is  $tHq$ , background, in red, is  $t\bar{t}$ ) for the three lepton channel, discriminated against  $t\bar{t}$  (fakes) background.

### 2046 6.5.1 Classifiers response

2047 Several MVA algorithms were evaluated to determine the most appropriate method  
 2048 for this analysis. The plots in Fig. 6.7 (top) show the background rejection as a  
 2049 function of the signal efficiency for  $t\bar{t}$  and  $t\bar{t}V$  trainings (ROC curves) for the different

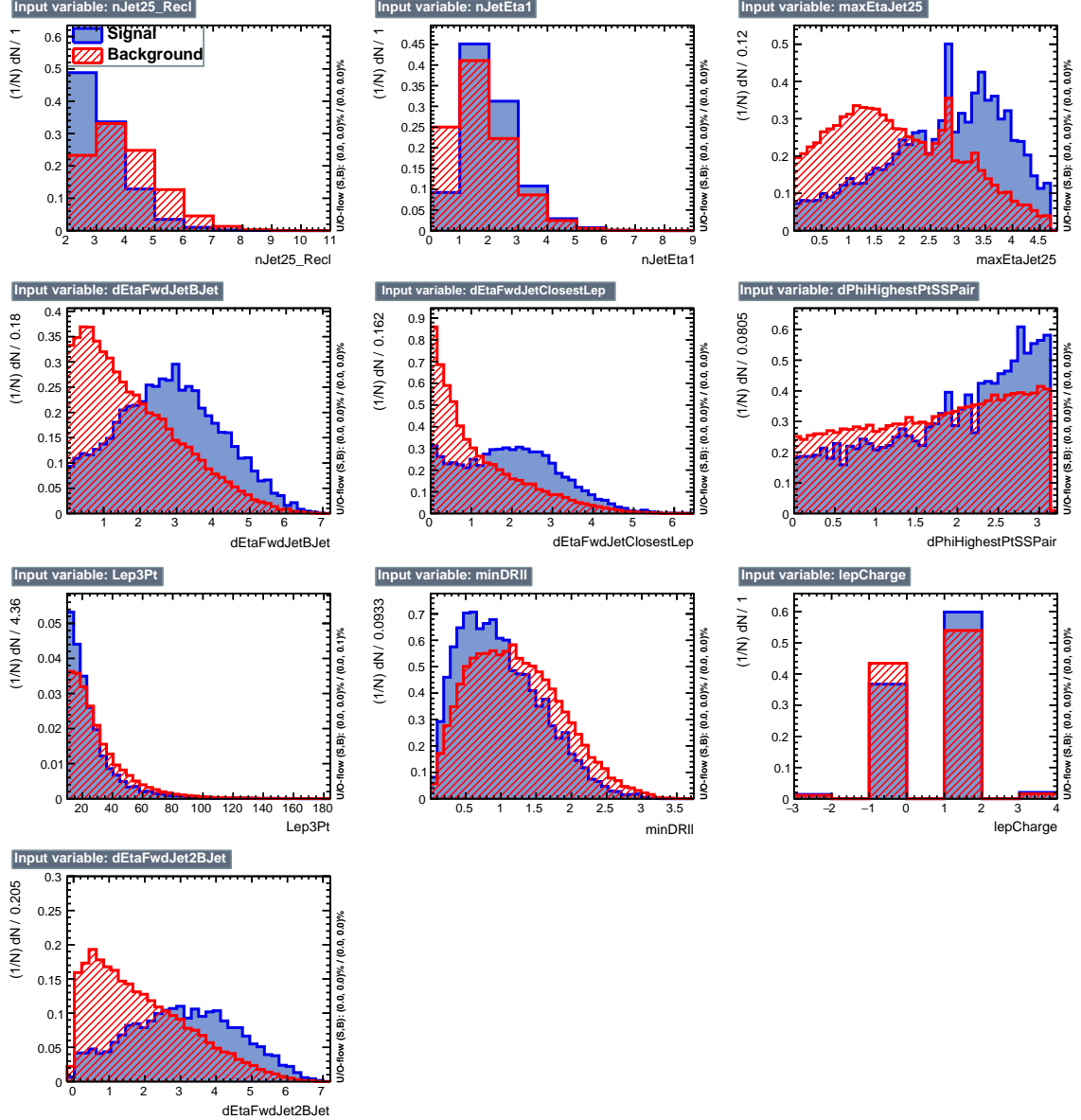


**Figure 6.5:** BDT inputs as seen by TMVA (signal, in blue, is  $tHq$ , background, in red, is  $t\bar{t}W+t\bar{t}Z$ ) for the three lepton channel, discriminated against  $t\bar{t}V$  background.

2050 algorithms that were evaluated.

2051 In both cases the gradient boosted decision tree (“BDTA\_GRAD”) classifier offers  
 2052 the best results, followed by an adaptive BDT classifier (“BDTA”). The BDTA\_GRAD  
 2053 classifier output distributions for signal and backgrounds are shown on the bottom of  
 2054 Fig. 6.7. As expected, a good discrimination power is obtained using default discrim-

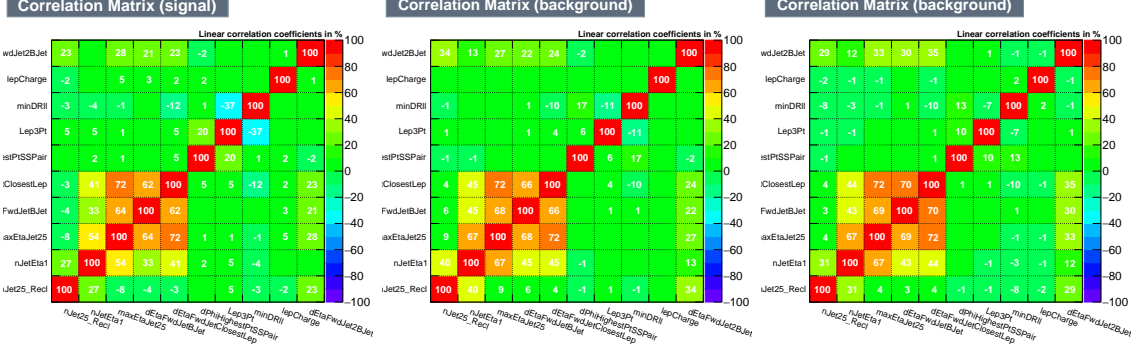


**Figure 6.6:** Signal (left),  $t\bar{t}$  background (middle), and  $t\bar{t}V$  background (right.) correlation matrices for the input variables in the TMVA analysis for the three lepton channel.

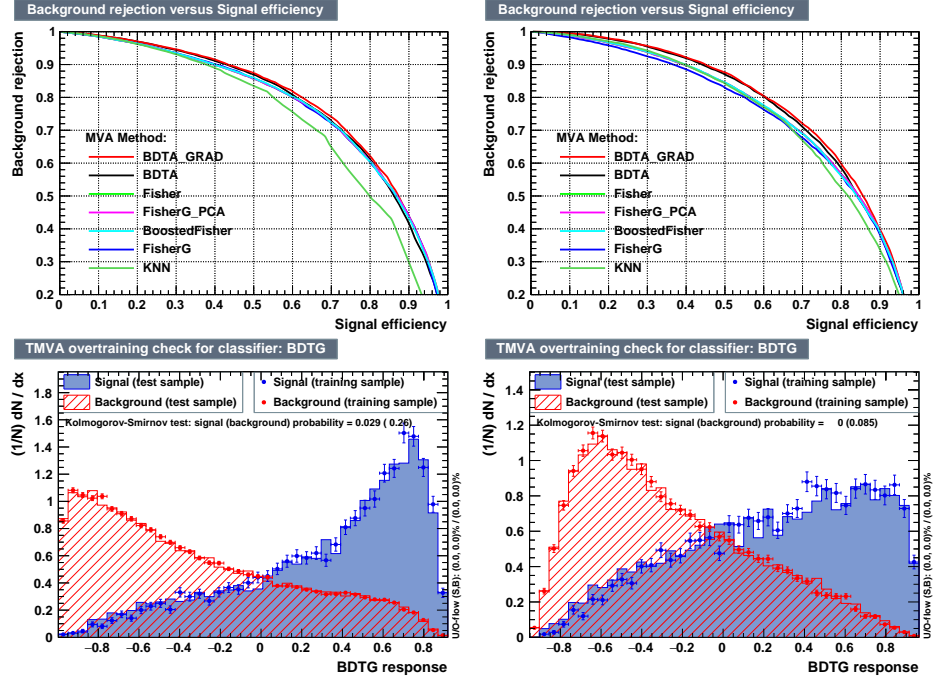


**Figure 6.7:** Top: background rejection vs signal efficiency (ROC curves) for various MVA classifiers (top) in the three lepton channel against  $t\bar{t}V$  (left) and  $t\bar{t}$  (right). Bottom: classifier output distributions for the gradient boosted decision trees, for training against  $t\bar{t}V$  (left) and against  $t\bar{t}$  (right).

2055 inator parameter values, with minimal overtraining. TMVA provides a ranking of the  
 2056 input variables by their importance in the classification process, shown in Tab. 6.10.  
 2057 The TMVA settings used in the BDT training are shown in Tab. 6.11.

ttbar training			ttV training		
Rank	Variable	Importance	Variable	Importance	Importance
1	minDRll	1.329e-01	dEtaFwdJetBJet	1.264e-01	
2	dEtaFwdJetClosestLep	1.294e-01	Lep3Pt	1.224e-01	
3	dEtaFwdJetBJet	1.209e-01	maxEtaJet25	1.221e-01	
4	dPhiHighestPtSSPair	1.192e-01	dEtaFwdJet2BJet	1.204e-01	
5	Lep3Pt	1.158e-01	dEtaFwdJetClosestLep	1.177e-01	
6	maxEtaJet25	1.121e-01	minDRll	1.143e-01	
7	dEtaFwdJet2BJet	9.363e-02	dPhiHighestPtSSPair	9.777e-02	
8	nJetEta1	6.730e-02	nJet25_Recl	9.034e-02	
9	nJet25_Recl	6.178e-02	nJetEta1	4.749e-02	
10	lepCharge	4.701e-02	lepCharge	4.116e-02	

**Table 6.10:** TMVA input variables ranking for BDTA\_GRAD method for the trainings in the three lepton channel. For both trainings the rankings show almost the same 5 variables in the first places.

---

```

TMVA.Types.kBDT
NTrees=800
BoostType=Grad
Shrinkage=0.10
!UseBaggedGrad
nCuts=50
MaxDepth=3
NegWeightTreatment=PairNegWeightsGlobal
CreateMVAPdfs

```

---

**Table 6.11:** TMVA configuration used in the BDT training.

## 2058 6.6 Additional discriminating variables

2059 Two additional discriminating variables were tested considering the fact that the  
 2060 forward jet in the background could come from the pileup; since we have a real  
 2061 forward jet in the signal, it could give some improvement in the discriminating power.  
 2062 The additional variables describe the forward jet momentum (fwdJetPt25) and the  
 2063 forward jet identification(fwdJetPUID). Distributions for these variables in the three  
 2064 lepton channel are shown in the figure 6.8. The forward jet identification distribution  
 2065 show that for both, signal and background, jets are mostly real jets.

2066 The testing was made including in the MVA input one variable at a time, so we

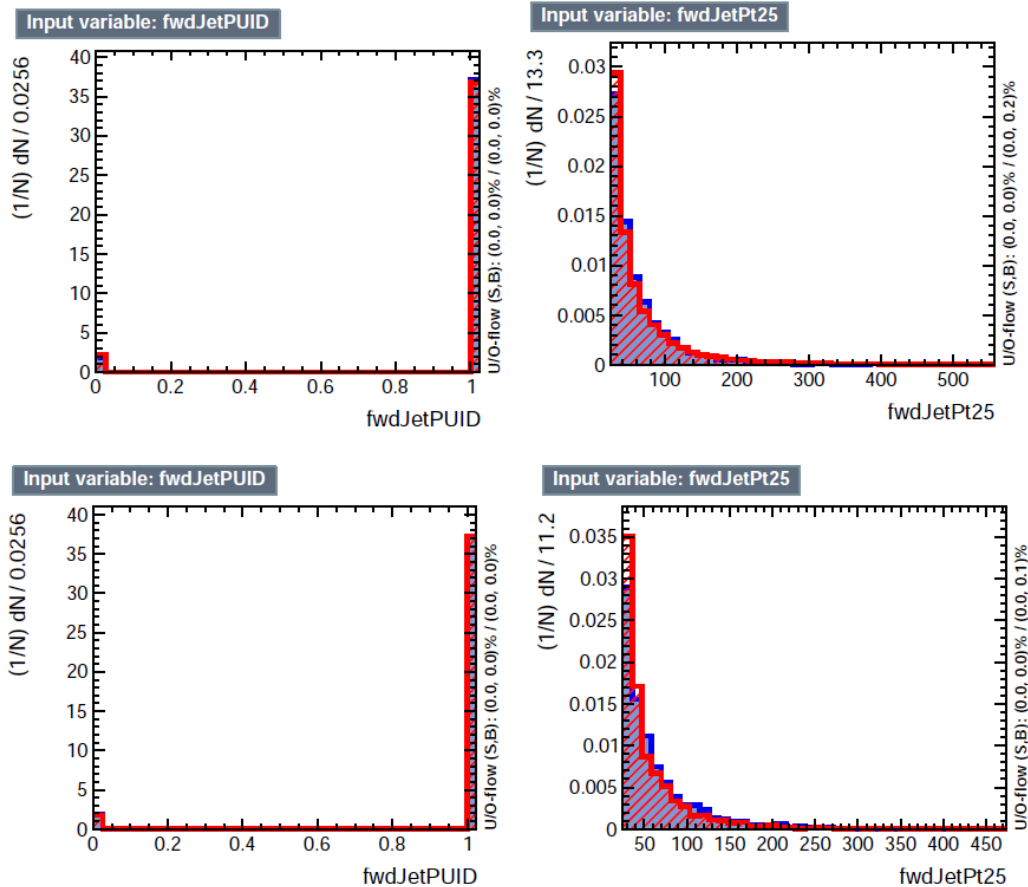


**Figure 6.8:** Additional discriminating variables distributions for ttV training (Top row) and tt training (bottom row) in the three lepton channel. The origin of the jets in the forward jet identification distribution is tagged as 0 for “pileup jets” while “real jets” are tagged as 1.

2067 can evaluate the discrimination power of each variable, and then both simultaneously.  
 2068 fwdJetPUID was ranked in the last place in importance (11) in both training (ttV  
 2069 and tt) while fwdJetPt25 was ranked 3 in the ttV training and 7 in the tt training.  
 2070 When training using 12 variables, fwdJetPt25 was ranked 5 and 7 in the ttV and tt  
 2071 trainings respectively, while fwdJetPUID was ranked 12 in both cases.

2072 The improvement in the discrimination performance provided by the additional  
 2073 variables is about 1%, so it was decided not to include them in the procedure. Table  
 2074 6.12 show the ROC-integral for all the testing cases we made.

ROC-integral	
base 10 var ttv	0.848
+ fwdJetPUID ttv	0.849
+ fwdJetPt25 ttv	0.856
12 var ttv	0.856
<hr/>	
base 10 var tt	0.777
+ fwdJetPUID tt	0.777
+ fwdJetPt25 tt	0.787
12 var	0.787

**Table 6.12:** ROC-integral for all the testing cases we made in the evaluation of the additional variables discriminating power. The improvement in the discrimination performance provided by the additional variables is about 1%

2075      **References**

- 2076 [1] J. Schwinger. "Quantum Electrodynamics. I. A Covariant Formulation". Physical Review. 74 (10): 1439-61, (1948).
- 2077
- 2078 [2] R. P. Feynman. "Space-Time Approach to Quantum Electrodynamics". Physical Review. 76 (6): 769-89, (1949).
- 2079
- 2080 [3] S. Tomonaga. "On a Relativistically Invariant Formulation of the Quantum Theory of Wave Fields". Progress of Theoretical Physics. 1 (2): 27-42, (1946).
- 2081
- 2082 [4] D.J. Griffiths, "Introduction to electrodynamics". 4th ed. Pearson, (2013).
- 2083 [5] F. Mandl, G. Shaw. "Quantum field theory." Chichester: Wiley (2009).
- 2084 [6] F. Halzen, and A.D. Martin, "Quarks and leptons: An introductory course in modern particle physics". New York: Wiley, (1984) .
- 2085
- 2086 [7] File: Standard\_Model\_of\_Elementary\_Particle\_dark.svg. (2017, June 12) Wikimedia Commons, the free media repository. Retrieved November 27, 2017 from <https://www.collegiate-advanced-electricity.com/single-post/2017/04/10/The-Standard-Model-of-Particle-Physics>.
- 2087
- 2088
- 2089
- 2090 [8] E. Noether, "Invariante Variationsprobleme", Nachrichten von der Gesellschaft der Wissenschaften zu Göttingen, mathematisch-physikalische Klasse, vol. 1918, pp. 235-257, (1918).
- 2091
- 2092

- 2093 [9] C. Patrignani et al. (Particle Data Group), Chin. Phys. C, 40, 100001 (2016)  
2094 and 2017 update.
- 2095 [10] M. Goldhaber, L. Grodzins, A.W. Sunyar “Helicity of Neutrinos”, Phys. Rev.  
2096 109, 1015 (1958).
- 2097 [11] Palanque-Delabrouille N et al. “Neutrino masses and cosmology with Lyman-  
2098 alpha forest power spectrum”, JCAP 11 011 (2015).
- 2099 [12] M. Gell-Mann. “A Schematic Model of Baryons and Mesons”. Physics Letters.  
2100 8 (3): 214-215 (1964).
- 2101 [13] G. Zweig. “An SU(3) Model for Strong Interaction Symmetry and its Breaking”  
2102 (PDF). CERN Report No.8182/TH.401 (1964).
- 2103 [14] G. Zweig. “An SU(3) Model for Strong Interaction Symmetry and its Breaking:  
2104 II” (PDF). CERN Report No.8419/TH.412(1964).
- 2105 [15] M. Gell-Mann. “The Interpretation of the New Particles as Displaced Charged  
2106 Multiplets”. Il Nuovo Cimento 4: 848. (1956).
- 2107 [16] T. Nakano, K, Nishijima. “Charge Independence for V-particles”. Progress of  
2108 Theoretical Physics 10 (5): 581-582. (1953).
- 2109 [17] N. Cabibbo, “Unitary symmetry and leptonic decays” Physical Review Letters,  
2110 vol. 10, no. 12, p. 531, (1963).
- 2111 [18] M.Kobayashi, T.Maskawa, “CP-violation in the renormalizable theory of weak  
2112 interaction,” Progress of Theoretical Physics, vol. 49, no. 2, pp. 652-657, (1973).
- 2113 [19] File: Weak Decay (flipped).svg. (2017, June 12). Wikimedia Com-  
2114 mons, the free media repository. Retrieved November 27, 2017 from

- 2115 https://commons.wikimedia.org/w/index.php?title=File:Weak\_Decay\_(flipped)  
2116 .svg&oldid=247498592.
- 2117 [20] Georgia Tech University. Coupling Constants for the Fundamental  
2118 Forces(2005). Retrieved January 10, 2018, from http://hyperphysics.phy-  
2119 astr.gsu.edu/hbase/Forces/couple.html#c2
- 2120 [21] M. Strassler. (May 31, 2013).The Strengths of the Known Forces. Retrieved Jan-  
2121 uary 10, 2018, from https://profmattstrassler.com/articles-and-posts/particle-  
2122 physics-basics/the-known-forces-of-nature/the-strength-of-the-known-forces/
- 2123 [22] S.L. Glashow. “Partial symmetries of weak interactions”, Nucl. Phys. 22 579-  
2124 588, (1961).
- 2125 [23] A. Salam, J.C. Ward. “Electromagnetic and weak interactions”, Physics Letters  
2126 13 168-171, (1964).
- 2127 [24] S. Weinberg, “A model of leptons”, Physical Review Letters, vol. 19, no. 21, p.  
2128 1264, (1967).
- 2129 [25] M. Peskin, D. Schroeder, “An introduction to quantum field theory”. Perseus  
2130 Books Publishing L.L.C., (1995).
- 2131 [26] A. Pich. “The Standard Model of Electroweak Interactions”  
2132 https://arxiv.org/abs/1201.0537
- 2133 [27] F.Bellaiche. (2012, 2 September). “What’s this Higgs boson anyway?”. Retrieved  
2134 from: https://www.quantum-bits.org/?p=233
- 2135 [28] M. Endres et al. Nature 487, 454-458 (2012) doi:10.1038/nature11255

- 2136 [29] F. Englert, R. Brout. “Broken Symmetry and the Mass of Gauge  
 2137 Vector Mesons”. Physical Review Letters. 13 (9): 321-23.(1964)  
 2138 doi:10.1103/PhysRevLett.13.321
- 2139 [30] P.Higgs. “Broken Symmetries and the Masses of Gauge Bosons”. Physical Re-  
 2140 view Letters. 13 (16): 508-509,(1964). doi:10.1103/PhysRevLett.13.508.
- 2141 [31] G.Guralnik, C.R. Hagen and T.W.B. Kibble. “Global Conservation Laws  
 2142 and Massless Particles”. Physical Review Letters. 13 (20): 585-587, (1964).  
 2143 doi:10.1103/PhysRevLett.13.585.
- 2144 [32] CMS collaboration. “Observation of a new boson at a mass of 125 GeV with  
 2145 the CMS experiment at the LHC”. Physics Letters B. 716 (1): 30-61 (2012).  
 2146 arXiv:1207.7235. doi:10.1016/j.physletb.2012.08.021
- 2147 [33] ATLAS collaboration. “Observation of a New Particle in the Search for the Stan-  
 2148 dard Model Higgs Boson with the ATLAS Detector at the LHC”. Physics Letters  
 2149 B. 716 (1): 1-29 (2012). arXiv:1207.7214. doi:10.1016/j.physletb.2012.08.020.
- 2150 [34] ATLAS collaboration; CMS collaboration (26 March 2015). “Combined Mea-  
 2151 surement of the Higgs Boson Mass in pp Collisions at  $\sqrt{s}=7$  and 8 TeV with  
 2152 the ATLAS and CMS Experiments”. Physical Review Letters. 114 (19): 191803.  
 2153 arXiv:1503.07589. doi:10.1103/PhysRevLett.114.191803.
- 2154 [35] LHC InternationalMasterclasses“When protons collide”. Retrieved from [http://atlas.physicsmasterclasses.org/en/zpath\\_protoncollisions.htm](http://atlas.physicsmasterclasses.org/en/zpath_protoncollisions.htm)  
 2155
- 2156 [36] CMS Collaboration, “SM Higgs Branching Ratios and Total Decay Widths (up-  
 2157 date in CERN Report4 2016)”. <https://twiki.cern.ch/twiki/bin/view/LHCPhysics/CERNYellowReportPageBR> , last accessed on 17.12.2017.  
 2158

- 2159 [37] R.Grant V. “Determination of Higgs branching ratios in  $H \rightarrow W^+W^- \rightarrow l\nu jj$   
 2160 and  $H \rightarrow ZZ \rightarrow l^+l^-jj$  channels”. Physics Department, University of Tennessee  
 2161 (Dated: October 31, 2012). Retrieved from <http://aesop.phys.utk.edu/ph611/2012/projects/Riley.pdf>
- 2163 [38] LHC Higgs Cross Section Working Group, Denner, A., Heinemeyer, S. et al.  
 2164 “Standard model Higgs-boson branching ratios with uncertainties”. Eur. Phys.  
 2165 J. C (2011) 71: 1753. <https://doi.org/10.1140/epjc/s10052-011-1753-8>
- 2166 [39] F. Maltoni, K. Paul, T. Stelzer, and S. Willenbrock, “Associated production  
 2167 of Higgs and single top at hadron colliders”, Phys.Rev. D64 (2001) 094023,  
 2168 [hep-ph/0106293].
- 2169 [40] S. Biswas, E. Gabrielli, F. Margaroli, and B. Mele, “Direct constraints on the  
 2170 top-Higgs coupling from the 8 TeV LHC data,” Journal of High Energy Physics,  
 2171 vol. 07, p. 073, (2013).
- 2172 [41] M. Farina, C. Grojean, F. Maltoni, E. Salvioni, and A. Thamm, “Lifting de-  
 2173 generacies in Higgs couplings using single top production in association with a  
 2174 Higgs boson,” Journal of High Energy Physics, vol. 05, p. 022, (2013).
- 2175 [42] T.M. Tait and C.-P. Yuan, “Single top quark production as a window to physics  
 2176 beyond the standard model”, Phys. Rev. D 63 (2000) 014018 [hep-ph/0007298].
- 2177 [43] F. Demartin, F. Maltoni, K. Mawatari, and M. Zaro, “Higgs production in  
 2178 association with a single top quark at the LHC,” European Physical Journal C,  
 2179 vol. 75, p. 267, (2015).

- 2180 [44] CMS Collaboration, “Modelling of the single top-quark production in associa-  
2181 tion with the Higgs boson at 13 TeV.” [https://twiki.cern.ch/twiki/bin/](https://twiki.cern.ch/twiki/bin/viewauth/CMS/SingleTopHiggsGeneration13TeV)  
2182 [viewauth/CMS/SingleTopHiggsGeneration13TeV](#), last accessed on 16.01.2018.
- 2183 [45] CMS Collaboration, “SM Higgs production cross sections at  $\sqrt{s} =$   
2184 13 TeV.” [https://twiki.cern.ch/twiki/bin/](https://twiki.cern.ch/twiki/bin/view/LHCPhysics/CERNYellowReportPageAt13TeV)  
2185 [view/LHCPhysics/CERNYellowReportPageAt13TeV](#), last accessed on 16.01.2018.
- 2186 [46] S. Dawson, The effective W approximation, Nucl. Phys. B 249 (1985) 42.
- 2187 [47] S. Biswas, E. Gabrielli and B. Mele, JHEP 1301 (2013) 088 [[arXiv:1211.0499 \[hep-ph\]](#)].
- 2189 [48] F. Demartin, B. Maier, F. Maltoni, K. Mawatari, and M. Zaro, “tWH associated  
2190 production at the LHC”, European Physical Journal C, vol. 77, p. 34, (2017).  
2191 [arXiv:1607.05862](#)
- 2192 [49] LHC Higgs Cross Section Working Group, “Handbook of LHC Higgs Cross  
2193 Sections: 4.Deciphering the Nature of the Higgs Sector”, [arXiv:1610.07922](#).
- 2194 [50] J. Ellis, D. S. Hwang, K. Sakurai, and M. Takeuchi.“Disentangling Higgs-Top  
2195 Couplings in Associated Production”, JHEP 1404 (2014) 004, [[arXiv:1312.5736](#)].
- 2196 [51] CMS Collaboration, V. Khachatryan et al., “Precise determination of the mass  
2197 of the Higgs boson and tests of compatibility of its couplings with the standard  
2198 model predictions using proton collisions at 7 and 8 TeV,” [arXiv:1412.8662](#).
- 2199 [52] ATLAS Collaboration, G. Aad et al., “Updated coupling measurements of the  
2200 Higgs boson with the ATLAS detector using up to  $25 \text{ fb}^{-1}$  of proton-proton  
2201 collision data”, ATLAS-CONF-2014-009.

- 2202 [53] ATLAS and CMS Collaborations, “Measurements of the Higgs boson produc-  
 2203 tion and decay rates and constraints on its couplings from a combined ATLAS  
 2204 and CMS analysis of the LHC pp collision data at  $\sqrt{s} = 7$  and 8 TeV,” (2016).  
 2205 CERN-EP-2016-100, ATLAS-HIGG-2015-07, CMS-HIG-15-002.
- 2206 [54] File:Cern-accelerator-complex.svg. Wikimedia Commons,  
 2207 the free media repository. Retrieved January, 2018 from  
 2208 <https://commons.wikimedia.org/wiki/File:Cern-accelerator-complex.svg>
- 2209 [55] J.L. Caron , “Layout of the LEP tunnel including future LHC infrastructures.”,  
 2210 (Nov, 1993). A C Collection. Legacy of AC. Pictures from 1992 to 2002. Re-  
 2211 trieval from <https://cds.cern.ch/record/841542>
- 2212 [56] M. Vretenar, “The radio-frequency quadrupole”. CERN Yellow Report CERN-  
 2213 2013-001, pp.207-223 DOI:10.5170/CERN-2013-001.207. arXiv:1303.6762
- 2214 [57] L.Evans. P. Bryant (editors). “LHC Machine”. JINST 3 S08001 (2008).
- 2215 [58] CERN Photographic Service.“Radio-frequency quadrupole, RFQ-1”, March  
 2216 1983, CERN-AC-8303511. Retrieved from <https://cds.cern.ch/record/615852>.
- 2217 [59] CERN Photographic Service “Animation of CERN’s accelerator net-  
 2218 work”, 14 October 2013. DOI: 10.17181/cds.1610170 Retrieved from  
 2219 <https://videos.cern.ch/record/1610170>
- 2220 [60] C.Sutton. “Particle accelerator”.Encyclopedia Britannica. July 17, 2013. Re-  
 2221 trieval from <https://www.britannica.com/technology/particle-accelerator>.
- 2222 [61] L.Guiraud. “Installation of LHC cavity in vacuum tank.”. July 27 2000. CERN-  
 2223 AC-0007016. Retrieved from <https://cds.cern.ch/record/41567>.

- 2224 [62] J.L. Caron, “Magnetic field induced by the LHC dipole’s superconducting coils”.  
2225 March 1998. AC Collection. Legacy of AC. Pictures from 1992 to 2002. LHC-  
2226 PHO-1998-325. Retrieved from <https://cds.cern.ch/record/841511>
- 2227 [63] AC Team. “Diagram of an LHC dipole magnet”. June 1999. CERN-DI-9906025  
2228 retrieved from <https://cds.cern.ch/record/40524>.
- 2229 [64] CMS Collaboration “Public CMS Luminosity Information”.  
2230 <https://twiki.cern.ch/twiki/bin/view/CMSPublic/LumiPublicResults#2016>  
2231 \_proton\_proton\_13\_TeV\_collis, last accessed 24.01.2018
- 2232 [65] J.L. Caron. “LHC Layout” AC Collection. Legacy of AC. Pictures  
2233 from 1992 to 2002. September 1997, LHC-PHO-1997-060. Retrieved from  
2234 <https://cds.cern.ch/record/841573>.
- 2235 [66] J.A. Coarasa. “The CMS Online Cluster: Setup, Operation and Maintenance  
2236 of an Evolving Cluster”. ISGC 2012, 26 February - 2 March 2012, Academia  
2237 Sinica, Taipei, Taiwan.
- 2238 [67] CMS Collaboration. “The CMS experiment at the CERN LHC” JINST 3 S08004  
2239 (2008).
- 2240 [68] CMS Collaboration. “CMS detector drawings 2012” CMS-PHO-GEN-2012-002.  
2241 Retrieved from <http://cds.cern.ch/record/1433717>.
- 2242 [69] R. Breedon. “View through the CMS detector during the cooldown of the  
2243 solenoid on February 2006. CMS Collection”, February 2006, CMS-PHO-  
2244 OREACH-2005-004, Retrieved from <https://cds.cern.ch/record/930094>.
- 2245 [70] A. Dominguez et. al. “CMS Technical Design Report for the Pixel Detector  
2246 Upgrade”, CERN-LHCC-2012-016. CMS-TDR-11.

- 2247 [71] CMS Collaboration. “Description and performance of track and primary-vertex  
2248 reconstruction with the CMS tracker,” Journal of Instrumentation, vol. 9, no.  
2249 10, p. P10009,(2014).
- 2250 [72] CMS Collaboration and M. Brice. “Images of the CMS Tracker Inner  
2251 Barrel”, November 2008, CMS-PHO-TRACKER-2008-002. Retrieved from  
2252 <https://cds.cern.ch/record/1431467>.
- 2253 [73] M. Weber. “The CMS tracker”. 6th international conference on hyperons, charm  
2254 and beauty hadrons Chicago, June 28-July 3 2004.
- 2255 [74] CMS Collaboration. “Projected Performance of an Upgraded CMS Detector at  
2256 the LHC and HL-LHC: Contribution to the Snowmass Process”. Jul 26, 2013.  
2257 arXiv:1307.7135
- 2258 [75] L. Veillet. “End assembly of HB with EB rails and rotation in-  
2259 side SX ”,January 2002. CMS-PHO-HCAL-2002-002. Retrieved from  
2260 <https://cds.cern.ch/record/42594>.
- 2261 [76] J. Puerta-Pelayo.“First DT+RPC chambers installation round in the  
2262 UX5 cavern.”. January 2007, CMS-PHO-OREACH-2007-001. Retrieved from  
2263 <https://cds.cern.ch/record/1019185>
- 2264 [77] X. Cid Vidal and R. Cid Manzano. “CMS Global Muon Trigger” web  
2265 site: Taking a closer look at LHC. Retrieved from [https://www.lhc-closer.es/taking\\_a\\_closer\\_look\\_at\\_lhc/0.lhc\\_trigger](https://www.lhc-closer.es/taking_a_closer_look_at_lhc/0.lhc_trigger)
- 2267 [78] WLCG Project Office, “Documents & Reference - Tiers - Structure,” (2014).  
2268 <http://wlcg.web.cern.ch/documents-reference> , last accessed on 30.01.2018.

- 2269 [79] CMS Collaboration. “CMSSW Application Framework”,  
2270 <https://twiki.cern.ch/twiki/bin/view/CMSPublic/WorkBookCMSSWFramework>,  
2271 last accesses 06.02.2018
- 2272 [80] A. Buckleya, J. Butterworthb, S. Giesekec, et. al. “General-purpose event gen-  
2273 erators for LHC physics”. arXiv:1101.2599v1 [hep-ph] 13 Jan 2011
- 2274 [81] A. Quadt. “Top Quark Physics at Hadron Colliders”. Advances in the Physics  
2275 of Particles and Nuclei. Springer-Verlag Berlin Heidelberg. DOI: 10.1007/978-  
2276 3-540-71060-8 (2007)
- 2277 [82] DurhamHep Data Project, “The Durham HepData Project - PDF Plotter.”  
2278 <http://hepdata.cedar.ac.uk/pdf/pdf3.html> , last accessed on 02.02.2018.
- 2279 [83] F. Maltoni, G. Ridolfi, and M. Ubiali, “b-initiated processes at the LHC: a  
2280 reappraisal,” Journal of High Energy Physics, vol. 07, p. 022, (2012).
- 2281 [84] B. Andersson, G. Gustafson, G.Ingelman and T. Sjostrand, “Parton fragmen-  
2282 tation and string dynamics”, Physics Reports, Vol. 97, No. 2-3, pp. 31-145,  
2283 1983.
- 2284 [85] CMS Collaboration, “Event generator tunes obtained from underlying event  
2285 and multiparton scattering measurements;” European Physical Journal C, vol.  
2286 76, no. 3, p. 155, (2016).
- 2287 [86] J. Alwall et. al., “The automated computation of tree-level and next-to-leading  
2288 order differential cross sections, and their matching to parton shower simula-  
2289 tions,” Journal of High Energy Physics, vol. 07, p. 079, (2014).

- 2290 [87] S. Frixione, P. Nason, and C. Oleari, “Matching NLO QCD computations with  
2291 Parton Shower simulations: the POWHEG method,” Journal of High Energy  
2292 Physics, vol. 11, p. 070, (2007).
- 2293 [88] S. Agostinelli et al., “GEANT4: A Simulation toolkit,” Nuclear Instruments  
2294 and Methods in Physics, vol. A506, pp. 250–303, (2003).
- 2295 [89] J.Allison et.al.,“Recent developments in Geant4”, Nuclear Instruments and  
2296 Methods in Physics Research A 835 (2016) 186-225.
- 2297 [90] CMS Collaboration “Full Simulation Offline Guide”, <https://twiki.cern.ch/twiki/bin/view/CMSPublic/SWGuideSimulation>, last accessed 04.02.2018
- 2299 [91] A. Giammanco. “The Fast Simulation of the CMS Experiment” J. Phys.: Conf.  
2300 Ser. 513 022012 (2014)
- 2301 [92] A.M. Sirunyan et. al. “Particle-flow reconstruction and global event description  
2302 with the CMS detector”, JINST 12 P10003 (2017) <https://doi.org/10.1088/1748-0221/12/10/P10003>.
- 2304 [93] The CMS Collaboration. “ Description and performance of track and pri-  
2305 mary vertex reconstruction with the CMS tracker”. JINST 9 P10009 (2014).  
2306 doi:10.1088/1748-0221/9/10/P10009
- 2307 [94] J. Incandela. “Status of the CMS SM Higgs Search” July 4, 2012. Pdf slides.  
2308 Retrieved from [https://indico.cern.ch/event/197461/contributions/1478917/attachments/290954/406673/CMS\\_4July2012\\_Final.pdf](https://indico.cern.ch/event/197461/contributions/1478917/attachments/290954/406673/CMS_4July2012_Final.pdf)
- 2310 [95] P. Billoir and S. Qian, “Simultaneous pattern recognition and track fitting by  
2311 the Kalman filtering method”, Nucl. Instrum. Meth. A 294 219. (1990).

- 2312 [96] W. Adam, R. Fruhwirth, A. Strandlie and T. Todorov, “Reconstruction of  
 2313 electrons with the Gaussian sum filter in the CMS tracker at LHC”, eConf  
 2314 C 0303241 (2003) TULT009 [physics/0306087].
- 2315 [97] K. Rose, “Deterministic Annealing for Clustering, Compression, Classification,  
 2316 Regression and related Optimisation Problems”, Proc. IEEE 86 (1998) 2210.
- 2317 [98] R. Fruhwirth, W. Waltenberger and P. Vanlaer, “ Adaptive Vertex Fitting”,  
 2318 CMS Note 2007-008 (2007).
- 2319 [99] CMS collaboration, “Performance of CMS muon reconstruction in pp collision  
 2320 events at  $\sqrt{s} = 7$  TeV ”, JINST 7 P10002 2012, [arXiv:1206.4071].
- 2321 [100] M. Cacciari, G. P. Salam, and G. Soyez, “The anti- $k_t$  jet clustering algorithm,”  
 2322 Journal of High Energy Physics, vol. 04, p. 063, (2008).
- 2323 [101] B. Dorney. “Anatomy of a Jet in CMS”. Quantum Diaries. June  
 2324 1st, 2011. Retrieved from <https://www.quantumdiaries.org/2011/06/01/anatomy-of-a-jet-in-cms/>
- 2326 [102] The CMS Collaboration.“Event Displays from the high-energy collisions at 7  
 2327 TeV”, May 2010, CMS-PHO-EVENTS-2010-007, Retrieved from <https://cds.cern.ch/record/1429614>.
- 2329 [103] The CMS collaboration. “Determination of jet energy calibration and transverse  
 2330 momentum resolution in CMS”. JINST 6 P11002 (2011). <http://dx.doi.org/10.1088/1748-0221/6/11/P11002>
- 2332 [104] The CMS Collaboration, “Introduction to Jet Energy Corrections at  
 2333 CMS.”. <https://twiki.cern.ch/twiki/bin/view/CMS/IntroToJEC>, last ac-  
 2334 cessed 10.02.2018.

- 2335 [105] CMS Collaboration Collaboration. “Identification of b quark jets at the CMS  
2336 Experiment in the LHC Run 2”. Tech. rep. CMS-PAS-BTV-15-001. Geneva:  
2337 CERN, (2016). <https://cds.cern.ch/record/2138504>.
- 2338 [106] CMS Collaboration Collaboration. “Performance of missing energy reconstruc-  
2339 tion in 13 TeV pp collision data using the CMS detector”. Tech. rep. CMS-PAS-  
2340 JME16-004. Geneva: CERN, 2016. <https://cds.cern.ch/record/2205284>.
- 2341 [107] K. Skovpen. “Event displays highlighting the main properties of heavy flavour  
2342 jets in the CMS Experiment”, Aug 2017, CMS-PHO-EVENTS-2017-006. Re-  
2343 trieved from <https://cds.cern.ch/record/2280025>.
- 2344 [108] G. Cowan. “Topics in statistical data analysis for high-energy physics”.  
2345 arXiv:1012.3589v1